

# **Processing and Consolidation of Amorphous and Nanocrystalline Aluminum-Nickel-Lanthanum Alloys**

vorgelegt von  
Diplom-Ingenieur  
Jens Vierke  
aus Berlin

von der Fakultät III - Prozesswissenschaften  
der Technischen Universität Berlin  
zur Erlangung des akademischen Grades  
Doktor der Ingenieurwissenschaften  
-Dr.-Ing.-

genehmigte Dissertation

Promotionsausschuss:

Vorsitzender: Prof. Dr. rer. nat. Helmut Schubert

Berichter: Prof. Dr. rer. nat. John Banhart

Berichter: Prof. Dr. rer. nat. Gerhard Wilde

Tag der wissenschaftlichen Aussprache: 14.12.2007

Berlin 2008

D83



# Abstract

This study investigates two Al-rich metallic glass alloys:  $\text{Al}_{87}\text{Ni}_8\text{La}_5$  and  $\text{Al}_{85}\text{Ni}_{10}\text{La}_5$  (at-%). These alloys have a strength that is two to three times higher than conventional polycrystalline Al-alloys. They are candidate light-weight materials for structural applications. The aim of this study was to produce bulk amorphous Al-alloys by gas-atomization and subsequent powder consolidation. Different consolidation techniques were applied in order to investigate how plastic deformation and processing temperature influence the stability of the amorphous phase.

$\text{Al}_{87}\text{Ni}_8\text{La}_5$  and  $\text{Al}_{85}\text{Ni}_{10}\text{La}_5$  powders were processed by gas-atomization using argon and helium gas. Helium-atomized amorphous  $\text{Al}_{85}\text{Ni}_{10}\text{La}_5$  powders were consolidated by means of high pressure torsion (HPT) at room temperature applying different levels of torsion, equal channel angular pressing (ECAP) at different temperatures, and hot pressing at different temperatures. The samples were investigated by different methods, for example: scanning and transmission electron microscopy, in-situ and ex-situ angle-dispersive X-ray diffractometry (XRD), ex-situ energy-dispersive XRD, differential scanning calorimetry, and inductively coupled plasma mass spectroscopy.

Within the methods used in this study, ECAP and HPT yield partially consolidated samples, whereas hot pressing can produce fully consolidated samples. Sample density and Vickers microhardness of consolidated powders increase with plastic shear deformation and with processing temperature. The hardness increases mainly due to partially crystallization of the amorphous phase. Upon continuous heating, as-atomized powders show a glass transition and a subsequent crystallization of fcc-Al and intermetallic phases within a narrow temperature range. A primary crystallization of fcc-Al occurs during isothermal heating below the crystallization temperature. After consolidation, no glass transition occurs upon continuous heating. Consolidated samples show fcc-Al crystals within the residual amorphous matrix. The volume fraction of fcc-Al crystals increases with plastic shear deformation and with processing temperature. The results indicate that primary precipitation of fcc-Al is strain-induced and possibly athermal.

Additionally, simultaneous in-situ X-ray attenuation and in-situ X-ray diffraction experiments were performed upon amorphous  $\text{Al}_{85}\text{Ni}_{10}\text{La}_5$  splats. These experiments show that the mass density of amorphous  $\text{Al}_{85}\text{Ni}_{10}\text{La}_5$  increases 1.4-1.7% during phase transformation from the amorphous to the crystalline state.



# Declaration

Ich erkläre an Eides statt, dass die vorliegende Dissertation in allen Teilen von mir selbstständig angefertigt wurde und die benutzten Hilfsmittel vollständig angegeben worden sind.



Dedicated to my parents.  
Meinen Eltern gewidmet.



# Acknowledgments

I would like to thank Prof. John Banhart, who offered me the opportunity to do my PhD at the department Materials of the Hahn-Meitner-Institut (HMI) Berlin. I would like to thank the second examiner Prof. Gerhard Wilde, who had the patience to read my thesis as well as for his fruitful comments during the last days of writing it. Furthermore, I would like to thank him and his colleague Dr. Nancy Boucharat for the nice ambiance at different conferences. I would like to thank Prof. Helmut Schubert for being the chairman during my defense of my PhD. And I would also like to thank his assistant lecturer André Glück for his logistical support. I would like to express my greatest gratitude to PD Dr. Gerhard Schumacher, who guided me through the science of metallic glasses during the last months of my PhD. I would like to thank him for his moral and scientific support as well as for the hundreds of discussions we had.

This work would have been impossible without the support of my cooperation partners: Many thanks to Dr. Martin Balog, Dr. Juraj Nagy, Ivan Kramer, and Dr. František Šimančík from the Institute of Materials and Machine Mechanics of the Slovak Academy of Sciences (SAS) in Bratislava, Slovak Republic, for their support, enthusiasm and efforts to perform ECAP experiments, for their hospitality, especially when showing me around Bratislava and its surroundings. In addition, I would like to thank Dr. Drušan Janičkovic and Dr. Peter Švec from the Institute of Physics of the SAS for the fruitful discussions in Bratislava and during international conferences.

I would like to thank Prof. Vitaly P. Pilyugin from the Institute of High Pressure Physics of the Ural Branch of the Russian Academy of Sciences in Yekaterinburg, Russia, for performing HPT experiments and for the fantastic adventure to the Siberian wilderness. Thanks to his wife and his PhD students who accompanied me on that trip. Special thanks to Yulia Badryzlova and Kseniya Baxitova for translating and accompanying me in Yekaterinburg. In this context I would like to thank Prof. A. Ye. Yermakov, who helped me set up the cooperation, and Dr. Christian Abromeit and Prof. Nikolai Lazarev to overcome logistical challenges.

I greatly acknowledge Tsaisuke T. Sasaki and Prof. K. Hono from the Graduate School of Pure and Applied Sciences, University of Tsukuba, and the National Institute for Materials Science, Tsukuba, Japan, for sparc sintering (SPS) experiments on amorphous powder and investigations on consolidated samples. Further thanks to Dr. Sergio Scudino and Prof. Jürgen Eckert from IFW Dresden, who investigated samples after SPS on partially crystalline powder. Thank you Dr. Ivo Zizak and Ingwer Denks from the Berlin synchrotron radiation facility (BESSY) for your interest in my topic and your support in performing in-situ XRD and energy-dispersive XRD experiments. Many thanks to Dr. Oliver Göhrke from the Institute of Ceramic Materials of the Berlin University of Technology,

who performed hot gas extraction experiments, and to Dr. Christian Wolf from the department “Spurenelemente” of the HMI, who performed ICP-MS experiments. I would like to thank M. Stobig and the NANOVAL G.m.b.H Berlin for producing the powders.

I owe special thanks to friends, and current and former colleagues of the department Materials, who supported and inspired me throughout the years of my PhD: Yvonne Herzog and Marlies Schneider in ordering my scattered brain and giving me administrative support, Christiane Förster, my room mate Claudia Leistner, Dagmar Köpnick-Welzel, Holger Kropf, Peter Schubert-Bischoff, Harald Stapel for their help in the laboratory, their technical and moral support, Jörg Beiorat for IT support, Dr. Nelia Wanderka and once again, Dr. Christian Abromeit, Dr. André Heinemann for his lectures in ethics, psychology, fractal dimensions, quantum physics,....., and Dr. Elvira Garcia-Matres Ginsberg, who inspired and supported me to learn Spanish, Dr. Cynthia Chang, who gave me moral, scientific and intercultural support. I would also like to thank Catalina Jimenez, the famous Bollywood actor Dr. Sashank Nayak, Manas Mukerjee, Nilam Barekar for a wonderful time in Berlin, Saxony Switzerland and the Baltic Sea, as well as for their patience when explaining them the Green Point System, the unforgotten Dr. Alan Brothers (“Albert Einstein told me, you are not Alan Brothers!”), my room mate Rainer Grupp, “last-man-standing” Hans M. Hellwig, Sicherheitsingenieur Stefan Höring and Ingmar Wieler, Dr. Stefan Mechler, Dr. Vitaly Kindratschuk and Dr. Evgeny Davidov, Dr. Martin Kamel, Dr. Olivier Perroud, Antonio Rueda and Panaceite, Dr. Norbert Babscan, Dr. Axel Griesche, Dr. Francisco Garcia-Moreno, Micha Bierwirth, André Hilger, Dr. Markus Wollgarten, and Dr. Simon Zabler. I would like to thank the colleagues of the institute’s construction department and workshop, who supported me in improving the meltspinner, repairing devices and constructing experimental set-up’s. Furthermore, I would like to thank Dr. Julia Herrero-Albios for the wonderful time in Berlin and in Zaragoza, Moshe Weizman for our guitar sessions, Dr. Bernhard Neumann and Prof. Upadrasta Ramamurty. Special thanks to Anna Bienas, Sandra Goergen, and Julie Colthorpe.

Last but not least, I would like to thank my family for their unconditional support during these years.

# Contents

<b>1</b>	<b>Introduction</b>	<b>1</b>
<b>2</b>	<b>Literature Survey</b>	<b>5</b>
2.1	Metallic Glasses . . . . .	6
2.1.1	Definition of Metallic Glass . . . . .	6
2.1.2	Glass Forming Ability . . . . .	6
2.2	Crystallization . . . . .	8
2.2.1	Nucleation . . . . .	9
2.2.2	Growth . . . . .	10
2.2.3	Crystallization Reactions . . . . .	11
2.3	Rapid Quenching Techniques . . . . .	11
2.3.1	Gas Atomization . . . . .	11
2.3.2	Splat Quenching . . . . .	12
2.4	Powder Consolidation Techniques . . . . .	12
2.4.1	Nanocrystalline Materials . . . . .	13
2.4.2	Hot Pressing . . . . .	14
2.4.3	High Speed Sintering . . . . .	14
2.4.4	Spac Plasma Sintering . . . . .	14
2.4.5	Direct Extrusion . . . . .	14
2.4.6	Equal Channel Angular Pressing . . . . .	15
2.4.7	High Pressure Torsion . . . . .	16
2.5	Al-based Metallic Glasses . . . . .	17
2.5.1	Structure and Glass Forming Ability . . . . .	17
2.5.2	Crystallization Behavior . . . . .	18
2.5.3	Consolidation of Amorphous Powders . . . . .	19
<b>3</b>	<b>Experimental Procedures</b>	<b>21</b>
3.1	Processing of Al-Ni-La Metallic Glasses . . . . .	22
3.1.1	Synthesis of Master Alloys . . . . .	22
3.1.2	Rapid Solidification by Gas Atomization . . . . .	22
3.1.3	Rapid Solidification by Splat Quenching . . . . .	22
3.1.4	Rapid Solidification by Melt Spinning . . . . .	23
3.2	Annealing . . . . .	23
3.3	Consolidation of Al-based Metallic Glass Powder . . . . .	23
3.3.1	Hot Pressing . . . . .	23
3.3.2	High Speed Sintering . . . . .	24

3.3.3	Sparc Plasma Sintering . . . . .	24
3.3.4	Direct Extrusion . . . . .	24
3.3.5	Equal Channel Angular Pressing . . . . .	24
3.3.6	High Pressure Torsion . . . . .	26
3.4	Sample Analysis . . . . .	26
3.4.1	Density Measurements . . . . .	26
3.4.2	Vickers Microhardness . . . . .	26
3.4.3	Granulometry . . . . .	27
3.4.4	Hot Gas Extraction . . . . .	27
3.4.5	Inductively Coupled Plasma Mass Spectroscopy . . . . .	27
3.4.6	Differential Scanning Calorimetry . . . . .	28
3.4.7	Scanning Electron Microscopy . . . . .	29
3.4.8	Transmission Electron Microscopy . . . . .	29
3.4.9	X-ray Diffractometry . . . . .	30
3.4.10	Simultaneous In-situ X-ray Attenuation and X-ray Diffraction . . . . .	32
<b>4</b>	<b>Experimental Results: Powders and Splats</b>	<b>35</b>
4.1	He-atomized Al <sub>85</sub> Ni <sub>10</sub> La <sub>5</sub> Powder, Batch I . . . . .	36
4.1.1	Particle Size Distribution and Morphology . . . . .	36
4.1.2	Microstructure of As-atomized Powder . . . . .	37
4.1.3	Crystallization during Continuous Heating . . . . .	37
4.1.4	Crystallization during Isothermal Heating . . . . .	39
4.1.5	Calorimetric Characterization of Crystallization . . . . .	40
4.2	He-atomized Al <sub>85</sub> Ni <sub>10</sub> La <sub>5</sub> Powder, Batch II . . . . .	41
4.2.1	Particle Size Distribution and Morphology . . . . .	41
4.2.2	Crystallization during Continuous Heating . . . . .	42
4.2.3	Crystallization during Isothermal Heating . . . . .	43
4.3	Ar-atomized Al <sub>85</sub> Ni <sub>10</sub> La <sub>5</sub> Powder . . . . .	44
4.4	He-atomized Al <sub>87</sub> Ni <sub>8</sub> La <sub>5</sub> Powder, Batch I . . . . .	45
4.4.1	Microstructure of As-atomized Powder . . . . .	45
4.4.2	Crystallization during Continuous Heating . . . . .	45
4.5	He-atomized Al <sub>87</sub> Ni <sub>8</sub> La <sub>5</sub> Powder, Batch II . . . . .	47
4.6	Ar-atomized Al <sub>87</sub> Ni <sub>8</sub> La <sub>5</sub> Powder . . . . .	49
4.6.1	Microstructure of As-atomized Powder . . . . .	49
4.6.2	Crystallization during Continuous Heating . . . . .	50
4.7	Comparison of Powders . . . . .	51
4.7.1	Influence of Alloy Composition, Atomization Gas, and Powder Particle Size on Microstructure and Oxygen Content . . . . .	51
4.7.2	Summary of Powder Properties . . . . .	51
4.8	Simultaneous In-situ X-ray Attenuation and Diffraction . . . . .	53
4.8.1	Composition of Al-Ni-La Splats . . . . .	53
4.8.2	Continuous Heating . . . . .	53
4.8.3	Crystallization during isothermal heating . . . . .	56

<b>5</b>	<b>Experimental Results: Consolidation</b>	<b>59</b>
5.1	Hot Pressing of Al-Ni-La Metallic Glass Powders . . . . .	60
5.1.1	In-situ Monitoring of Hot Pressing . . . . .	60
5.1.2	Morphology of Hot Pressed Samples . . . . .	60
5.1.3	Density and Hardness of Hot Pressed Samples . . . . .	61
5.1.4	XRD of Hot Pressed Samples . . . . .	62
5.1.5	Calorimetric Characterization after Hot Pressing . . . . .	63
5.1.6	Hot Pressing of Different Alloy Powders . . . . .	64
5.2	ECAP of Al-Ni-La Metallic Glass Powder . . . . .	64
5.2.1	Load and Ram Speed Evolution during ECAP . . . . .	65
5.2.2	Morphology of ECAP Processed Samples . . . . .	65
5.2.3	Density and Hardness of ECAP Processed Samples . . . . .	67
5.2.4	XRD of ECAP Processed Samples . . . . .	67
5.2.5	Calorimetric Characterization after ECAP . . . . .	68
5.2.6	Influence of Plastic Deformation on Morphology . . . . .	69
5.2.7	Influence of Plastic Deformation on Density, Hardness, Structure	71
5.2.8	Influence of Plastic Deformation on Calorimetric Behavior . . . . .	71
5.3	HPT of Al-Ni-La Metallic Glass Powder . . . . .	73
5.3.1	Morphology and Density as a Function of Torsion . . . . .	73
5.3.2	Morphology in Radial Direction . . . . .	73
5.3.3	XRD and Calorimetric Characterization as a Function of Torsion .	75
5.3.4	XRD and Calorimetric Characterization in Radial Direction . . . .	76
5.4	Extrusion and HSS of Al-Ni-La Metallic Glass Powder . . . . .	78
5.4.1	Extrusion of Al-Ni-La Metallic Glass Powder . . . . .	78
5.4.2	High Speed Sintering (HSS) of Al-Ni-La Metallic Glass Powder .	79
<b>6</b>	<b>Discussion</b>	<b>81</b>
6.1	Processing of Al-Ni-La Metallic Glass . . . . .	82
6.2	Crystallization of As-atomized Al-Ni-La Metallic Glass . . . . .	84
6.2.1	As-quenched State of Al-Ni-La Metallic Glass . . . . .	84
6.2.2	Temperature-induced Crystallization . . . . .	85
6.2.3	Strain-induced Crystallization of Al <sub>85</sub> Ni <sub>10</sub> La <sub>5</sub> Powders . . . . .	87
6.2.4	Density Changes during Crystallization . . . . .	91
6.3	Consolidation of Al-Ni-La Metallic Glass Powder . . . . .	91
<b>7</b>	<b>Summary and Conclusions</b>	<b>95</b>



# **Chapter 1**

## **Introduction**

Aluminum (Al) is abundant in the earth's crust yielding to massive use in engineering. One of the advantages of Al is its low specific weight compared to steel's so that it is a potential candidate in many engineering applications. A traditional way of enhancing the properties is by element addition and therefore, according to the application, the mechanical properties such as light specific strength, good workability and good corrosion resistance can be tailored. Up to now, commercial Al-alloys show maximum room-temperature strength of "only" 600 MPa (A7075), which hinders its use in high strength applications.

Aluminium-rich metallic glass alloys have attracted a lot of interest due to their potential to develop nanostructured materials, which can have a two to three times larger yield strength in comparison to conventional polycrystalline Al-alloys. An enhanced yield strength of approximately 1000 MPa has been observed in a Al-rich metallic glass after partial devitrification, whenever an extremely high number density of Al-nanocrystals ( $\geq 10^{22} \text{ m}^{-3}$ ) is present in the residual amorphous matrix [1]. Complete devitrification can lead to a maximum yield strength of about 1420 MPa [2]. The nanocrystals can be produced either by thermal treatment [3] or by plastic deformation [1], [4], [5]. Deformation- or strain-induced crystallization<sup>1</sup> at ambient and sub-ambient temperatures has been observed after cold rolling [4], extreme bending [1], [5], nanoindentation [6], and high pressure torsion [7]. The strain-induced crystallization mechanism is however supposed to be different from crystallization mechanism induced by thermal treatment [1], [4], [5]. Strain-induced crystallization is believed to be the result of static atom displacement's, whereas crystallization induced by thermal treatment stems from thermal atomic jumps.

Since Al-rich metallic glasses are marginal glassformers, they can be synthesized only in limited sample dimensions such as powders, flakes, ribbons or layers. Powders and flakes require consolidation to a bulk material for any structural applications. Consolidation by hot pressing [2], spark sintering [8], [9], [10] and hot extrusion [11] have to be performed at rather high temperatures (around the crystallization onset and higher) to be feasible and/or to achieve sufficiently compacted samples with low porosity. As a consequence of the high processing temperature, the bulk materials consolidated in one of these ways are usually completely crystallized and hence extremely brittle. As alternative methods, equal channel angular pressing (ECAP) and high pressure torsion (HPT) provide consolidation at low temperatures avoiding complete crystallization [7], [12], [13], [14]. Besides this, ECAP and HPT are good methods to study properties as a function of the amount of plastic shear deformation.

In this work, Al-Ni-La alloy system was chosen due to its relatively good glass forming ability compared to other known Al-rich metallic glasses. The synthesis and consolidation of amorphous  $\text{Al}_{85}\text{Ni}_{10}\text{La}_5$  and  $\text{Al}_{87}\text{Ni}_8\text{La}_5$  powder by means of hot pressing, ECAP, HPT, sintering and hot extrusion was motivated by one main question: is it possible to consolidate amorphous  $\text{Al}_{85}\text{Ni}_{10}\text{La}_5$  alloy by preserving the amorphous phase?

This work provides a literature survey and experimental procedures in chapter 2 and 3, respectively. Chapters 4 and 5 show experimental results of rapid quenched powders,

---

<sup>1</sup>Deformation- and strain-induced crystallization are both used in scientific literature. This work refers to the term strain-induced crystallization

---

splats, and consolidation experiments. The discussion in chapter 6 focuses on processing of metallic glasses, its crystallization behavior upon annealing and upon plastic deformation, mass density changes during crystallization, and an assessment of different consolidation techniques. Chapter 7 summarizes main results and conclusions.



## **Chapter 2**

# **Literature Survey**

## 2.1 Metallic Glasses

Metallic glasses are metastable materials which have an amorphous structure. The Glass Forming Ability (GFA) of an alloy can be described by thermodynamical, kinetical, structural and empirical models.

### 2.1.1 Definition of Metallic Glass

Metallic glasses or amorphous metallic alloys are one class of non-crystalline solids. In the context of metallic glasses, the term amorphous<sup>1</sup> indicates lacking organization of atomic structure whereas the term “glass” is associated with phenomena of the glass transition. Amorphous metallic alloys have no long range order compared to crystalline solids. But locally, they show structural indications to nearest neighbor atoms (short and medium range order) [16]. X-ray, neutron and electron scattering of amorphous structures involve a broad low intensity diffraction peak instead of discrete high intensity diffraction pattern in crystalline materials. The glass transition is characterized by changing the slope of the property curve (e.g. specific heat  $c_p$ , enthalpy  $H$  and viscosity  $\eta$ , see figure 2.1) during heating or cooling near the glass transition temperature  $T_g$ . The region between melting temperature  $T_m$  and  $T_g$  is called supercooled melt.

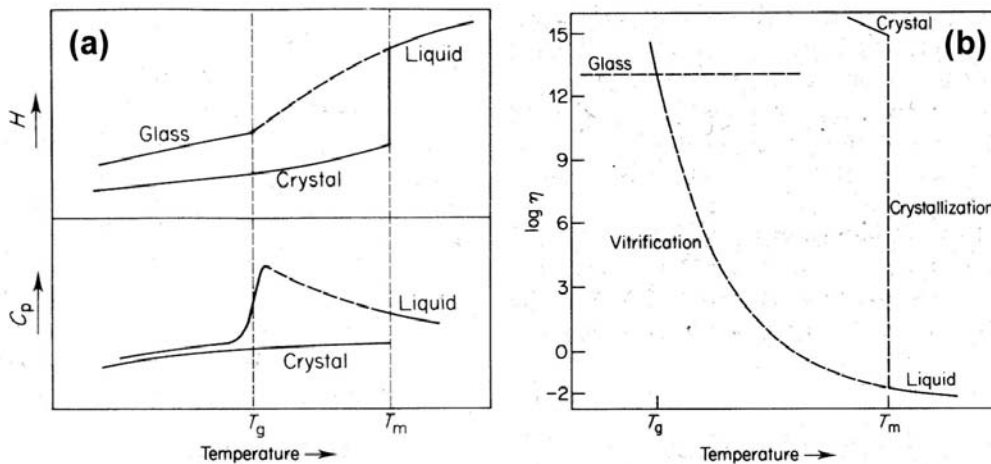


Figure 2.1: Temperature dependence of enthalpy  $H$ , specific heat  $C_p$  (a) and viscosity  $\eta$  (b) corresponding to crystallization and vitrification [16].

### 2.1.2 Glass Forming Ability

Liquids which can yield metallic glasses require fast cooling below  $T_g$ . Fast transformations affect the interfacial equilibrium during the phase transformation process towards different levels of equilibrium. Common phase diagrams apply under the condition of

<sup>1</sup>The adjective “amorphous” means: having no definite form, being without definite character or nature, and lacking organization or unity. [15].

interfacial equilibrium, which exist when relaxation time of a transformation process is infinitely long. The hierarchy of equilibrium levels characterizes the capability of a material to relax towards full or metastable equilibrium during processing. A suppression of full equilibrium phases can be hereby kinetically and thermodynamically favorable [17], [18]. The transition from stable to metastable equilibrium phase diagram is illustrated in figure 2.2. Kinetic constraints during processing suppress the formation of equilibrium  $\gamma$  phase (figure 2.2(a)) resulting in a metastable eutectic of  $\alpha$  and  $\beta$  phases (figure 2.2(b)). Under extreme conditions, the liquidus and solidus boundaries collapse to so-called  $T_0$ -curves (figure 2.2(c)), which represent thermodynamic restrictions for partitionless transformations [19]. This means in case of rapid quenching, that due to diffusional constraints no partition occurs along the fast propagation of liquid-solid interface (loss of interfacial equilibrium). Thus, the crystallization is inhibited and the liquid state conserved forming a metallic glass.

The  $T_0$ -curve in figure 2.2(c) shows a composition-dependent  $T_g$  and solidus boundaries of solid solution phases  $\alpha_{SS}$  and  $\beta_{SS}$ . According to figure 2.2(c), glass formation can be achieved by different pathways, like rapid quenching of homogeneous melt (pathway I and II) and compositional changes by solid state processes (pathway III). Solid state processes, such as cold rolling, high pressure torsion or ball milling, can lead to amorphous phases by destabilizing crystalline phases when the maximum solubility is exceeded [17], [18]. This process can be also considered as strain-induced mixing. They require temperatures below  $T_g$  where the diffusion is low (e.g. low atomic mobility) under the condition that strain-induced mixing is performed on long timescales.

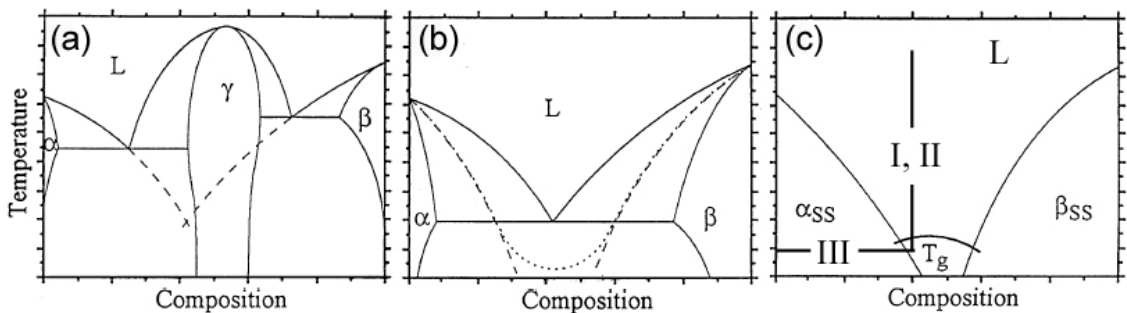


Figure 2.2: Schematic illustration (a-c) of the evolution of a phase diagram under metastable equilibrium conditions. If primary phases have different structures and low solubility for the other species, then  $T_0$ -curves (dotted lines) might not intersect (c). Such a situation favors glass formation by either rapid quenching (pathway I and II) or by solid state reactions (pathway III) [17], [18].

In contrast, rapid quenching of a melt from high temperatures involves rather fast diffusion (e.g. high atomic mobility). Thus, high cooling rates are required in order to achieve a metallic glass by circumventing crystallization [17]. The time range where metallic glasses can be obtained is limited by the nucleation and growth kinetics. One way to represent kinetic restrictions is based upon the application of time-temperature-transformation (TTT) diagrams, as illustrated in figure 2.3. It shows a “nose” shape which is the reflection of the competition between the increasing driving force for crystallization and the decreasing atomic mobility with supercooling the melt [20].

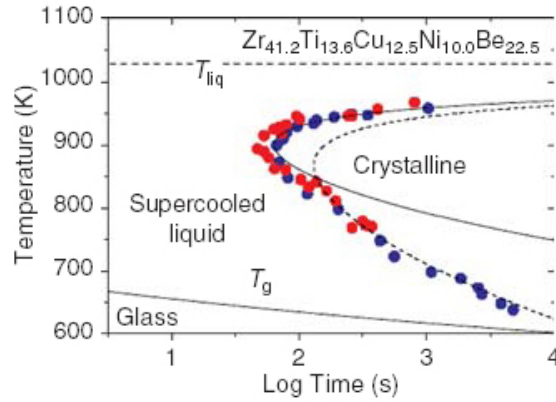


Figure 2.3: Time-temperature-transformation diagram of Vitreloy 1. The curves labeled  $T_{liq}$  and  $T_g$  indicate the liquidus and the glass transition temperature, respectively [20].

For the first time in 1960; Klement, Willens and Duwez reported the synthesis of amorphous metal in Au-Si system obtained from a melt by rapid quenching [21]. First known glass forming alloys required high critical cooling rates of about  $10^6$  K/s to obtain amorphous phases by means of melt spinning. These high cooling rates limit sample dimensions of metallic glasses to a few  $\mu\text{m}$ , at least in one dimension. Over the years, new metallic glass forming alloys were developed in order to reduce the critical cooling rate, thus increasing their glass forming ability. Nowadays, critical cooling rates ranging from  $10^1$  K/s to 1 K/s permit to achieve Bulk Metallic Glasses (BMG) with critical sizes of a few cm. This is currently limited to few metallic glass forming systems based on Pd [22], Zr [23] Y [24] Mg [25] and La [26]. Considering applications, many of these alloys contain either expensive (Pd) or undesirable elements (such as toxic Be in ZrTiCuNiBe alloys). Consequently, current research is partially focused on the search for inexpensive alloys based on Fe, Cu, Ni, and Al with enhanced GFA.

It was reported that alloy systems with deep eutectics lead to good GFA [27]. According to this phenomenon, Turnbull [28] provided a tool to describe GFA by the reduced glass transition temperature  $T_{rg}$  which is given by the  $T_g/T_m$  ratio, where  $T_g$  and  $T_m$  denote the glass transition and the melting temperature, respectively. Good GFA exists for alloys which show  $T_{rg} > 2/3$ . A further tool to describe GFA was given by Inoue [29] which provides empirical rules for good GFA. According to this, a good glass former consists of a 3 component system, in which the main constituents have large atomic size differences ( $\geq 12\%$ ) and a negative (exothermic) heat of mixing. Further models are reviewed in [30].

## 2.2 Crystallization

Generally the crystallization is described by a nucleation and growth process. The driving force of crystallization is the difference of free energy  $\Delta G$  between metastable glass or supercooled melt and stable crystalline phases [31].

### 2.2.1 Nucleation

From classical nucleation theory, one distinguishes between homogeneous and heterogeneous nucleation [32]. In homogeneous nucleation theory, temporary random fluctuations of the composition in a metastable supercooled melt can locally form crystalline clusters. As soon as a crystalline cluster is formed, the free energy rises at first. Though growth is associated with a reduction of free energy and therefore thermodynamically favorable. The change of free energy  $\Delta G$  can be described by volume free energy of a spherical cluster and its surface free energy, according to the equation:

$$\Delta G = -\frac{4\pi}{3}r^3\Delta g_v + 4\pi r^2\sigma \quad (2.1)$$

where  $r$  is the radius of the cluster,  $\Delta g_v$  is the free energy per unit volume and  $\sigma$  is the surface free energy. The relation between  $\Delta G$  and  $r$  is illustrated in figure 2.4. Whether such cluster is unstable or stable, inducing its decay or its growth respectively, depends on the critical cluster radius  $r_c$ . Applying an activation energy concept, the critical cluster is defined by the critical free energy  $\Delta G_c$  barrier, which has to be overcome for continuous growth. A cluster exceeding the critical size will grow by reducing its free energy.

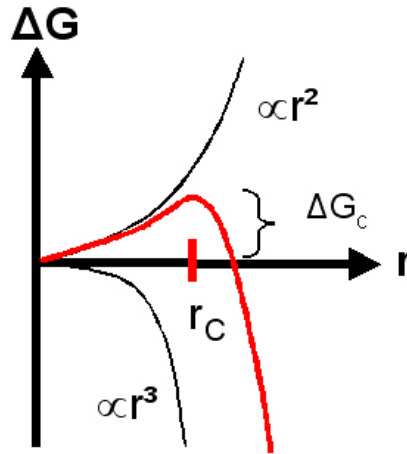


Figure 2.4: Free energy  $\Delta G_c$  of a spherical cluster with radius  $r$ .  $\Delta G_c$  and  $r_c$  represent critical free energy and critical cluster radius, respectively.

Crystals with radii smaller than  $r_c$  are called embryos. Larger crystals are called nuclei [33]. The critical radius  $r_c$  is supposed to be of the order of 1 nm [31]. In heterogeneous nucleation, a foreign material provides a surface which facilitates the formation of a critical nucleus.

The rate of formation of critical nuclei, or the homogeneous (steady state) nucleation rate  $\dot{N}$  is given by:

$$\dot{N} \propto \exp\left(-\frac{\Delta G_c}{k_B T}\right) \exp\left(-\frac{Q}{k_B T}\right) \quad (2.2)$$

where  $\Delta G_c$  denotes critical free energy,  $Q$  denotes activation energy for the transfer of a matrix-atom to an embryo,  $k_B$  and  $T$  denote Boltzmann constant and temperature, respectively. This expression emphasizes the temperature dependence of  $\dot{N}$ . When homogeneous nucleation is a stochastic process obeying Boltzmann statistics, it is called thermal nucleation. Hence nucleation proceeds constantly during isothermal conditions (steady state). But under non-isothermal conditions like rapid quenching, sub-critical embryos are promoted to form nuclei when the critical size decreases during cooling. This process is called athermal nucleation. It is a deterministic process in which the number of nucleation events depends on supercooling but not on time [34].

The roles of thermal or athermal growth of pre-existing (quenched-in) nuclei in real nucleation depends on GFA, thermal history and process conditions. In marginal glass formers (see chapter 2.5), growth of quenched-in nuclei is expected to be the dominant mechanism [31]. Heterogeneous nucleation induced by inhomogeneities, impurities and compositional segregates might act as nucleation sites but not predominantly [31].

### 2.2.2 Growth

The growth rate  $u$  of stable nuclei under isothermal conditions may be limited by (a) either transfer of the advancing surface of nuclei (surface or interface controlled) or (b) by rate of diffusion of atoms towards or away from growing nuclei (diffusion controlled). For (a), only small diffusion paths are required and growth is linear with time  $u \propto t$ ; whereas for (b), long range diffusion leads to growth which is parabolic with time  $u \propto \sqrt{t}$ .

The product of nucleation and growth rate leads to nose-shaped rate-temperature curves as presented in figure 2.5.

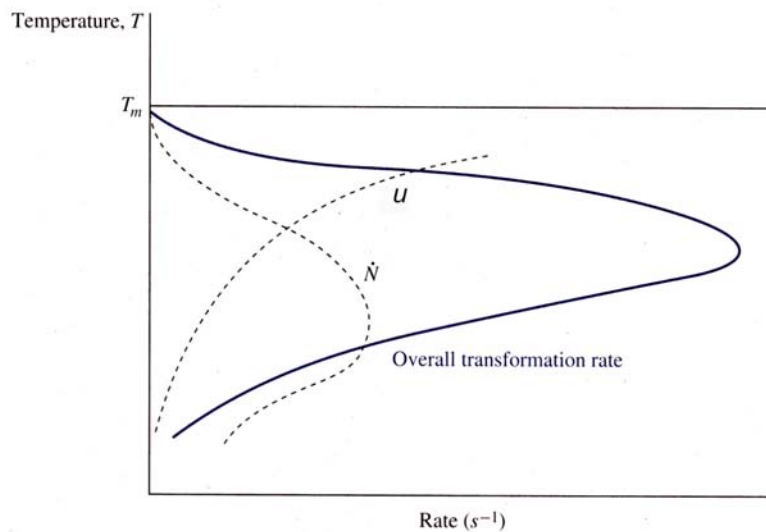


Figure 2.5: The overall transformation rate is the product of nucleation  $\dot{N}$  and growth rate  $u$  [35].

### 2.2.3 Crystallization Reactions

According to [36], crystallization reactions can be generally divided into three categories. **Polymorphous crystallization:** A crystal grows into the glassy matrix without change of composition. No long range diffusion is required. **Eutectic crystallization:** The glass transforms simultaneously into two crystalline phases. The overall composition of eutectic crystal phase and glass remain the same. Similar to polymorphous crystallization, no long range diffusion is required. **Primary crystallization:** A primary phase crystallizes into the glassy matrix, which has a composition different to the matrix. As a consequence, solute atoms will be rejected from the crystal and will create a compositional gradient in the region ahead of the crystal. Long range diffusion is required for crystal growth. Moreover, constitutional supercooling can occur and induce dendritic growth. The investigation of the crystal morphology allows to distinguish among these crystallization reactions.

## 2.3 Rapid Quenching Techniques

Rapid quenching conveys the liquid melt into an amorphous metallic solid by circumventing equilibrium reactions like crystallization. In this work, different rapid quenching techniques were used such as gas atomization, splat quenching and melt spinning. Cooling rates and achievable specimen quantity define mainly the differences among these three techniques. Melt spinning was performed in the framework of a student's project [37]. It is not further presented here.

### 2.3.1 Gas Atomization

In gas atomization, a high-velocity gas jet breaks up a molten metal stream into fine droplets that solidify to form a powder. The most dominating process parameters are: oxygen content of the gas, surface oxide contents of the melt, gas velocity (in practice regulated by gas pressure), gas to metal flow ratio, gas density, and nature of the gas. Beside physical process parameters, the nozzle geometry strongly influences the powder particle size. The NANOVAL nozzle design permits to obtain very fine powders containing narrow particle size distributions and hence a high yield of fine powders [38], [39], [40].

The cooling rate depends mostly on melt droplet size and type of atomization gas used [41], [42]. Both parameters allow cooling rates ranging from  $10^2$  to  $10^7$  K/s, which are many orders of magnitude above those in casting processes [38]. In case of powders, the cooling rate  $dT/dt$  as function of the powder particle diameter  $d$  can be determined by [43]:

$$\frac{dT}{dt} = \frac{10}{(d/2)^2} \left[ \frac{\text{K} \times \text{cm}^2}{\text{s}} \right] \quad (2.3)$$

The formula disregards the cooling medium and might be considered as the maximum cooling rate. The powders used in this project have particle sizes ranging from  $\leq 1$  to  $50 \mu\text{m}$  yielding cooling rates of approximately  $10^9$  to  $10^6$  K/s. The powder particle distribution is generally unimodal and follows log normal law [38], [39]. Mean and median diameter are used to describe the size of a powder. The mass median diameter  $d_{50}$  expresses the 50% point of the cumulative weight vs. particle size distribution. Information about the spread of the particle size distribution can be expressed by the geometric standard deviation  $\sigma_g$ . According to Ünal et al. [39], the geometric standard deviation  $\sigma_g$  of a log normal distribution can be calculated by:

$$\sigma_g = \sqrt{(d_{84.1}/d_{15.9})} = (d_{84.1}/d_{50}) = (d_{50}/d_{15.9}) \quad (2.4)$$

where  $d_{84.1}$  and  $d_{15.9}$  denote the 84.1% and 15.9% point, respectively, of the cumulative weight vs. particle size distribution. The  $\sigma_g$  of gas-atomized powder varies in the range of 1.8 and 2.5 [39].

### 2.3.2 Splat Quenching

In splat quenching, a cube of Al-Ni-La master alloy is inductively levitated and molten in an evacuated recipient. As soon as the power supply of induction heating is switched off, the melt droplet falls down passing an optical sensor which triggers the rapid closure of a horizontally positioned pair of Copper pistons. The melt droplet is flattened and quenched rapidly between the piston surfaces which have a high thermal conductivity [41]. The cooling rate during solidification of a molten alloy strongly depends on the sample dimension and the piston material in which the heat is conducted. In case of splats, the cooling rate  $dT/dt$  can be estimated by formula 2.3 replacing powder particle diameter  $d$  by splat thickness  $d^*$ . In this work, the splat thickness ranged between 35 and 45  $\mu\text{m}$  yielding cooling rates of approximately  $10^6$  K/s.

## 2.4 Powder Consolidation Techniques

Powder consolidation<sup>2</sup> requires pressure and temperature. Severe shear stresses and shear strains are desirable because they are most effective in collapsing pores and cracking surface oxide layers. In order of increasing shear effectiveness during consolidation, one can list following processes: spark plasma sintering (SPS), uni-axial hot pressing, direct extrusion, equal channel angular pressing (ECAP) and high pressure torsion (HPT). HPT and ECAP are also known as severe plastic deformation (SPD) methods.

---

<sup>2</sup>The verb consolidate (etymologically from Latin: to make solid) means: to unite, to strengthen and to form into a compact mass [15]. The verb compact means: having a dense structure or parts closely packed or joined, occupying a small volume by reason of efficient use of space and being solid [15]. No distinction between both terms is made in the scientific literature even though “consolidation” has a nuance of leading to denser, pore-free materials. This work refers to the term consolidation.

SPS experiments were performed in the framework of this project. The results are not presented here. They are published in [9] and [10].

### 2.4.1 Nanocrystalline Materials

Nanocrystalline materials<sup>3</sup> are one group of nanostructured materials which allow different material property modifications. Nanocrystalline materials are metastable structures which are far from thermodynamical equilibrium. They are composed of very small crystallites with a size of a few nanometers ( $< 100$  nm [45], [46]). The basic idea of nanocrystalline materials is to increase the amount of disordered solid among nanocrystals. A disordered solid may consist of grain boundaries, phase boundaries, dislocations, glassy (amorphous) matrix or others.

Processing of bulk nanocrystalline materials can in principle be achieved by either “bottom-up” or “top-down” methods [47]. Top-down methods start with a bulk solid and obtain a nanostructure by structural decomposition. Bottom-up methods include processing of clusters, powders, flakes etc, which require subsequent consolidation into bulk material. Generally, the goal of particle consolidation is to obtain 100% theoretical density and good particle bonding. At the same time, grain growth of nanocrystalline grains has to be avoided or limited. In order to obtain material with nanocrystalline grain size, nucleation events should be favoured over growth.

One approach to achieve nanocrystalline materials is based on the complete or partial crystallization of metallic glasses, which are used as precursors. In case of Al-rich metallic glasses [17], [18], nanocrystalline structures can be basically tailored and controlled by:

1. rapid quenching of a melt.
2. plastic deformation of a crystalline solid.
3. annealing of amorphous phases.
4. plastic deformation of amorphous phases.
5. combination of item 1-4.

Nanocrystalline materials show a wide range of unique mechanical properties, from high toughness, long fatigue life to good wear resistance [45]. At the same time, they can show completely brittle, ductile or superplastic behavior [45], [48], [49]. Moreover, nanocrystalline materials can exhibit higher temperature stability compared to conventional crystalline materials [47], [50].

---

<sup>3</sup>In scientific literature, nanocrystalline materials are also called ultra-fine grained materials, nanophase materials or nanometer-sized crystalline materials [44]. This work refers to the term nanocrystalline materials.

### 2.4.2 Hot Pressing

Powder consolidation by means of hot pressing involves heating and compression of powder particles which are fitted tightly in a die cavity. During processing plastic deformation, creep, and diffusion occur causing denser compact bulk materials. Sintering is not necessarily a required processing step. Plastic deformation becomes more difficult as lateral and axial pressures in the die approach equality, similar to a hydrostatic state [51].

### 2.4.3 High Speed Sintering

Sintering is a powder consolidation method, which effects powder particle bonding by heating below the melting temperature  $T_m$ . In one-component systems, typical sinter temperatures range between  $2/3 T_m$  and  $4/5 T_m$  [ $T$  in K]. For multi-component systems with a melting interval, typical sintering is processed at temperatures in the vicinity of the solidus temperature of the phase with the deepest melting point [52]. Since the material transport responsible for particle bonding is governed by diffusion only, conventional sintering processes require long durations [51]. High speed sintering involves fast heating to the sintering temperature (e.g 60 s). Sintering methods can be assisted by applying uni-axial or hydrostatical pressure.

### 2.4.4 Sparc Plasma Sintering

Sparc Plasma Sintering (SPS<sup>4</sup>) comprises the sintering of powders under influence of a current (typically a pulsed DC current) and pressure. Powders are inserted in the die cavity and resistance heating is effected by passing an electrical current through die, and through powder particles. This induces a plasma and sparks through the powder. High temperatures are generated at the points of contact between adjacent powder particles which causes bonding. In this process, heating is different from hot pressing or sintering, as the powder is not heated via the die. A further difference between SPS and conventional hot pressing is the applied heating rate, which can be as high as 1000°C/min if necessary [53]. Advantages of SPS compared to pressureless sintering and hot pressing include lower sintering temperatures and shorter holding times [51], [53].

### 2.4.5 Direct Extrusion

In powder consolidation by direct extrusion, metal powders undergo plastic shear deformation (usually at elevated temperatures) while pressing a powder billet of diameter  $D_{billet}$  through a die with smaller diameter  $D_{die}$ . An extrusion ratio  $R$  with  $R = D_{billet}^2 / D_{die}^2$

---

<sup>4</sup>It should be noted that SPS is a registered trademark. Besides SPS, further terms are used interchangeably in scientific literature such as Pulsed Electric Current Sintering (PECS), Plasma Assisted Sintering (PAS), Electroconsolidation and Electric Pulse Assisted Consolidation (EPAC) [53]. This work refers to the term SPS.

can be determined expressing a measure for the amount of plastic deformation subjected during extrusion. According to [50], an effective logarithmic strain  $\epsilon_{eff}$  is given by:

$$\epsilon_{eff} = 2 \times \ln \sqrt{R} = 2 \times \ln \sqrt{\frac{D_{billet}^2}{D_{die}^2}} \quad (2.5)$$

In this work, extrusion ratios of 11/1 and 4/1 were used yielding  $\epsilon_{eff}$  of 2.4 and 1.4, respectively. Extrusion can produce densified and elongated form bulk material. Sintering is not necessarily required [54]. Besides, extrusion is a continuous process compared to hot pressing, HSS, and SPS.

### 2.4.6 Equal Channel Angular Pressing

Powder consolidation by equal channel angular pressing (ECAP<sup>5</sup>) involves pressing of samples through a die containing two channels with equal cross section, which intersect at an angle  $\phi$ . The sample undergoes simple shear deformation by retaining the cross sectional area while pressing the sample through the channel intersection. As result of pressing pressure and shear straining, powder particles can be consolidated to bulk materials. Similar to extrusion, ECAP can be a continuous process such as the ECAP-conform process [56].

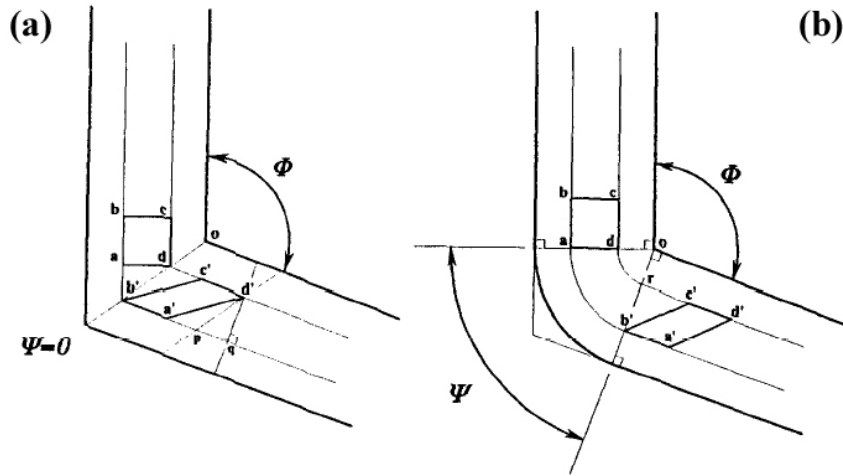


Figure 2.6: Principle of ECAP where  $\phi$  is the angle of the intersection of two channels and  $\psi$  is the outer corner curvature angles [57].

Based on geometrical considerations, the shear strain  $\gamma$  induced by ECAP can be calculated by [57]:

$$\gamma_{xy} = \gamma = 2 \cot\left(\frac{\phi}{2} + \frac{\psi}{2}\right) + \psi \cos\left(\frac{\phi}{2} + \frac{\psi}{2}\right) \quad (2.6)$$

<sup>5</sup>The terms ECAP and ECAE (Equal Channel Angular Extrusion) are used interchangeably in scientific literature. Since no cross sectional reduction of the work-piece occurs, as in common extrusion, this thesis refers to the term ECAP. It should be noted that ECAE is a registered trademark [55].

where  $\phi$  and  $\psi$  denote an inner channel intersection angle and an outer corner curvature angle, respectively, as shown in figure 2.6. A comparison of shear strain values with strain values of other deformation schemes can be achieved by calculation of equivalent strain  $\epsilon_{eq}$  according to von-Mises criterion [57]:

$$\epsilon_{eq} = N \left( \frac{\gamma_{xy}}{\sqrt{3}} \right) \quad (2.7)$$

where  $N$  denotes the number of ECAP passes. In this work, two different ECAP tools were used. Equivalent strains  $\epsilon_{eq}$  induced by conventional ECAP die and zic-zac ECAP die are 1.2 and  $2 \times 0.7$ , respectively.

### 2.4.7 High Pressure Torsion

High pressure torsional straining can be used to consolidate metal powders [58]. Metal powder is compressed between two anvils applying high pressures of several GPa. The rotation of one anvil imposes a large shear strain through friction forces between powder and anvils. A disc shaped specimen is the product.

Different relationships can be used to determine strain values [13]. Based on geometrical considerations, the shear strain  $\gamma$  along the disc radius  $R$  can be estimated by [13]:

$$\gamma = \frac{\vartheta R}{L} = \frac{2\pi NR}{L} \quad (2.8)$$

where  $\vartheta$ ,  $N$  and  $L$  is the rotation angle in radians, the number of full rotations and disc thickness, respectively. For example, a disc used in this work with an 8 mm diameter, 100  $\mu\text{m}$  thickness, and  $360^\circ$  rotation yields a shear strain of 40. According to [7], this large strain seems to be unrealistic regarding deformation of metallic glasses at room temperature. Therefore, logarithmic shear strain relationships can provide more realistic shear strain values. According to [13], the true shear strain  $\gamma_{tr}$  is given by:

$$\gamma_{tr} = \ln \left( \frac{\vartheta R}{L} \right) \quad (2.9)$$

yielding a maximum true shear strain  $\gamma_{tr}$  of 3.7 at edge of the disc with dimensions as described before. In order to compare between shear straining by HPT and straining by other deformation techniques, equivalent strains  $\epsilon_{eq}$  according to von-Mises criterion can be determined by [7]:

$$\epsilon_{eq} = \frac{2}{\sqrt{3}} \gamma_{tr} \quad (2.10)$$

The maximum equivalent strain  $\epsilon_{eq}$  at the disc edge is 4.3.

## 2.5 Al-based Metallic Glasses

### 2.5.1 Structure and Glass Forming Ability

In the late 1980s, Inoue and coworkers discovered (independently to a French and a US-American group) multi-component aluminum-based metallic glass alloys, which contain as main constituents transition metals (TM) and rare earth elements (RE) [59].

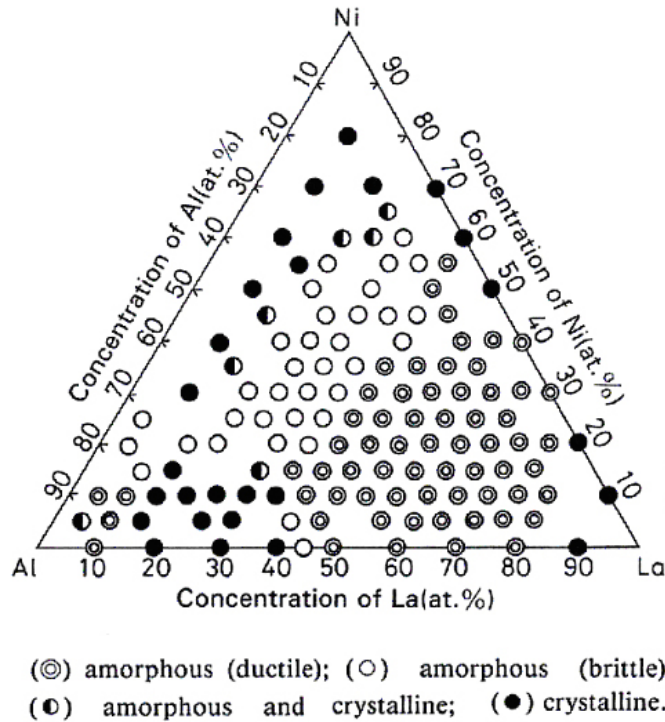


Figure 2.7: Composition range in which an amorphous phase is formed in Al-Ni-La system by means of melt spinning and compositional dependence of bending ductility. [60].

So far, the best GFA in Al-based systems was discovered in ternary Al-Ni-La alloy. Melt-spun ribbons with high bending ductility (so-called ductile glasses) were obtained using alloys with high Al content of  $\geq 85$  at-% as base component or high a La content ranging from 35 to 83 at-%, as illustrated in figure 2.7. La-rich Al-Ni-La alloys have superior GFA compared to Al-rich glasses. They show extended supercooled regions prior to crystallization ( $T_x - T_g = 60 - 69^\circ\text{C}$ ) and require low critical cooling rates. La-rich BMGs with a 30 mm diameter were recently achieved [26]. However, La-rich amorphous alloys are still too expensive compared to Al-rich alloys. Al-rich amorphous alloys can be a suitable, less expensive alternative with lower GFA yielding fully amorphous samples with a maximum thickness of 30-40  $\mu\text{m}$ . One can measure a glass transition when the alloying content exceeds 13%. These Al-based metallic glasses with Ni+La content  $> 13\%$  show supercooled regions prior to crystallization  $T_x - T_g$  ranging from 12 to  $18^\circ\text{C}$  [61]. Their reduced glass transition temperatures  $T_{rg}$  is approximately 0.5 [61].

The structure of Al-rich Al-Ni-La alloys can be discussed in the light of hard-sphere dense-random packing model (DRP) which was used to fit X-ray absorption fine structure (XAFS) measurements [62]. Al-La clusters in amorphous  $\text{Al}_{89}\text{La}_6\text{Ni}_5$  alloy have a coordination number of 12, which is similar to that of an icosahedron or a fcc-crystal. On the contrary, Al-Ni and Al-Al interatomic distances are anomalously short and do not fit the data obtained by the DRP model. Furthermore, the Al-Ni clusters have a coordination number of 6 which differs from the corresponding distances of stable crystalline  $\text{Al}_3\text{Ni}$ . These results indicate a strong interaction between Al and Ni atoms, which might be due to covalent bonding character between Al and Ni atoms.

Amorphous phases in Al-rich glasses obtained by either rapid quenching or solid state reaction can differ in their properties. Low strain rate cold rolling subjected to amorphous  $\text{Al}_{92}\text{Sm}_8$  leads to stable glasses, whereas melt spinning of the same composition leads to a metallic glass with quenched-in nuclei [63]. This is confirmed by fluctuation electron microscopy investigations, which reveal a fcc-Al-like medium range order in rapid quenched amorphous  $\text{Al}_{92}\text{Sm}_8$  alloy but not in cold rolled amorphous  $\text{Al}_{92}\text{Sm}_8$  alloy [64]. The investigations suggest the existence of quenched-in nuclei in rapidly quenched Al-rich metallic glasses. This corresponds to non-statistical element distributions detected by atom-probe in the as-quenched state of  $\text{Al}_{89}\text{Ni}_6\text{La}_5$  alloy [65], also indicating quenched-in nuclei. Rapidly quenched marginal glass formers can be stabilized when the cooling rate is as high as possible to avoid nucleation during quenching or when a compositional change enhances GFA [4].

## 2.5.2 Crystallization Behavior

Prior to crystallization, the amorphous phase in Al-based metallic glass can decompose into amorphous phases with different compositions upon heating. This was observed in  $\text{Al}_{89}\text{Ni}_6\text{La}_5$  alloy [65],  $\text{Al}_{92}\text{Sm}_8$  alloy [64], and  $\text{Al}_{88}\text{La}_2\text{Gd}_6\text{Ni}_4$  alloy [66].

Generally, Al-rich amorphous alloys undergo a two-stage crystallization process upon heating. The first transformation involves primary crystallization of fcc-Al within the amorphous matrix. The second transformation involves devitrification of the residual amorphous matrix into several intermetallic compounds [59]. It was observed that primary crystallization of fcc-Al in rapid quenched Al-Ni-Ce(-Cu) [67] and Al-Ni-La glasses [65], [68], [69] leads to solute partitioning. The decreased solubility of solute atoms in the crystal induces solute enriched regions around the crystal. This influences growth kinetics of the fcc-Al crystals into the residual amorphous matrix [18].

It has been recently reported that in annealed melt-spun Al-Ni-La ribbon occurs a drop of microhardness after crystallization is completed [68], [69]. This may limit the potential use of such alloys in structural parts, where a certain level of ductility is required. Considering the consolidation of amorphous alloys to achieve nanocrystalline materials, low temperature consolidation strategies are required to avoid complete crystallization.

In a few Al-rich amorphous alloys, metastable phases can form. The existence of metastable phases in Al-Ni-RE alloys depends on the atomic radius of the rare earth. The smaller the atomic radius of the rare earth element, the higher the probability of the

formation of these metastable phases [70]. In Al-Ni-La system, a metastable bcc phase depending on the Ni and La concentration can occur [68], [69], [71].

Crystallization induced by plastic deformation was observed after bending of amorphous melt-spun ribbons [1], [5], cold rolling [72], nanoindentation [6] and high pressure torsion [7], [17], [73]. Compared to crystallization after annealing: morphology, number density of strain-induced crystals, and crystallization sequence can alter during plastic deformation at temperatures below the onset of crystallization.

### 2.5.3 Consolidation of Amorphous Powders

Successful attempts of consolidating, shaping and forming metallic glasses into complex shaped components were made using alloys with a wide supercooled region. In this region between  $T_g$  and  $T_X$ , metallic glasses have a lower viscosity and can be formed very similar to plastics under similar processing temperatures and pressures. One example is the extrusion in the supercooled region of amorphous He-atomized Zr-based metallic glass powders [74]. The as-extruded samples were still amorphous and had relative density up to 99.9% showing similar strength and fracture properties as the as-cast glassy material. Analogous results have been reported in [75], where Zr-based amorphous powders were consolidated in the supercooled region by means of equal angular channel pressing (ECAP). Furthermore, this concept was recently applied to form micro-electromechanical devices [76].

Consolidation in the supercooled region is also a desirable process strategy for producing bulk Al-rich metallic glasses. However, these glasses are marginal glass formers with either no or only a small supercooled region. Therefore consolidation in the supercooled region cannot be applied to Al-rich metallic glass.

It was observed that consolidation can cause fully, or at least partially crystallization of the amorphous phase [59], even when performed at temperatures below the onset of crystallization. Warm-extruded nanocrystalline bulk Al-Ni-Mn, Al-Ni-Ce and Al-Ni-Y alloy powders can have excellent mechanical properties, like high compressive strength up to 1480 MPa [2], modest ductility or superplasticity during tensile stress at elevated temperatures leading to elongations up to 650% [59].

In addition to extrusion, further consolidation techniques such as hot pressing [77], [78], spark plasma sintering [9], [10] high pressure torsion (HPT) [7], [14], and ECAP [12] were tested. The pressed and sintered materials revealed remaining porosities between 0.1 and 8%, microhardness of maximum 352 HV and high compression strengths between 800 and 1340 MPa after complete crystallization. Fully consolidated samples at room temperature were achieved by means of HPT. Consolidation via ECAP yielded only to a partially consolidated specimen.



## **Chapter 3**

# **Experimental Procedures**

## 3.1 Processing of Al-Ni-La Metallic Glasses

### 3.1.1 Synthesis of Master Alloys

Ingots of nominal composition used for splat quenching were prepared by alloying pure elements Al (99.999%), Ni (99.95%) and La (99.5%) by induction melting in a high frequency electromagnetic levitation furnace under a purified argon atmosphere. The levitated melt was kept at high temperatures until the surface oxide skin broke up. After 2 to 7 min of holding, the high frequency current was switched off and the levitated melt fell down into a water chilled copper crucible, where it solidified forming a crystalline ingot. This procedure was repeated several times to ensure the homogeneity of the alloy. Further information about the process is given in [79] and [80]. The master alloy of amorphous Al alloy powder was synthesized in the atomizer, as described in chapter 3.1.2.

### 3.1.2 Rapid Solidification by Gas Atomization

In this work, Al<sub>87</sub>Ni<sub>8</sub>La<sub>5</sub> and Al<sub>85</sub>Ni<sub>10</sub>La<sub>5</sub> alloys were gas-atomized by Nanoval G.m.b.H. using the “Nanoval” process [40]. The master alloys were prepared in the atomizer. Prior to processing, the whole atomizer was evacuated and subsequently flooded with argon gas for 15 min. Al<sub>87</sub>Ni<sub>8</sub>La<sub>5</sub> and Al<sub>85</sub>Ni<sub>10</sub>La<sub>5</sub> alloy were synthesized in a graphite crucible and an alumina crucible, respectively, by induction melting under an argon atmosphere, using pure elements Al(99.98%), Ni(99.7%) and La(99.7%). The melt of Al<sub>87</sub>Ni<sub>8</sub>La<sub>5</sub> and Al<sub>85</sub>Ni<sub>10</sub>La<sub>5</sub> alloy were heated up to approximately 1100°C and 1200°C, respectively, and were subsequently gas-atomized using helium or argon gas. The gas-pressure was controlled manually and could reach maximum 30 bar. Atomization yielded two powder fractions: a coarser major powder fraction collected in the atomizer’s recipient and a finer minor powder fraction collected in the cyclone. A slow oxidation of the as-atomized powder was allowed by flooding the atomizer with air. When the powder was removed from the atomizer, each fraction was mixed manually in air for about 1 min. The as-atomized powder was stored in air under ambient temperature and humidity. Due to the atomizer’s capacity, alloys of 1 kg per batch were synthesized and atomized obtaining approximately 750 g powder per batch. A residue of alloy and slag remained non-atomized in the melting furnace.

### 3.1.3 Rapid Solidification by Splat Quenching

Thin sheets (splats) of rapidly solidified Al-Ni-La alloy were produced under vacuum of  $\approx 10^{-5}$  mbar using a Buehler G.m.b.H. twin piston splat cooler. The splat thickness which was necessary to achieve amorphous samples ranged from 35 to 45  $\mu\text{m}$ . The necessary master alloys were prepared from ingots which were cut into cubes of approximately  $2 \times 2 \times 2 \text{ mm}^3$ .

### 3.1.4 Rapid Solidification by Melt Spinning

Melt spinning experiments were performed in the framework of a students project at the Hahn-Meitner-Institute, Berlin. In this project, the influence of process parameters on properties of Al-Ni-La melt-spun ribbons was investigated. The results are shown in [37].

## 3.2 Annealing

Annealing experiments were carried out using a differential scanning calorimeter (DSC) to investigate phase transformations upon annealing. The device is described in chapter 3.4.6.

Continuous heating of powder samples was realized by applying rates between 20 and 40°C/min. At different given temperatures, heating was interrupted and the samples were cooled down with a cooling rate of approximately 100°C/min. Isothermal annealing was performed by heating up the sample at 80°C/min to the desired dwelling temperature. After dwelling at the given temperature, the samples were cooled down with a cooling rate of about 100°C/min.

The samples were placed in open Al pans. Prior to annealing, the DSC furnace was 3 times evacuated and subsequently flushed by a argon gas stream. During annealing, the furnace was purged by constant argon gas flow of about 20 ml/min.

## 3.3 Consolidation of Al-based Metallic Glass Powder

### 3.3.1 Hot Pressing

Powder consolidation of partially crystalline  $\text{Al}_{87}\text{Ni}_8\text{La}_5$  and amorphous  $\text{Al}_{85}\text{Ni}_{10}\text{La}_5$  powders were performed by uni-axial hot pressing at 637 and 955 MPa load, respectively, using a 20 mm diameter cylindric pressing die. A single action ram hydraulic press was used to apply the load. Except for cold pressing, the entire die was heated by means of a heating sleeve. The pressing temperature was measured in the die, close to the cavity. Pressing temperatures ranged from room temperature to 370°C, which was the upper temperature limit of the die used. Boron nitride (BN) lubricant was used to improve ejection of the pressed material from the die. The pressing process was employed as follows: Approximately 11 g of powder was filled into a BN coated cold die and closed between bottom and top punch applying the whole process load for 5 s. The filled die was removed from the press and heated up to process temperature. After reaching the final temperature, the die was kept for 5 min at the temperature set. Afterwards, the hot die was moved back between upper and lower ram and the actual hot pressing process was started. During hot pressing, the temperature was kept constant. A constant load was difficult to achieve because of the rough load control of the hydraulic press. After hot pressing, the sample was removed from the hot die within approximately 3 min and was subsequently water quenched.

### 3.3.2 High Speed Sintering

One high speed sintering (HSS) experiment of amorphous  $\text{Al}_{85}\text{Ni}_{10}\text{La}_5$  powder was performed at the Powder Technology Center of the Austrian Research Centers (ACR) Seibersdorf. Prior to sintering, the powder was filled into a graphite mold and degassed until a vacuum of  $10^{-5}$  mbar was achieved. Sintering was performed under 50 MPa uni-axial load by applying fast heating of the graphite mold to 400°C sintering temperature within 1 min. The sintering temperature was kept constant for about 30 s.

### 3.3.3 Sparc Plasma Sintering

Consolidation of amorphous  $\text{Al}_{85}\text{Ni}_{10}\text{La}_5$  powder by sparc plasma sintering was performed at the National Institute for Materials Science (NIMS) in Tsukuba, Japan. The sintered samples were investigated at lieu and the results are presented in [9]. Further SPS experiments on partially crystalline  $\text{Al}_{87}\text{Ni}_8\text{La}_5$  were performed at the Research Center for Machine Parts and Materials Processing, University of Ulsan, Republic of Korea and investigated at the IFW Dresden, Institut fr Komplexe Materialien, Germany. The results are presented in [10]. They will be discussed in the light of the comparison of different consolidation techniques.

### 3.3.4 Direct Extrusion

Direct extrusion of partially crystalline  $\text{Al}_{87}\text{Ni}_8\text{La}_5$  powder was performed at the Institute of Materials Machine Mechanics (IMMM) of the Slovak Academy of Sciences (SAS) Bratislava, Slovak Republic. A 45° conic faced die and a flat face die were used with an extrusion ratio of 11/1 and 4/1, respectively. Loose and cold isostatically pressed powders were canned in commercial Al profiles of 20 mm outer diameter in which a 16 mm hole was drilled. Extrusion was carried out at 200 and 300°C. The samples were preheated to process temperature for 15 min and subsequently extruded by means of a hydraulic single action ram press. Graphite was used to reduce friction between sample and feeding channel. A detailed description of the set-up used is given in [50].

### 3.3.5 Equal Channel Angular Pressing

Equal channel angular pressing (ECAP) of as-atomized  $\text{Al}_{85}\text{Ni}_{10}\text{La}_5$  powder was carried out at the IMMM of the SAS Bratislava. A single action ram hydraulic press was used to press the sample through the ECAP die. Two ECAP dies were used as illustrated in figure 3.1. They are called in the following “conventional ECAP die” and “zic-zac ECAP die”. The conventional ECAP die consists of two square channels with  $12 \times 12 \text{ mm}^2$  cross section, which intersect perpendicular ( $\phi = 90^\circ$ ). The channel intersection has square corners (corner curvature angle  $\psi = 0^\circ$ ). The zic-zac ECAP die consists of two square channels parallel to the pressing direction with channel cross section of  $12 \times 12 \text{ mm}^2$ . The exit channel is shifted perpendicular to the pressing axis creating two corners with channel

intersection angles of  $\phi = 110^\circ$ . Inner and outer corner curvature angles are  $\psi = 0^\circ$  and  $\psi = 15^\circ$ , respectively. A further detailed description is given in [81] and [55].

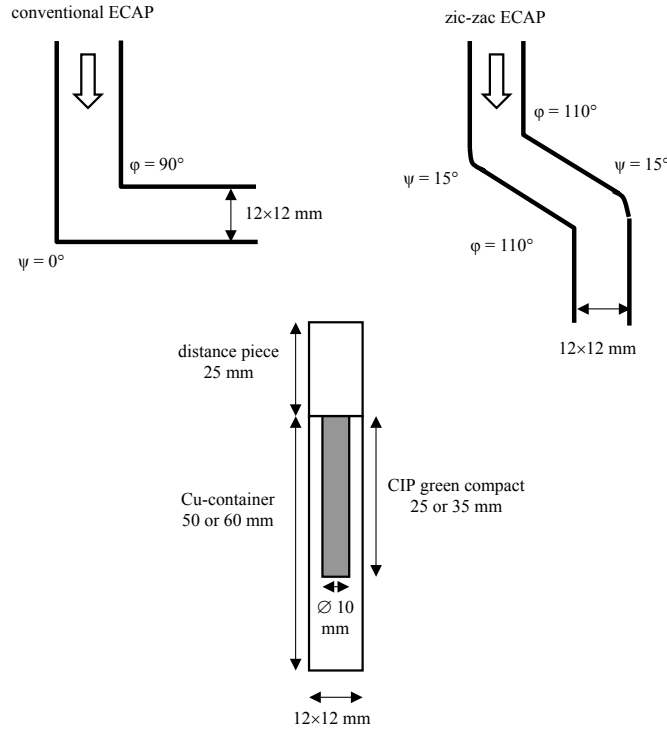


Figure 3.1: Schematic view of conventional and zic-zac ECAP dies [81].

Figure 3.2 shows the procedure how consolidation of as-atomized  $\text{Al}_{85}\text{Ni}_{10}\text{La}_5$  powder was performed. Prior to ECAP, as-atomized powder were precompacted by cold isostatic pressing (CIP). Rubber cylinders were filled with powder and degassed to approximately  $10^{-2}$  mbar. Sealed cylinders were cold isostatically pressed at room temperature applying a pressure of 1 GPa for approximately 2 min. After CIP, the powder had a temperature of approximately  $60^\circ\text{C}$ . Cold isostatically pressed samples were turned to cylinders of 10 mm diameter. Specimens of 26 and 36 mm length were cut from cylinders and inserted into copper containers of 50 and 60 mm length, respectively. The containers were made of commercial copper profiles with a square cross section of  $12 \times 12$  mm into which holes of 10 mm diameter and 25 or 35 mm depth were drilled. Pieces of 25 mm length of plain copper profile were used as distance pieces to press the specimen completely through the ECAP die, see figure 3.1. ECAP of canned samples was done at different temperatures using either the conventional or the zic-zac ECAP die. The ECAP die was heated up to processing temperature and was held constant throughout the whole process. After 10 to 15 min of holding at process temperature, the graphite-coated canned specimen was inserted into the entrance channel of the hot ECAP die. The specimen rested there for about 5 min. Afterwards, one ECAP pass was preformed. The deformed specimen remained approximately 2 min in the hot die, before it was removed and water quenched.

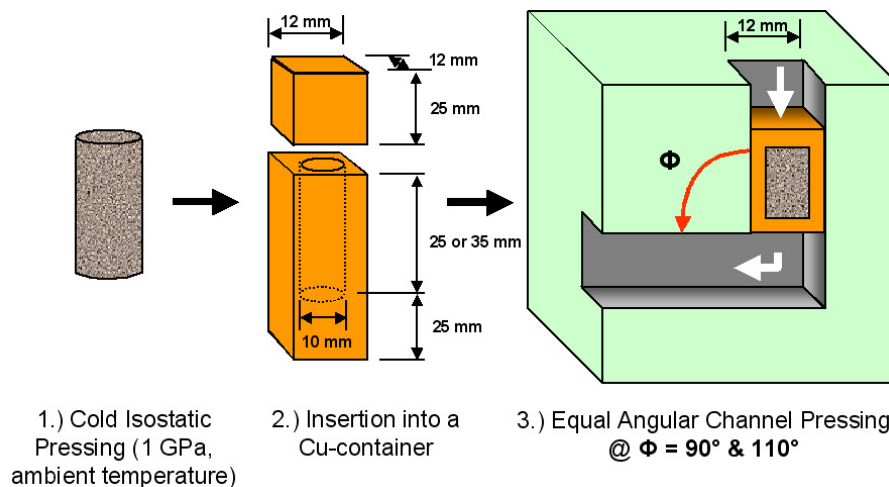


Figure 3.2: Experimental scheme of the consolidation by means of ECAP.

### 3.3.6 High Pressure Torsion

In this project, high pressure torsion (HPT) was performed at the Institute of High Pressure Physics, Ural Branch of the Russian Academy of Sciences in Yekaterinburg, Russian Federation. The HPT set up consisted of a hydraulic press, where the lower anvil is driven by an electric motor via reduction gears rotating around its vertical axis. The anvils were of Bridgeman [82] type geometry with a working area made of tungsten carbide. Amorphous  $\text{Al}_{85}\text{Ni}_{10}\text{La}_5$  powders were subjected to HPT at room temperature under uni-axial pressure of 6 GPa and an angular speed of the rotating anvil of  $0.3 \text{ min}^{-1}$ . Four discs were prepared using 5, 15, 45, and 360 degrees of torsion. In the following, these discs are named D5, D15, D45 and D360.

## 3.4 Sample Analysis

### 3.4.1 Density Measurements

Densities of consolidated samples were determined according to Archimedes' principle using a Sartorius scale BP211D and high purity ethanol. Each measurement was repeated three times. Mean values and standard deviations were calculated.

### 3.4.2 Vickers Microhardness

Hardness measurements were used to obtain information about inter particle bonding and phase transformations after consolidation. Polished longitudinal cross sections (in pressing direction) of ECAP and hot pressed samples were used as indentation plane. Vickers microhardness measurements were carried out by means of a Reichert-Jung MHT-10 using 200 g load, 20 s slope and 15 s dwelling time. Mean values and standard deviations

were determined using 15 indents per sample. The indents were set in appropriate distances taking into account the impact of the indent deformation zone.

### 3.4.3 Granulometry

Particle size distributions of as-atomized powders were measured with a CILAS 715 particle analyzer by NANOVAL G.m.b.H. Berlin. Powder samples were dispersed in a ultrasound-assisted water bath. Laser diffraction spectrometry was used to determine the particle size distribution of solute particles. The diffraction spectra were analyzed using the Fraunhofer approximation which is valid for particles larger than 2  $\mu\text{m}$  [83]. The acquisition of particle size distribution was repeated 2 to 3 times extracting samples from different places of the powder batch in order to proof the reliability of the measurement.

### 3.4.4 Hot Gas Extraction

The oxygen content of Al-Ni-La powder was determined by carrier gas hot extraction [84] using a nitrogen/oxygen analyzer Horiba EMGA 620 WC. The experiments were performed at the Institute of Ceramic Materials of the Berlin University of Technology. This method involves the quantitative reduction of oxygen in the sample, the release of gaseous reaction products, and their selective and quantitative detection. Approximately 5 mg of powder were first filled into a tin, then into a nickel capsule. Encapsulated samples were inserted into a graphite crucible which was electrically heated up to about 2500°C for 40 s. The capsules act as metal additives to obtain a homogeneous reduction-assisted melt. At these high temperatures, oxygen of the sample reacts with carbon forming carbon monoxide, which was detected by infrared absorption analysis. Hot gas extraction measurements were repeated once in order to proof reproducibility. It was found that absolute values differ by approximately 50% and are therefore not reliable. However, measurements show that relative changes of the oxygen content related to the powder particle diameter are similar. The results will be discussed only in the context of relative changes.

### 3.4.5 Inductively Coupled Plasma Mass Spectroscopy

Quantitative element analysis of Al-Ni-La alloys were done by inductively coupled plasma mass spectroscopy (ICP-MS) measurements, performed at the department SF6 (Spurenelemente) of the Hahn-Meitner-Institute, Berlin. Three replicates of approximately 10 mg per sample were prepared by dissolving the sample material in highly concentrated  $\text{HNO}_3$  (400  $\mu\text{l}$ ) under stepwise heating from 60 to 90°C and continuous shaking. Data analysis was done assuming that only Al, Ni and La are present in the sample material. The peak intensities of Al and Ni relatively to La were determined. Mean values were calculated from 30 measurements per sample. Relative intensities of the sample referred to the standard solution yielded the stoichiometric concentration of the sample. The results presented here are the calculated mean of three replicates per sample. The

estimated error is approximately 0.1 at.-%. Further details about the data analysis is given in [85].

### 3.4.6 Differential Scanning Calorimetry

In this work, differential scanning calorimetry (DSC) measurements were used to investigate phase transformations upon annealing of amorphous precursor materials (powder, splats, ribbons) and consolidated samples. DSC experiments were performed in a flowing argon atmosphere using a Perkin-Elmer DSC Pyris 1. The Pyris 1 is a power compensation DSC, which can run isothermal and continuous<sup>1</sup> heating experiments. The signal of a power compensation DSC is related to the differential heat provided to keep sample and reference to the same temperature. Due to the fact that sample furnace and reference furnace have different thermal properties, a baseline has to be recorded to eliminate device errors. Baseline drift, resulting from thermal balances between sample and reference furnace, can be reliably corrected within 1 hour of isothermal heating. The initial transient during isothermal heating is less than 1 min. Further information is given in [86] and [87]. The DSC device was calibrated using pure In and Zn. The accuracy of temperature and electrical power is about  $\pm 0.3^\circ\text{C}$  and  $\pm 0.02\text{ mW}$ , respectively.

Continuous heating experiments were carried out using heating rates between 5 and  $80^\circ\text{C}/\text{min}$ . Continuous heating at  $20^\circ\text{C}/\text{min}$  of all as-atomized powders was repeated 3 times in order to prove the reliability of DSC measurements. The repeated measurements showed qualitatively identical curves. Isothermal heating experiments were performed in a way that samples were heated up to the desired dwelling temperature using a rate of  $80^\circ\text{C}/\text{min}$ . As soon as the desired temperature was achieved, it was held constant for 1 hour. After the first run of any experiment, the fully crystallized specimen was heated again under identical conditions in order to determine the baseline. The baseline was subtracted from first run data, when necessary. Peak minimum, onset temperatures and peak areas were extracted from DSC curves. Figure 4.3(b) and (c) illustrate the tangent construction used to determine onset temperatures of glass transition  $T_g$  and crystallization  $T_X$ , respectively. Their values varied within the accuracy of setting the tangents on the DSC curve yielding an overall error of approximately 1%. In addition, Kissinger analysis was applied in order to determine activation energies of phase transformations in as-atomized powders. The procedure used is described in [88], [89]. The analysis required DSC data from continuous heating experiments performed at different heating rates between 5 and  $80^\circ\text{C}/\text{min}$ .

No special sample preparation was required. The samples were cut in a way that they just fitted into the Al pan.

---

<sup>1</sup>The terms continuous heating, isochronal heating and scanning experiments are all used in scientific literature. This work prefers the term continuous heating.

### 3.4.7 Scanning Electron Microscopy

Powders and consolidated samples were investigated by scanning electron microscopy (SEM) using both a Philips XL30 ESEM and a Zeiss CrossBeam 1540ESB operating between 5 and 20 kV. Surface and morphology analysis of powders and consolidated samples were performed without any sample preparation. Cross sectional analysis was carried out on polished samples. Different imaging modes were used: secondary electron (SE) and in-lens detected secondary electrons yielding images with a topological contrast; and back scattered electron (BSE) images yielding a phase specific contrast.

SEM images and the free-source software ImageJ were used to determine the plastic strain of elongated powder particles and their rotation with respect to the entrance channel of the ECAP die (figure 5.16). The cross sectional surfaces of each powder particle was fitted by an ellipse. The ellipse area, its length along major axis  $a$  and minor axis  $b$  were determined. Between 20 and 40 powder particles were measured per SEM-image yielding a median value, its first and third quartile. The first and third quartile denote the 25% and 75% point of the cumulative distribution function of powder particle diameters. Assuming that the material is incompressible, the ellipse area is equal to the circle area of the initially spherical as-atomized powders. Consequently, a median circle diameter  $d_{50}$  was determined from the measured ellipse areas. Median length of major axis  $a$ ,  $a_{50}$ , and median circle diameter yield a strain value  $\varepsilon = (a_{50} - d_{50})/d_{50}$ . Alternatively, the strain along the minor axis  $b$  is  $\varepsilon = (d_{50} - b_{50})/d_{50}$ . Moreover, the rotation of powder particles is specified by the angle  $\alpha$  between entrance channel and major axis  $a$ .

### 3.4.8 Transmission Electron Microscopy

Transmission Electron Microscopy (TEM) was used when looking at very fine microstructures, especially when analyzing the crystallization products of the metallic glass. Contrary to X-ray diffraction, TEM is a technique to obtain local information. TEM experiments were performed using a Philips CM30, which was operated at 300 kV permitting a satisfactory transmission of metallic samples up to about 80 nm thickness. Bright field (BF), dark field (DF) and electron diffraction (D) images were taken using AGFA films and imaging plates.

Crystallite size measurements presented in figure 4.16(b) and 4.9(b) were carried out using TEM-images and the free-source software "ImageJ". At first, crystallite cross sections were fitted by polygons and the crystallite cross sectional area was calculated. The polygon area was considered to be a circle area assuming that crystals are spherical. Consequently, a crystallite diameter was determined. It has to be noted that only relative crystallite size changes can be discussed since the crystallite cross sections in a TEM sample do not necessarily cross the center of the sphere. The crystallites in figure 4.16(b) were measured at 2 different sample positions of only one annealed powder particle. This yielded 36 crystallites for a powder particle continuously heated up to 205°C. For powder particles continuously heated up to 220°C, 285°C, 312°C, 358°C, this yielded 15, 13, 11, 9 crystallites, respectively. Median crystallite diameters, the first, and the third quartile were calculated.

Electron diffraction served to identify crystalline phases by comparing diffraction patterns with PDF-2-data of the International Center for Diffraction Data. Debye-Scherrer diffraction rings were tangentially integrated to achieve diffraction intensity profiles. The length scale of the  $2\Theta$ -axis was calibrated using electron intensity profiles of pure gold, which were recorded under identical conditions as those of the samples. The gold standard consisted of a Au sputtered carbon grid. The d-values were calculated by Bragg's law using a wavelength of 0.00197 nm, which corresponds to an acceleration voltage of 300 kV [90].

TEM-samples of powders were prepared by embedding powder particles in a medium which had mechanical properties and a sputter yield similar to that of amorphous and nanocrystalline powders. First, an epoxy resin was mixed with titanium nitride powder (particle size ranging from 2 to 5  $\mu\text{m}$ ). Afterwards, a small amount of amorphous or nanocrystalline powder was added and mixed. The mixture was hardened at 80 °C for 30 min yielding a compact and well machinable block. From this block thin slices between 5 and 8  $\mu\text{m}$  thickness were cut and were mechanically polished. Final thinning was done by ion milling. Further information about the TEM-sample preparation is given in [91]. Electro-polishing of powder samples failed.

### 3.4.9 X-ray Diffractometry

X-ray diffraction (XRD) was used to identify and analyze amorphous and crystalline phases. An incident coherent X-ray beam scatters elastically at electron shells of sample atoms. In crystalline materials, a constructive interference of diffracted X-rays leads to discrete maximum intensities at certain angles  $\Theta$ , which correspond to the spacing of crystal lattice  $d_{hkl}$ , expressed by the Bragg formula:

$$n\lambda = 2d_{hkl}\sin\Theta \quad (3.1)$$

where  $\lambda$  denotes the wavelength of X-ray radiation used, and  $n$  is an integer denoting the order of the scattering maximum. In the following, discrete maximum intensities of the diffracted beam are named either Bragg reflections or Bragg peaks. Compared to coherent scattering in a single crystal, crystalline powders and nanocrystalline bulk materials show cones with a semi angle  $2\Theta$  (Debye-Scherrer rings). Debye-Scherrer rings stem from a sum of Bragg reflections of randomly oriented crystallites [92],[93]. Decreasing crystallite sizes are associated with a broadening of Bragg reflections. This effect can be used to estimate the crystallite size  $\langle D \rangle$  by employing Scherrer's Formula [94]:

$$\langle D \rangle = \frac{180}{\Pi} \frac{K\lambda}{\beta(\Theta)\cos\Theta}, \quad K = 0.89\dots 1.39 \quad (3.2)$$

where  $\beta(\Theta)$  is the full-width-at-half-maximum (FWHM) of a Bragg reflection at Bragg angle  $\Theta$ ,  $\lambda$  is the wavelength and  $K$  is a constant expressing the shape of the crystal. Considering a spherical crystal shape,  $K$  is approximately 1.

Amorphous materials have no periodical long range order but a short range order,

which means that only the coordination of a random atom to its neighbor atoms is defined. The correlation of a atom to its neighbors diminishes with increasing distance to second and further neighbor shells. Therefore the scattered intensity does not show discrete Bragg peaks as in crystalline materials but a broad diffuse scattering maximum (amorphous halo) with less intensity. Partial crystallization leads to a superposition of the broad diffuse scattering and discrete Bragg reflections. After complete crystallization only Bragg reflections occur.

In this work, two types of XRD experiments were performed: angle-dispersive (AD) XRD, in which monochromatic radiation is used; and energy-dispersive (ED) XRD, for which the scattering angle is fixed. In energy-dispersive XRD, the photon energy of the reflected X-ray beam is measured. The reflected X-ray beam obeys Bragg's law, and the angle-dispersive Bragg formula changes to:

$$E_{hkl} = h\nu = \frac{hc}{\lambda} = \frac{hcn}{2d_{hkl}\sin\Theta} \quad (3.3)$$

where  $E_{hkl}$  denotes energy of the Bragg reflection  $hkl$ ,  $h$  is Planck's constant,  $c$  denotes speed of light, and  $n$  is an integer of the order of the scattering maximum. ED XRD experiments along the radius of disc D360 were performed at the Berlin synchrotron radiation facility (BESSY). The cross section of the incident beam was  $0.5 \times 0.5 \text{ mm}^2$  permitting a spatial resolution of 0.5 mm. The experimental set-up is schematically illustrated in figure 3.3. A high intensity white X-ray beam was pointed to the disc target and a diffracted beam was recorded in transmission mode at  $2\Theta = 7^\circ$  by means of an energy-dispersive detector. The disc was translated in steps of 0.5 mm along the radius after a measurement was completed. The acquisition time per measurement was 1 hour. Further information about the set-up is given in [95] and [96]. The broad diffuse scattering of the residual amorphous phase was fitted by means of a linear function in the vicinity of the Bragg peak and subsequently subtracted from the superposing Bragg reflection peak. The integral intensity obtained from a fit using the Gaussian function was corrected by the background level in order to take variations in the specimen thickness into account. Peak positions were analyzed by the search and match method using PDF-2-data of the International Center for Diffraction Data.

AD XRD experiments were carried out with a Bruker D8 Advance diffractometer using Bragg-Brentano geometry, Cu  $K_\alpha$  radiation ( $\lambda = 0.15406 \text{ nm}$ ), a secondary graphite monochromator and a scintillation counter detector.  $2\Theta$  scans were performed ranging from  $10$  to  $90^\circ$ , in steps of  $0.02^\circ$  using an acquisition time of 10 s per step. Collimator slits of 0.6 mm were used for incident and diffracted beam. In order to increase the diffracted beam intensity, the sample rotated in horizontal plane around its eucentric point with a speed of 12 rpm ( $\phi$ -circle). The illuminated area achieved was circular with a diameter of 6 mm. Powder samples were poured on a sample holder and pressed obtaining a plane and smooth horizontal surface. Bulk samples after hot pressing and ECAP were ground up to 4000 grains/inch<sup>2</sup> paper. Splats and HPT discs did not require further preparation.

XRD intensity profiles were analyzed by search and match method using PDF-2-data of the International Center for Diffraction Data. Integral intensities of hot pressed powders were determined by fitting broad (111) and (200) fcc-Al Bragg reflections using Gaussian

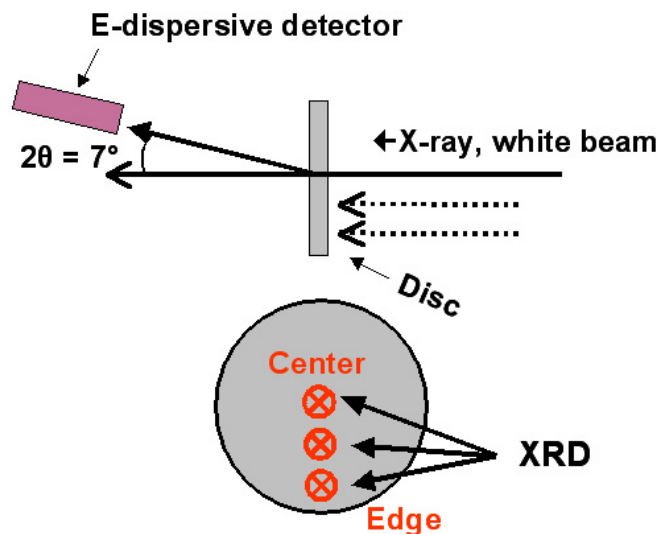


Figure 3.3: Schematic view of the experimental set-up for energy-dispersive XRD measurements along the radius of disc D360.

functions. The broad diffuse scattering of the residual amorphous phase was subtracted by linear function in the vicinity of each Bragg peak. Device errors and emission spectrum are not corrected because only peak intensities of the same Bragg reflections were compared keeping the error constant. Average crystallite sizes were estimated from angle dispersive XRD intensity profiles using a Bruker TOPAS 3 software. The broad diffuse scattering of the residual amorphous phase was fitted by Chebychev polynomial functions and subtracted from the Bragg reflections. Bragg peaks were fitted by Lorentzian functions. Crystallite sizes were determined from FWHM of fitted peaks using Scherrer's equation.

### 3.4.10 Simultaneous In-situ X-ray Attenuation and X-ray Diffraction

Simultaneous in-situ angle-dispersive XRD and X-ray attenuation experiments were performed to monitor in real time the crystallization process of amorphous  $\text{Al}_{85}\text{Ni}_{10}\text{La}_5$  alloy and the associated change in mass density upon annealing. The experiment was performed at BESSY using a monochromatic synchrotron radiation of 8 keV photon energy ( $\lambda = 0.154$  nm). In addition, in-situ XRD without simultaneous X-ray attenuation experiments were carried out on powder samples. A schematic view of the set up used is presented in figure 3.4. Amorphous  $\text{Al}_{85}\text{Ni}_{10}\text{La}_5$  powders were subjected to constant heating at  $10^\circ\text{C}/\text{min}$ , while in steps of 5 s XRD pattern were acquired corresponding to a temperature resolution of approximately  $0.9^\circ\text{C}$ . The accuracy of the heating control during in-situ experiments is approximately 10%. Powder samples were poured on a ceramic sample holder and manually pressed. This assembly was mounted on a resistance heater placed on a goniometer in an evacuated high temperature chamber. The chamber was equipped with a beryllium dome, which is almost transparent for the photon energy used. The diffracted X-rays were acquired by means of a 2D-detector. The distance between specimen and detector was chosen in a way that the  $2\Theta$  range was from  $29$  to  $48^\circ$ , because the

diffuse scattering maximum of the amorphous phase, the (111), and (200) fcc-Al Bragg reflections occur in this range. Temperature control was realized by two thermocouples placed on the sample holder and on the resistance heater, respectively.

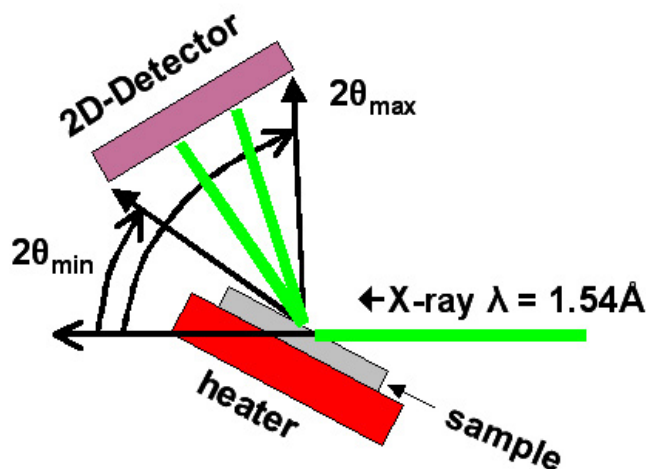


Figure 3.4: Schematic view of the in-situ XRD experimental set-up for powder samples.

Simultaneous in-situ XRD and in-situ X-ray attenuation measurements of  $\text{Al}_{85}\text{Ni}_{10}\text{La}_5$  splats and of D360 sample pieces were performed in transmission mode. For this purpose, the in-situ XRD experimental set-up was slightly modified, as illustrated in figure 3.5. The sample was fixed on a copper sample holder in a way that the incident beam transmitted through the sample. The 2D-detector acquired diffracted X-rays ranging from  $2\Theta = 29$  to  $48^\circ$  with  $2\Theta$  steps of  $0.05^\circ$ , whereas the straight transmitted beam intensity was recorded by a diode rendering information about thermal expansion and thermally induced mass density changes. The illuminated area was  $0.5 \times 0.5 \text{ mm}^2$ . The radiation used had a photon energy of 8 keV. The samples were subjected to continuous and isothermal heating. Twenty XRD pattern per minute were taken during heating the sample. No special sample preparation was performed. The attenuation data were normalized by the incident beam intensity in order to correct the intensity decrease of synchrotron radiation over time. The accuracy of the heating control during in-situ experiments is less than 0.1% for experiments using the copper sample holder. Since the thermocouple for temperature measurements of splats and D360 samples cannot be fixed on the samples, the temperature difference between sample and sample holder is expected to be approximately 10%.

The diffraction data of in-situ XRD measurements were analyzed as follows: Recorded Debye-Scherrer ring parts were tangentially integrated in order to achieve XRD intensity profiles. Diffuse scattering by the beryllium dome and decreasing intensity of the incident beam were regarded and corrected, if it was necessary. Bragg reflections were calibrated using corundum standard powder. Bragg peaks were identified by means of search and match method using PDF-2-data of the International Center for Diffraction Data. The in-situ X-ray intensity attenuation was used to estimate the relative density change upon heating  $\Delta\rho/\rho_0$  and the thermal expansion coefficient  $\alpha$ . Assuming that small density changes due to thermally induced volume changes are linear and isotropic, the relative

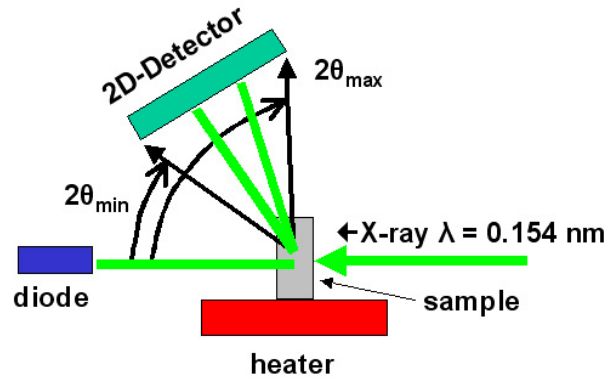


Figure 3.5: Principle of the simultaneous in-situ X-ray diffraction and X-ray attenuation experiment.

density is proportional to the relative volume change  $\Delta\rho/\rho \propto \Delta V/V$  at constant mass. Small changes in the volume of isotropic material is the sum of the lateral expansion in three dimensions  $\Delta V = (\Delta x/x) + (\Delta y/y) + (\Delta z/z)$  and  $(\Delta x/x) = (\Delta y/y) = (\Delta z/z)$ . According to the experimental set-up, the lateral expansion parallel to the beam  $\Delta x/x$  will not influence the attenuation of the X-rays. Only the volume expansion perpendicular to the beam  $((\Delta y/y) + (\Delta z/z))$  will influence attenuation. Thus, the attenuation corresponds to 2/3 of the density. Regarding this, the relative density change upon annealing  $\Delta\rho/\rho$  can be estimated by:

$$-\frac{\Delta\rho}{\rho_0} = \frac{3}{2} \frac{\Delta I}{I_0} \quad (3.4)$$

where  $\Delta I/I_0$  denotes the relative X-ray intensity change (attenuation). The factor 3/2 expresses the correction for the three dimensional volume expansion. The one-dimensional thermal expansion coefficient  $\alpha$  is assumed to be constant when changes are small. Under this condition,  $\alpha$  can be determined by  $\alpha = 1/x \times \Delta x/\Delta T$ , where  $\Delta x$  and  $\Delta T$  are lateral expansion in dimension x and the temperature change, respectively. Assuming furthermore an isotropic material and expansion in three dimensions, the volume expansion coefficient  $\gamma_{th}$  is given by  $\gamma_{th} = 3\alpha$  and  $\Delta\rho/\rho = 3\alpha \times \Delta T$ . Since the experimental set-up regards only changes in two dimensions, the one-dimensional thermal expansion coefficient  $\alpha$  can be estimated by:

$$\alpha = \frac{1}{2} \frac{1}{\Delta T} \frac{\Delta I}{I_0} \quad (3.5)$$

where  $\Delta I/I_0$ ,  $\Delta T$  and the factor 1/2 denote the relative X-ray intensity change (attenuation), the temperature change and correction factor taking into account the three dimensional volume expansion. The overall error of relative density calculation and  $\alpha$  is about 5% and 40%, respectively.

## **Chapter 4**

# **Experimental Results: Powders and Splats**

This chapter deals with the characterization of argon- and helium-atomized  $\text{Al}_{87}\text{Ni}_8\text{La}_5$  and  $\text{Al}_{85}\text{Ni}_{10}\text{La}_5$  (at-%) powder. Morphology, microstructure and thermodynamic behavior are presented and compared. Detailed investigations were made on two batches of helium-atomized  $\text{Al}_{85}\text{Ni}_{10}\text{La}_5$  powders. Moreover, simultaneous X-ray attenuation and X-ray diffraction experiments upon  $\text{Al}_{85}\text{Ni}_{10}\text{La}_5$  splats are herein presented providing information about mass density changes and thermal expansion during annealing.

## 4.1 He-atomized $\text{Al}_{85}\text{Ni}_{10}\text{La}_5$ Powder, Batch I

### 4.1.1 Particle Size Distribution and Morphology

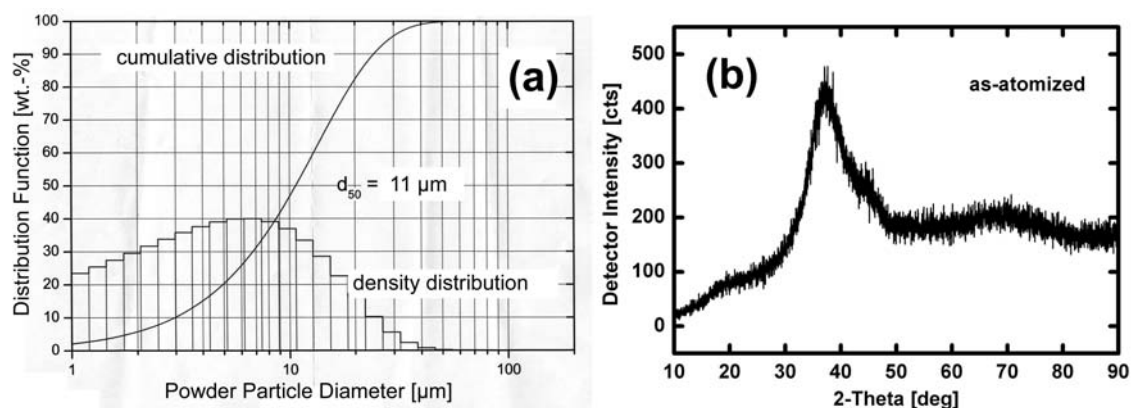


Figure 4.1: (a) Powder particle size distribution, and (b) XRD-patterns of helium-atomized  $\text{Al}_{85}\text{Ni}_{10}\text{La}_5$  powder (batch I).

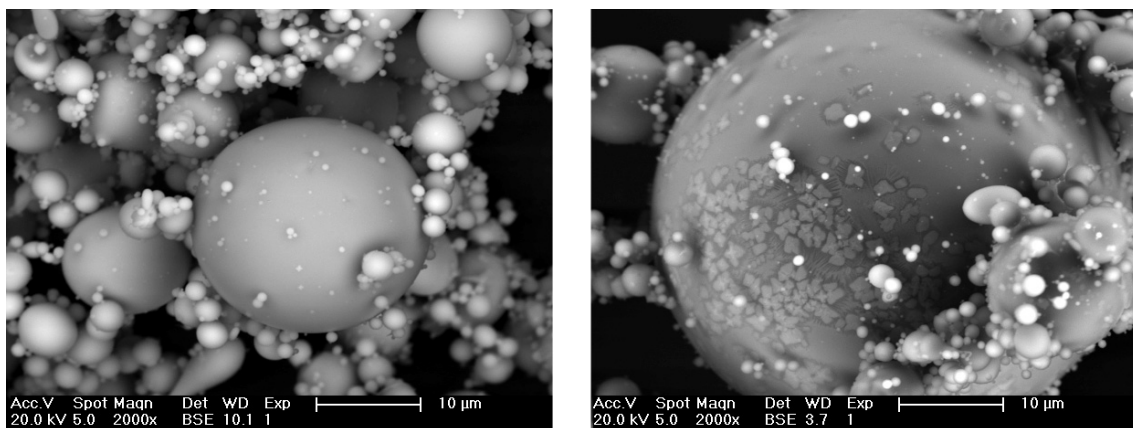


Figure 4.2: SEM-images of helium-atomized  $\text{Al}_{85}\text{Ni}_{10}\text{La}_5$  powder particles (batch I). The left image shows particles smaller than  $11 \mu\text{m}$  diameter. The right image shows one powder particle of about  $30 \mu\text{m}$  diameter.

Figure 4.1(a) shows density and cumulative distribution of powder particle sizes of helium-atomized  $\text{Al}_{85}\text{Ni}_{10}\text{La}_5$  powder (batch I). The most frequent powder particle diam-

eter is  $6\ \mu\text{m}$ . 50 wt.-% and 84 wt.-% of the powder, expressed by the  $d_{50}$  and  $d_{84}$  value, have particle diameters of  $11\ \mu\text{m}$  and  $22\ \mu\text{m}$ , respectively. The geometrical standard deviation  $\sigma_g$  of the density distribution is 2 ( $d_{84}/d_{50}$  ratio). SEM investigations as shown in figure 4.2 reveal, that powder particles have a spherical shape and a smooth surface. Hot welded particle satellites were rarely detected. The right SEM-image in figure 4.2 depicts a powder particle with a diameter of about  $30\ \mu\text{m}$ . Single dendrites with a size of approximately 1 to  $2\ \mu\text{m}$  occur on its surface.

#### 4.1.2 Microstructure of As-atomized Powder

Figure 4.1(b) shows XRD patterns of helium-atomized  $\text{Al}_{85}\text{Ni}_{10}\text{La}_5$  powder (batch I). A broad diffuse scattering maximum intensity - the amorphous halo - occurs at a  $2\Theta \approx 37^\circ$ . It is accompanied by a shoulder at  $2\Theta \approx 44^\circ$ . The broad diffuse scattering maximum and its shoulder are close to the positions of (111) and (200) fcc-Al Bragg reflections of crystalline Al, which occur at  $2\Theta = 38.5^\circ$  and  $2\Theta = 44.7^\circ$ , respectively. Besides, a prepeak occurs at  $2\Theta \approx 20^\circ$ .

#### 4.1.3 Crystallization during Continuous Heating

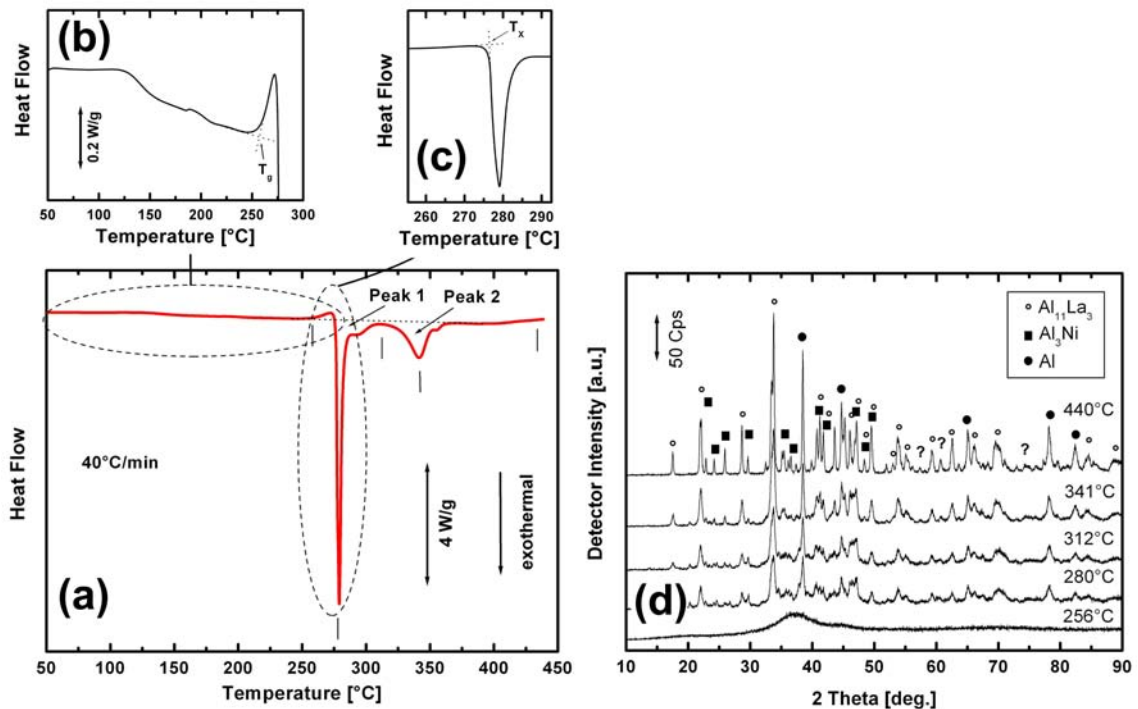


Figure 4.3: (a) DSC curve of helium-atomized  $\text{Al}_{85}\text{Ni}_{10}\text{La}_5$  powder (batch I) obtained during continuous heating at  $40^\circ\text{C}/\text{min}$ . Figures (b) and (c) show enlarged areas of (a). Vertical lines in (a) specify the temperatures at which the microstructure was investigated by means of XRD after continuous heating up to the indicated temperature. The corresponding XRD patterns are presented in (d).

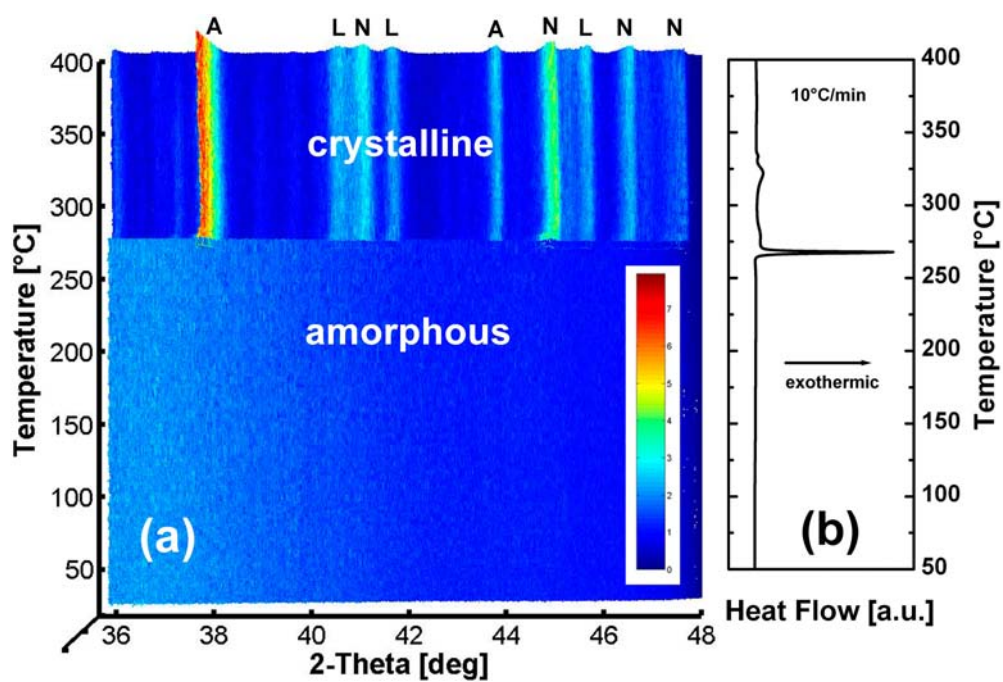


Figure 4.4: (a) In-situ XRD plot of helium-atomized  $Al_{85}Ni_{10}La_5$  powder (batch I) obtained during continuous heating at  $10^\circ C/min$ . The intensity is expressed by different colors. Capital letter A, N and L signify Bragg reflections of fcc-Al,  $Al_3Ni$  and  $Al_{11}La_3$  phase, respectively. Figure (b) shows a DSC curve corresponding to (a), which was measured under identical conditions.

Figure 4.3(a) presents the DSC curve of helium-atomized Al<sub>85</sub>Ni<sub>10</sub>La<sub>5</sub> powder (batch I) obtained during continuous heating at 40°C/min. As highlighted in figure 4.3(b), a small broad exothermic heat release ranging from approximately 125°C to 250°C can be observed denoting structural relaxation. A glass transition occurs at an onset temperature of  $T_g = 258^\circ\text{C}$ , as indicated by the endothermic peak in figure 4.3(c). The first large exothermic heat release can be detected at an onset temperature of  $T_X = 277^\circ\text{C}$  indicating the begin of the crystallization. Two exothermic peaks can be distinguished. They show curve minimum temperatures at  $T_{Peak1} = 280^\circ\text{C}$  and  $T_{Peak2} = 341^\circ\text{C}$ , respectively.

Figure 4.3(b) shows XRD patterns of helium-atomized Al<sub>85</sub>Ni<sub>10</sub>La<sub>5</sub> powder (batch I) obtained after continuous heating at 40°C/min up to 256°C, 280°C, 312°C, 341°C and 440°C. These temperatures are marked by small vertical lines in figure 4.3(a). After continuous heating up to 256°C the XRD pattern show a broad diffuse scattering maximum similar to that of the initial as-atomized state. Bragg reflections of fcc-Al and of intermetallic phases (Al<sub>3</sub>Ni and Al<sub>11</sub>La<sub>3</sub>) develop after continuous heating up to 280°C. The Bragg peak intensities of these three phases increase during further continuous heating up to 312°C, 341°C and 440°C.

Figure 4.4(a) shows in-situ XRD patterns of helium-atomized Al<sub>85</sub>Ni<sub>10</sub>La<sub>5</sub> powder (batch I) obtained during continuous heating at 10°C/min. The intensity is expressed by different colors. A color gradient, which occurs in a  $2-\Theta$ -range between 36 and 40°, represents a broad diffuse scattering maximum. It remains essentially unchanged during heating from room temperature to 271°C. At 271°C, Bragg reflections of fcc-Al, Al<sub>3</sub>Ni and Al<sub>11</sub>La<sub>3</sub> develop within a small temperature range of 3 K. All Bragg peaks shift to smaller  $2\Theta$ -values between 271°C and 400°C, indicating thermal expansion of the crystal lattice. Their peak intensities and peak widths change only slightly towards higher intensities and smaller widths.

Figure 4.4(b) shows a DSC continuous heating curve obtained under identical conditions as in figure 4.4(a). The first large exothermic heat release occurs at an onset temperature of 267°C.

#### 4.1.4 Crystallization during Isothermal Heating

Figure 4.5(a) shows the DSC heat response of helium-atomized Al<sub>85</sub>Ni<sub>10</sub>La<sub>5</sub> powder (batch I) during isothermal annealing at 246°C. A first exothermic heat release, which decreases monotonically, can be observed after reaching the dwelling temperature. A second exothermic heat release appears after approximately 10 min, which is indicated by increasing negative heat flow. The curve minimum after approximately 20 min assigns the maximum exothermic heat release of the second peak.

Figure 4.5(b) shows XRD patterns of helium-atomized Al<sub>85</sub>Ni<sub>10</sub>La<sub>5</sub> alloy powder (batch I) obtained after isothermal annealing at 246°C for 5 min, 10 min, 15 min, 20 min and 30 min. The times correspond to small vertical lines in figure 4.5(a). After 5 min of isothermal annealing, XRD patterns resemble the ones of the initial as-atomized state. First signs of fcc-Al Bragg reflections with marginal intensities rise from the broad diffuse scattering level after 15 min. After 20 min of isothermal annealing, Bragg reflections of

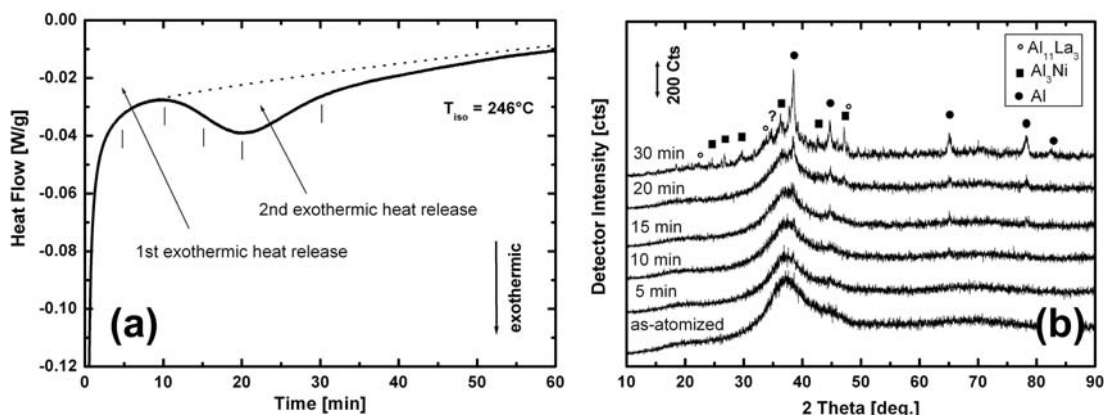


Figure 4.5: (a) DSC curve of helium-atomized  $\text{Al}_{85}\text{Ni}_{10}\text{La}_5$  powder (batch I) obtained during isothermal heating at  $246^\circ\text{C}$ . Figure (b) shows ex-situ XRD patterns of isothermally annealed powder samples. Annealing times are indicated by small vertical lines in (a).

intermetallic phases  $\text{Al}_3\text{Ni}$  and  $\text{Al}_{11}\text{La}_3$  appear. The Bragg peak intensities increase with annealing time.

#### 4.1.5 Calorimetric Characterization of Crystallization

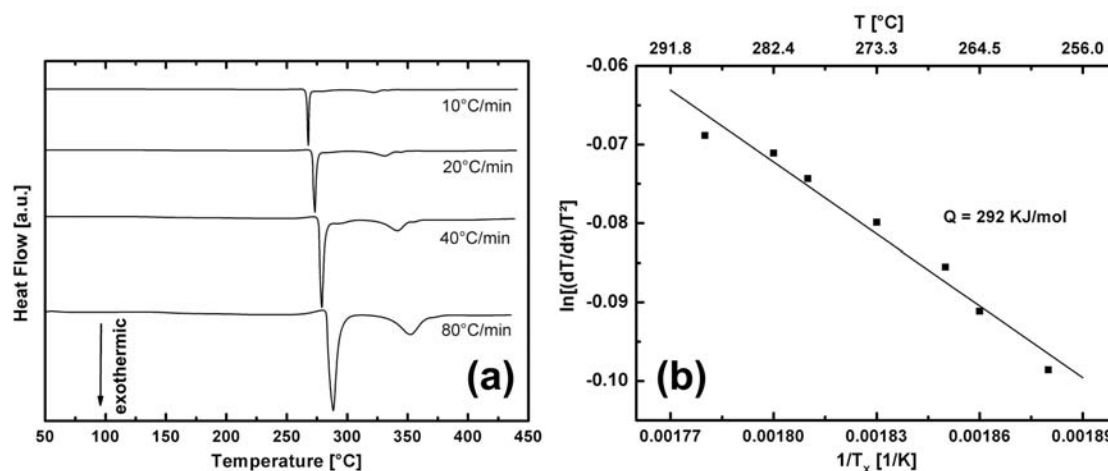


Figure 4.6: (a) DSC curves of helium-atomized  $\text{Al}_{85}\text{Ni}_{10}\text{La}_5$  powder (batch I) obtained during continuous heating using different heating rates. (b) Kissinger plot of the first large exothermic heat release in (a).

Figure 4.6(a) shows DSC continuous heating traces of helium-atomized  $\text{Al}_{85}\text{Ni}_{10}\text{La}_5$  powder (batch I) using heating rates ranging from  $10^\circ\text{C}/\text{min}$  to  $80^\circ\text{C}/\text{min}$ . Two large exothermic peaks occur over all applied heating rates. Their onsets shift to smaller values with increasing heating rate. Figure 4.6(b) shows a Kissinger plot obtained from the first exothermic heat release (crystallization start). The values were extracted from continuous heating experiments using heating rates ranging from  $2.5^\circ\text{C}/\text{min}$  to  $80^\circ\text{C}/\text{min}$ . A fit to

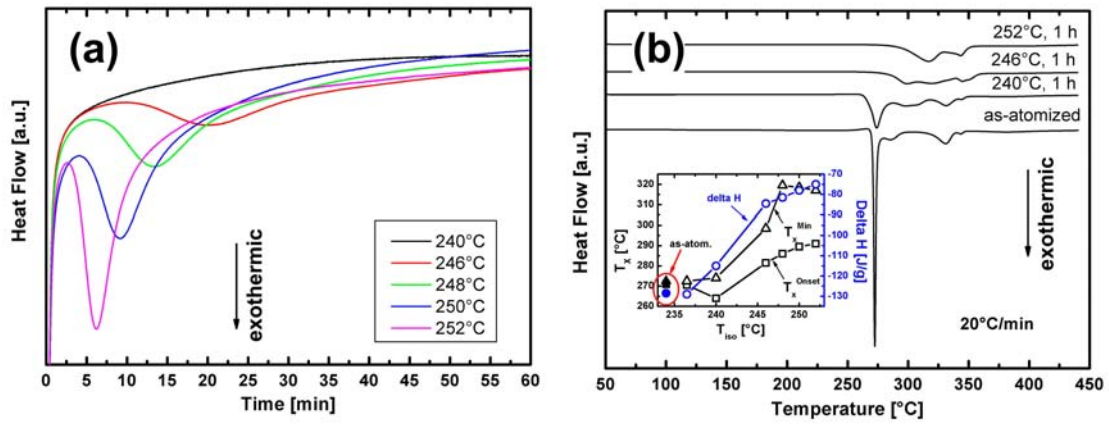


Figure 4.7: (a) DSC curves of helium-atomized  $\text{Al}_{85}\text{Ni}_{10}\text{La}_5$  powder (batch I) obtained during isothermal annealing at different temperatures. (b) DSC continuous heating curves of helium-atomized  $\text{Al}_{85}\text{Ni}_{10}\text{La}_5$  powder (batch I) after 1 hour isothermal annealing at different dwelling temperatures. The inserted plot shows the change of onset temperatures  $T_X^{\text{Onset}}$  and minimum temperatures  $T_X^{\text{Min}}$  of the first large exothermic heat release as a function of  $T_{\text{iso}}$ . The integrated peak area over the whole crystallization sequence is the reaction enthalpy  $\Delta H$ .

data of figure 4.6(b) using a linear function yields an activation energy  $Q = 292$  KJ/mol.

Figure 4.7(a) presents DSC curves of helium-atomized  $\text{Al}_{85}\text{Ni}_{10}\text{La}_5$  powder (batch I) obtained during isothermal annealing at dwelling temperatures ranging from 240 to 252°C. The curve minimum, indicating the maximum exothermic heat release, shifts towards smaller times with increasing dwelling temperatures. The onset time of this event decreases from approximately 10 min at 246°C to 3 min at 252°C. No DSC curve minimum develops during isothermal annealing at 240°C.

Figure 4.7(b) shows DSC continuous heating curves of helium-atomized  $\text{Al}_{85}\text{Ni}_{10}\text{La}_5$  powder (batch I) after 1 hour of isothermal annealing between 240 and 252°C. Onset temperatures  $T_X^{\text{Onset}}$  and minimum temperatures  $T_X^{\text{Min}}$  of the large exothermal heat release (begin of crystallization) at different annealing temperatures are shown in the inserted plot in figure 4.7(b). The integrated peak area over the whole crystallization sequence is the reaction enthalpy  $\Delta H$ . An increasing  $T_{\text{iso}}$  leads to the disappearance of the first crystallization peak and to a decrease of  $\Delta H$ . This is accompanied by a shift of the crystallization start to higher temperatures.

## 4.2 He-atomized $\text{Al}_{85}\text{Ni}_{10}\text{La}_5$ Powder, Batch II

### 4.2.1 Particle Size Distribution and Morphology

Granulometry shows a most frequent powder particle diameter of 7  $\mu\text{m}$  (not presented here). 50 wt.-% and 84 wt.-% of the powder, expressed by the  $d_{50}$  and  $d_{84}$  value, have particle diameters of 12  $\mu\text{m}$  and 24  $\mu\text{m}$ , respectively. The geometrical standard deviation

$\sigma_g$  of the density distribution is 2. SEM investigations (not presented here) reveal that powder particles have a spherical shape and a smooth surface. Hot welded particle satellites were rarely detected. Dendrites with a diameter of approximately 1 to 2  $\mu\text{m}$  can be observed on few single powder particles bigger than 20  $\mu\text{m}$ .

## 4.2.2 Crystallization during Continuous Heating

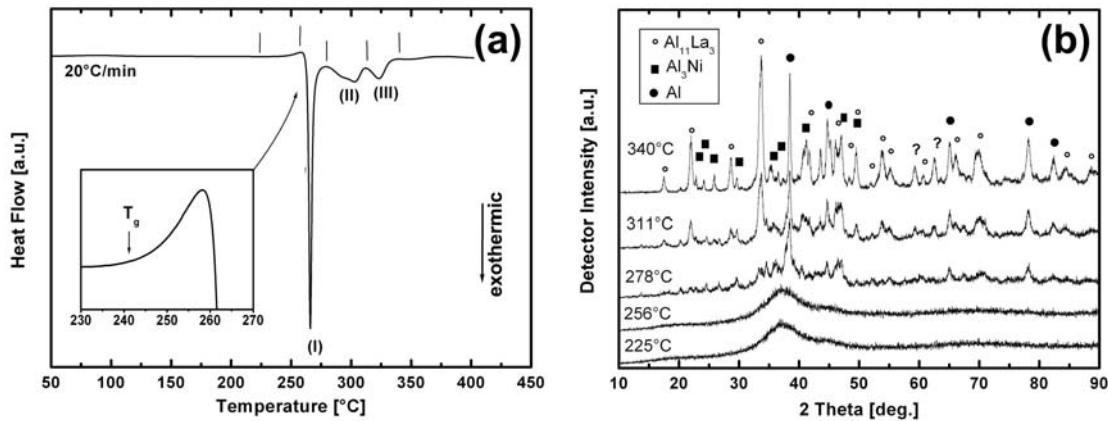


Figure 4.8: (a) DSC curve of helium-atomized  $\text{Al}_{85}\text{Ni}_{10}\text{La}_5$  powder (batch II) obtained during continuous heating at  $20^\circ\text{C}/\text{min}$ . The inserted plot in (a) is an enlarged area of the DSC curve showing the glass transition. Three exothermic peaks can be distinguished. Vertical lines denote temperatures at which the microstructure was investigated by means of XRD. Corresponding XRD patterns are presented (b).

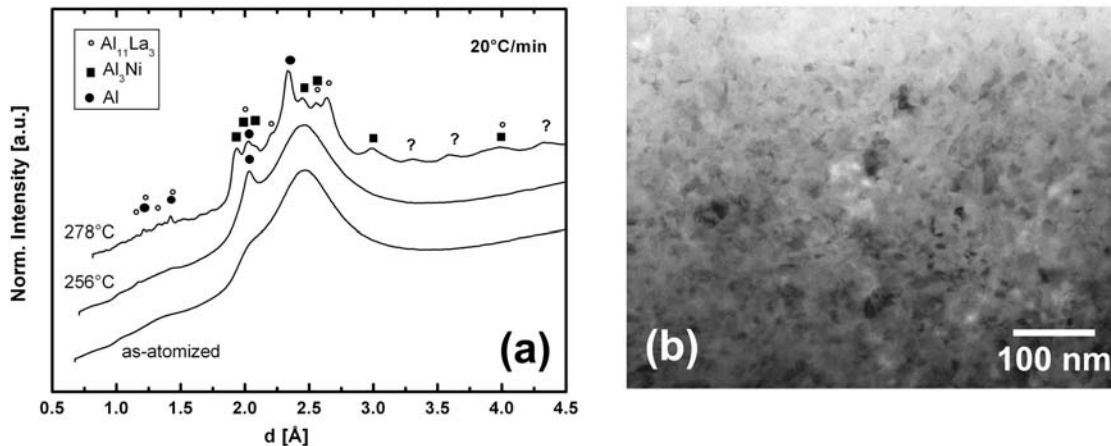


Figure 4.9: (a) Electron diffraction patterns of helium-atomized  $\text{Al}_{85}\text{Ni}_{10}\text{La}_5$  powder (batch II) obtained after continuous heating at  $20^\circ\text{C}/\text{min}$  up to different temperatures. (b) BF-image of  $\text{Al}_{85}\text{Ni}_{10}\text{La}_5$  powder (batch II) obtained after continuous heating at  $20^\circ\text{C}/\text{min}$  up to  $340^\circ\text{C}$ .

Figure 4.8(a) presents the DSC curve of helium-atomized  $\text{Al}_{85}\text{Ni}_{10}\text{La}_5$  powder (batch II) obtained during continuous heating at  $20^\circ\text{C}/\text{min}$ . A glass transition appears at an onset temperature of  $243^\circ\text{C}$ . The first large exothermic heat release at an onset temperature

of  $264^\circ\text{C}$  reflects the start of the crystallization. Three exothermic peaks can be distinguished, which have their minimum temperature at (I)  $266^\circ\text{C}$ , (II)  $303^\circ\text{C}$  and (III)  $323^\circ\text{C}$ .

Figure 4.8(b) shows XRD patterns of helium-atomized  $\text{Al}_{85}\text{Ni}_{10}\text{La}_5$  powder (batch II) obtained after continuous heating at  $20^\circ\text{C}/\text{min}$  up to  $225^\circ\text{C}$ ,  $256^\circ\text{C}$ ,  $278^\circ\text{C}$ ,  $311^\circ\text{C}$  and  $340^\circ\text{C}$ . The temperatures are assigned by small vertical lines in figure 4.8(a). After continuous heating up to  $256^\circ\text{C}$ , the XRD pattern remain essentially unchanged compared to the initial state. Bragg reflections of fcc-Al,  $\text{Al}_3\text{Ni}$  and  $\text{Al}_{11}\text{La}_3$  develop after continuous heating up to  $278^\circ\text{C}$ . After further heating, their peak intensities increase relatively to the background level.

Figure 4.9(a) represents electron diffraction patterns of helium-atomized  $\text{Al}_{85}\text{Ni}_{10}\text{La}_5$  powder (batch II) obtained after continuous heating at  $20^\circ\text{C}/\text{min}$  up to  $256^\circ\text{C}$  and  $278^\circ\text{C}$ . The as-atomized powder shows a broad maximum intensity at  $d \approx 2.5 \text{ \AA}$  accompanied by a shoulder at  $d \approx 2.1 \text{ \AA}$ . In comparison to the as-atomized pattern, after continuous heating up to  $256^\circ\text{C}$  the electron diffraction patterns shows a broad diffuse scattering maximum and a (200) fcc-Al Bragg reflection. Bragg reflections of fcc-Al,  $\text{Al}_3\text{Ni}$  and  $\text{Al}_{11}\text{La}_3$  appear after continuous heating up to  $278^\circ\text{C}$ .

Figure 4.9(b) shows the BF-image of  $\text{Al}_{85}\text{Ni}_{10}\text{La}_5$  alloy powder (batch II) obtained after continuous heating at  $20^\circ\text{C}/\text{min}$  up to  $340^\circ\text{C}$ . The image reveals a fully crystalline microstructure. The median crystal size is 20 nm. First and third quartile size are 12 and 28 nm, respectively.

### 4.2.3 Crystallization during Isothermal Heating

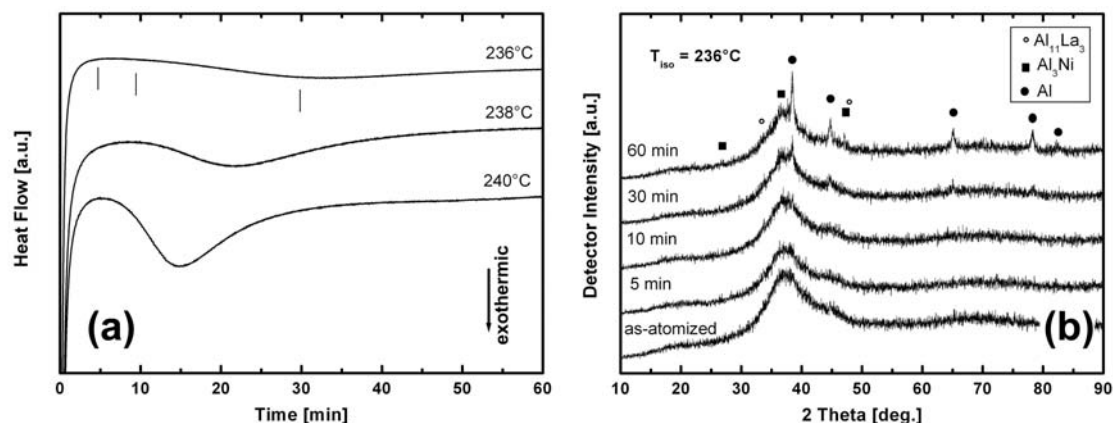


Figure 4.10: (a) DSC curve of helium-atomized  $\text{Al}_{85}\text{Ni}_{10}\text{La}_5$  powder (batch II) obtained during isothermal annealing at different temperatures. Vertical lines in (a) signify the annealing time at  $236^\circ\text{C}$  at which powder samples were investigated by means of XRD, as presented in (b).

Figure 4.10(a) shows DSC curves during isothermal annealing at  $T_{\text{iso}} = 236^\circ\text{C}$  of helium-atomized  $\text{Al}_{85}\text{Ni}_{10}\text{La}_5$  powder (batch II). At  $236^\circ\text{C}$ , a first exothermic heat release develops just after reaching the dwelling temperature. The signal decreases monotonically towards the baseline within 5 min. A second exothermic heat release appears

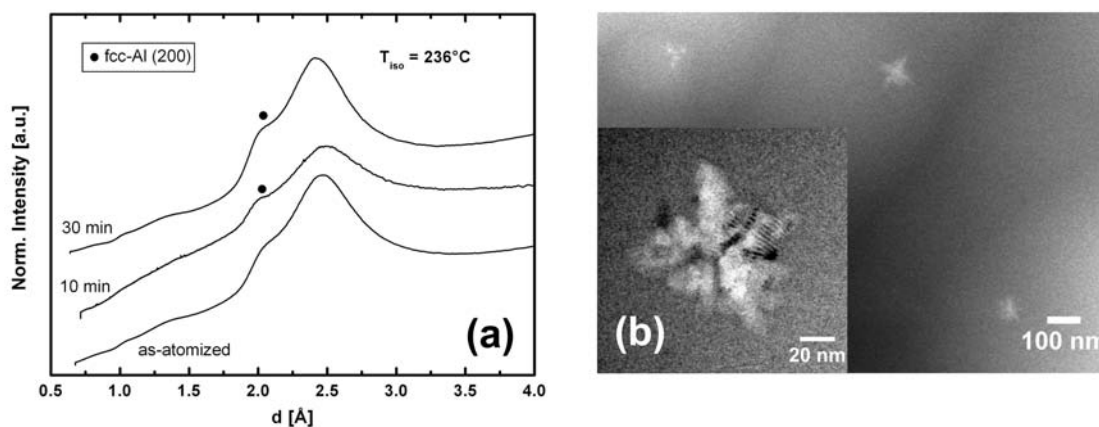


Figure 4.11: (a) Electron diffraction patterns of helium-atomized  $\text{Al}_{85}\text{Ni}_{10}\text{La}_5$  powder (batch II) obtained after 10 min and 30 min of isothermal annealing at  $236^\circ\text{C}$ . (b) BF-image of a helium-atomized  $\text{Al}_{85}\text{Ni}_{10}\text{La}_5$  powder particle (batch II) after 30 min of isothermal annealing at  $236^\circ\text{C}$ . The inserted image shows an enlarged area of (b).

after approximately 9 min showing its maximum heat flow (curve minimum) at approximately 32 min. Applying different dwelling temperatures reveals a shift of the curve minimum towards shorter times with increasing temperature, from 32 min at  $236^\circ\text{C}$ , 22 min at  $238^\circ\text{C}$ , to 15 min at  $240^\circ\text{C}$ .

Figure 4.10(b) shows XRD patterns of helium-atomized  $\text{Al}_{85}\text{Ni}_{10}\text{La}_5$  powder (batch II) obtained after isothermal annealing at  $236^\circ\text{C}$  between 5 min and 60 min. The annealing times are indicated by vertical lines in figure 4.10(a). After 5 min and 10 min isothermal annealing, XRD patterns resemble those of the as-atomized state. First signs of fcc-Al Bragg reflections with marginal intensities rise from the broad diffuse scattering maximum after 30 min. Bragg reflections of  $\text{Al}_3\text{Ni}$  and  $\text{Al}_{11}\text{La}_3$  develop after 60 min of isothermal annealing at  $236^\circ\text{C}$ .

Figure 4.11(a) exhibits electron diffraction patterns of helium-atomized  $\text{Al}_{85}\text{Ni}_{10}\text{La}_5$  powder (batch II) obtained after 10 min and 30 min of isothermal annealing at  $236^\circ\text{C}$ . Both show a broad diffuse scattering maximum and a shoulder close to the (200) fcc-Al Bragg reflection, which is similar to XRD patterns of as-atomized powder.

The BF-image of a  $\text{Al}_{85}\text{Ni}_{10}\text{La}_5$  powder particle (batch II) obtained after 30 min of isothermal annealing at  $236^\circ\text{C}$  in figure 4.11(b) shows single dendrites with a diameter of approximately 100 nm in a featureless amorphous matrix.

### 4.3 Ar-atomized $\text{Al}_{85}\text{Ni}_{10}\text{La}_5$ Powder

Recipient and cyclone fractions of argon-atomized  $\text{Al}_{85}\text{Ni}_{10}\text{La}_5$  powder show median particle diameters  $d_{50}$  of 11  $\mu\text{m}$  and 21  $\mu\text{m}$ , respectively. XRD patterns of these powders are depicted in figure 4.12(b). The cyclone fraction with  $d_{50} = 11 \mu\text{m}$  reveals a broad maximum intensity at  $2\Theta \approx 38^\circ$ , which is accompanied by a shoulder at  $2\Theta \approx 44^\circ$ . This

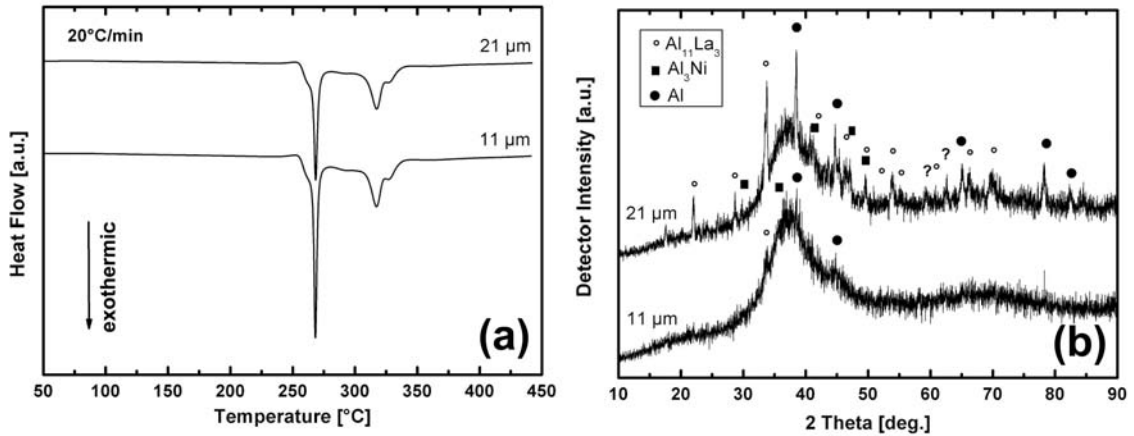


Figure 4.12: (a) DSC continuous heating curves at  $20^\circ\text{C}/\text{min}$ , and (b) XRD patterns of two fractions with different median particle diameters of argon-atomized  $\text{Al}_{85}\text{Ni}_{10}\text{La}_5$  powder.

is similar to XRD patterns of helium-atomized  $\text{Al}_{85}\text{Ni}_{10}\text{La}_5$  powder. The broad scattering maximum is superimposed by small Bragg reflections of fcc-Al,  $\text{Al}_3\text{Ni}$  and  $\text{Al}_{11}\text{La}_3$ . The recipient fraction, which contains coarser powder ( $d_{50} = 21 \mu\text{m}$ ), shows a broad scattering maximum and Bragg reflections of afore mentioned phases. Their intensities relative to the level of the broad scattering maximum are larger compared to those of the cyclone fraction.

Figure 4.12(a) exhibits DSC curves of powders during continuous heating at  $20^\circ\text{C}/\text{min}$ . The powders stem from recipient fraction ( $d_{50} = 21 \mu\text{m}$ ) and cyclone fraction ( $d_{50} = 11 \mu\text{m}$ ). Both curves show a first and a second curve minimum indicating the crystallization reaction. The peak area over both minimum peaks, expressing the reaction enthalpy  $\Delta H$ , decreases with increasing particle size from  $125 \text{ J/g}$  to  $103 \text{ J/g}$ .

## 4.4 He-atomized $\text{Al}_{87}\text{Ni}_8\text{La}_5$ Powder, Batch I

### 4.4.1 Microstructure of As-atomized Powder

Recipient and cyclone fractions of helium-atomized  $\text{Al}_{87}\text{Ni}_8\text{La}_5$  powder have median particle diameters  $d_{50}$  of  $10 \mu\text{m}$  and  $4 \mu\text{m}$ , respectively. Figure 4.13(a) presents XRD patterns of both fractions. Regardless of the particle size, XRD patterns show a broad diffuse scattering maximum and narrow high intensity Bragg reflections of fcc-Al. Figure 4.13(b) illustrates a dendritic morphology of fcc-Al crystals (cyclone fraction,  $d_{50} = 4 \mu\text{m}$ ).

### 4.4.2 Crystallization during Continuous Heating

Figure 4.14(a) presents DSC curves of helium-atomized  $\text{Al}_{87}\text{Ni}_8\text{La}_5$  powder (batch I) obtained during continuous heating at  $20^\circ\text{C}/\text{min}$ . One exothermic heat release occurs at an onset temperature of  $330^\circ\text{C}$ .

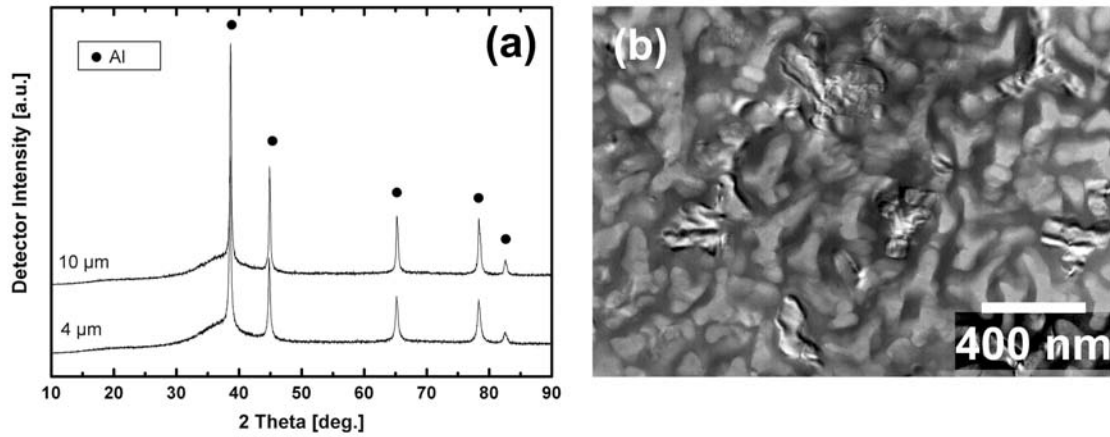


Figure 4.13: (a) XRD patterns of two fractions with different median particle diameters  $d_{50}$  of helium-atomized  $Al_{87}Ni_8La_5$  powder (batch I). (b) BF-image of a powder particle of the  $d_{50} = 4 \mu m$  fraction.

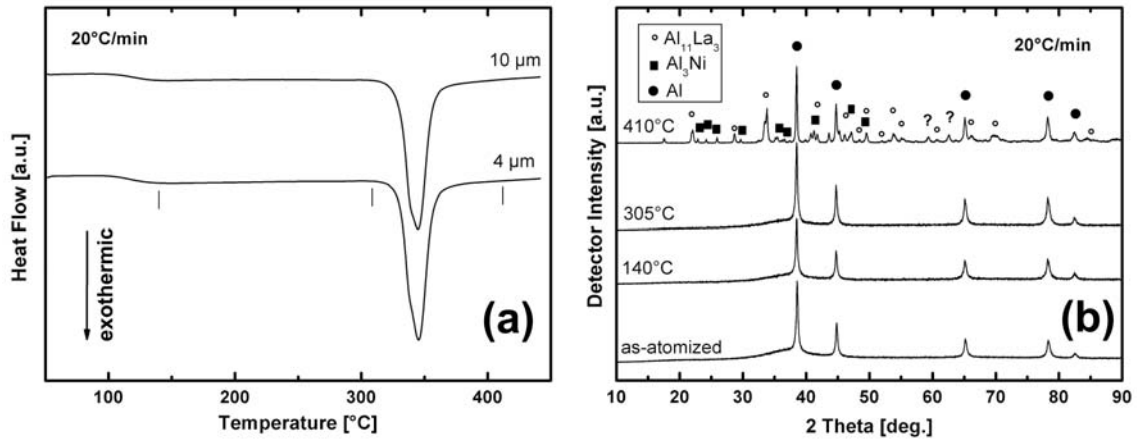


Figure 4.14: (a) DSC curves of two fractions of helium-atomized  $Al_{87}Ni_8La_5$  powder (batch I) obtained during continuous heating at  $20^\circ C/min$ . Vertical lines in (a) indicate the temperature at which annealed powder samples were investigated by means of XRD. The corresponding XRD patterns are presented in (b).

Figure 4.14(b) shows XRD patterns of helium-atomized  $\text{Al}_{87}\text{Ni}_8\text{La}_5$  powders (batch I) obtained after continuous heating at  $20^\circ\text{C}/\text{min}$  up to  $140^\circ\text{C}$ ,  $305^\circ\text{C}$ , and  $410^\circ\text{C}$ . The temperatures are indicated by small vertical lines in figure 4.14(a). The initial microstructure remains essentially unchanged for XRD up to  $305^\circ\text{C}$ . Bragg reflections of  $\text{Al}_3\text{Ni}$  and  $\text{Al}_{11}\text{La}_3$  develop after continuous heating up to  $410^\circ\text{C}$ .

## 4.5 He-atomized $\text{Al}_{87}\text{Ni}_8\text{La}_5$ Powder, Batch II

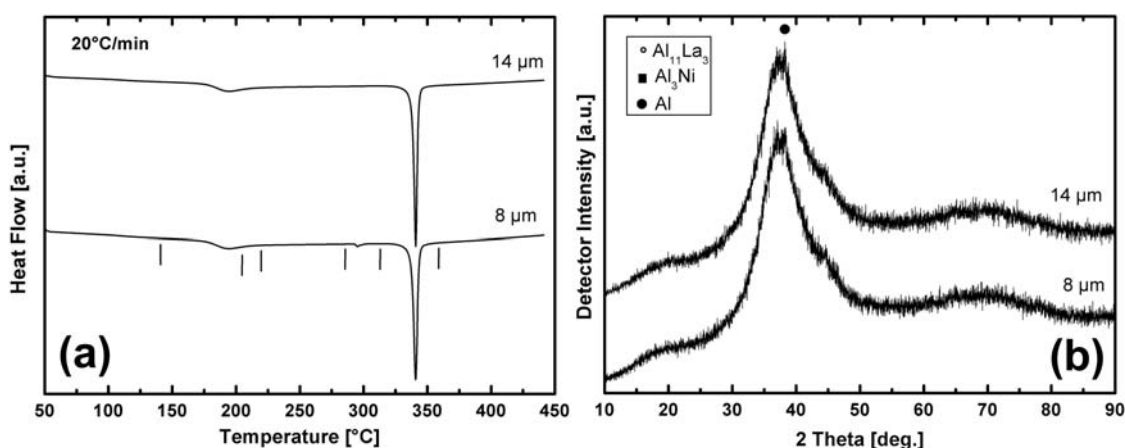


Figure 4.15: (a) DSC curves and (b) XRD patterns of two fractions with different median particle diameters of helium-atomized  $\text{Al}_{87}\text{Ni}_8\text{La}_5$  powder (batch II). DSC curves were obtained during continuous heating at  $20^\circ\text{C}/\text{min}$ . Vertical lines in (a) indicate temperatures, at which annealed powder samples were investigated by means of XRD. Corresponding XRD patterns are presented in figure 4.16.

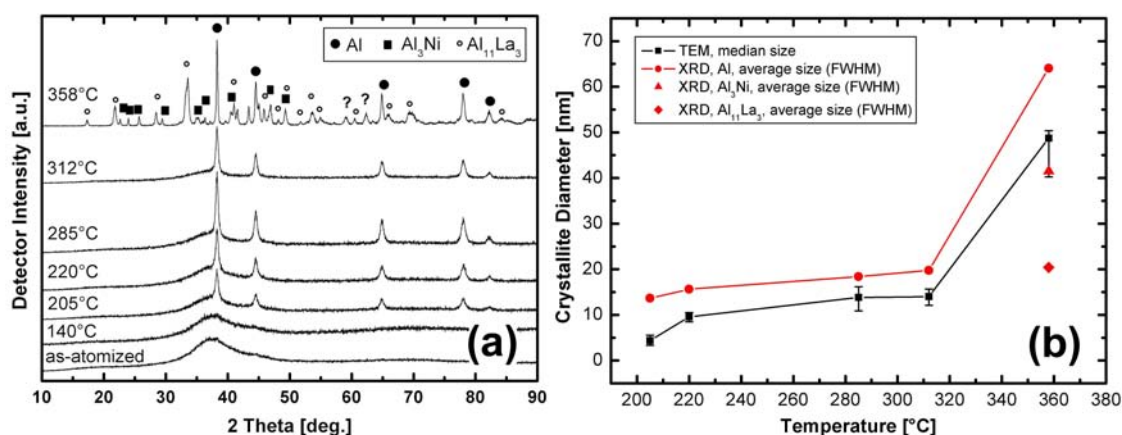


Figure 4.16: (a) XRD patterns and (b) crystallite diameter of helium-atomized  $\text{Al}_{87}\text{Ni}_8\text{La}_5$  powder (batch II,  $d_{50} = 8\ \mu\text{m}$ ) obtained after continuous heating at  $20^\circ\text{C}/\text{min}$  up to temperatures as indicated in figure 4.15(a). Crystallite sizes were calculated from XRD data and from TEM-images.

Recipient and cyclone fractions of helium-atomized  $\text{Al}_{87}\text{Ni}_8\text{La}_5$  powder (batch II) have median particle size diameters  $d_{50}$  of 14  $\mu\text{m}$  and 8  $\mu\text{m}$ , respectively. Figure 4.15(b) shows XRD patterns of both fractions. Regardless of particle size, XRD patterns show a diffuse scattering maximum and small (111) fcc-Al Bragg reflections.

Figure 4.15(a) illustrates DSC curves of powders from recipient and cyclone fractions obtained during continuous heating at  $20^\circ\text{C}/\text{min}$ . Both curves show a first exothermic heat release at an onset temperature of  $176^\circ\text{C}$  indicating a crystallization reaction. At  $337^\circ\text{C}$  onset temperature, both curves show a curve minimum (exothermic heat flow maximum). The 8  $\mu\text{m}$  powder shows a further peak at  $296^\circ\text{C}$ .

Vertical lines in 4.15(a) indicate temperatures, at which annealed powder samples were investigated by means of XRD. Corresponding XRD patterns are presented in figure 4.16(a). After continuous heating up to  $140^\circ\text{C}$ , XRD patterns show a broad diffuse scattering maximum similar to that of the as-atomized powder. XRD patterns of powders annealed up to temperatures ranging from  $205^\circ\text{C}$  to  $312^\circ\text{C}$  exhibit fcc-Al Bragg reflections and a broad scattering maximum. The fcc-Al Bragg reflections increase in intensity and decrease in width with increasing temperature (except the intensity at  $312^\circ\text{C}$ ). At the same time, the broad diffuse scattering intensity decreases. At  $358^\circ\text{C}$ , XRD patterns reveal Bragg reflections of fcc-Al,  $\text{Al}_3\text{Ni}$  and  $\text{Al}_{11}\text{La}_3$ .

Figure 4.16(b) shows crystallites size evolution of helium-atomized  $\text{Al}_{85}\text{Ni}_{10}\text{La}_5$  powder (batch II) after continuous heating at  $20^\circ\text{C}/\text{min}$  up to different temperatures. Crystallite diameters were determined from TEM-images and XDR data. Crystallite sizes of fcc-Al increase slightly between  $205^\circ\text{C}$  and  $312^\circ\text{C}$  from 4 nm to 14 nm for TEM analysis, and from 14 nm to 20 nm for XRD analysis. At  $358^\circ\text{C}$ , fcc-Al crystallite diameters increase to 49 nm for TEM analysis, and to 64 nm for XRD analysis.

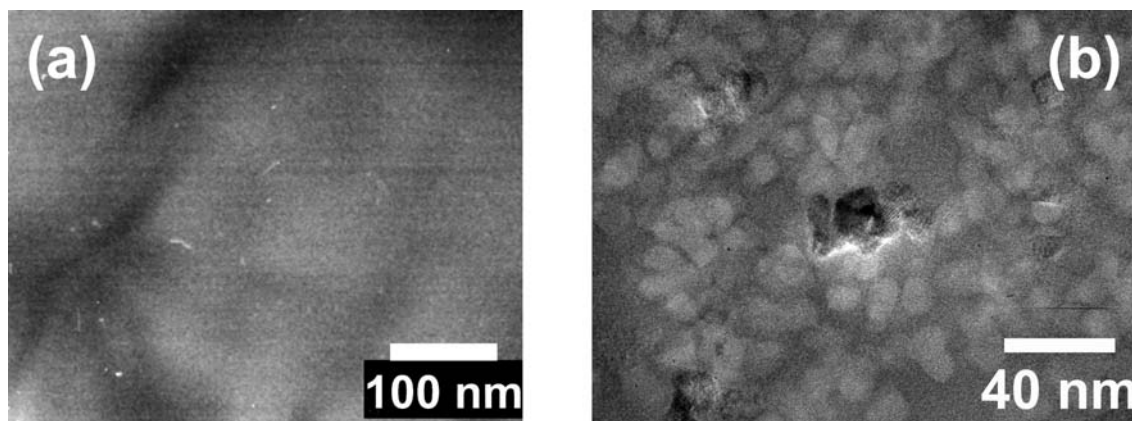


Figure 4.17: (a) BF-image of a helium-atomized  $\text{Al}_{87}\text{Ni}_8\text{La}_5$  powder particles (batch II, 8  $\mu\text{m}$ ) in the initial state, and (b) after continuous heating at  $20^\circ\text{C}/\text{min}$  up to  $312^\circ\text{C}$  (b).

Figure 4.17(a) shows a featureless amorphous structure of helium-atomized  $\text{Al}_{87}\text{Ni}_8\text{La}_5$  powder (batch II, 8  $\mu\text{m}$ ). Figure 4.17(b) shows spheric and dendritic fcc-Al crystallites (light gray contrast) within the amorphous matrix (dark gray contrast) of a helium-atomized  $\text{Al}_{87}\text{Ni}_8\text{La}_5$  powder particle (batch II, 8  $\mu\text{m}$ ) obtained after continuous heating at  $20^\circ\text{C}/\text{min}$  up to  $312^\circ\text{C}$ .

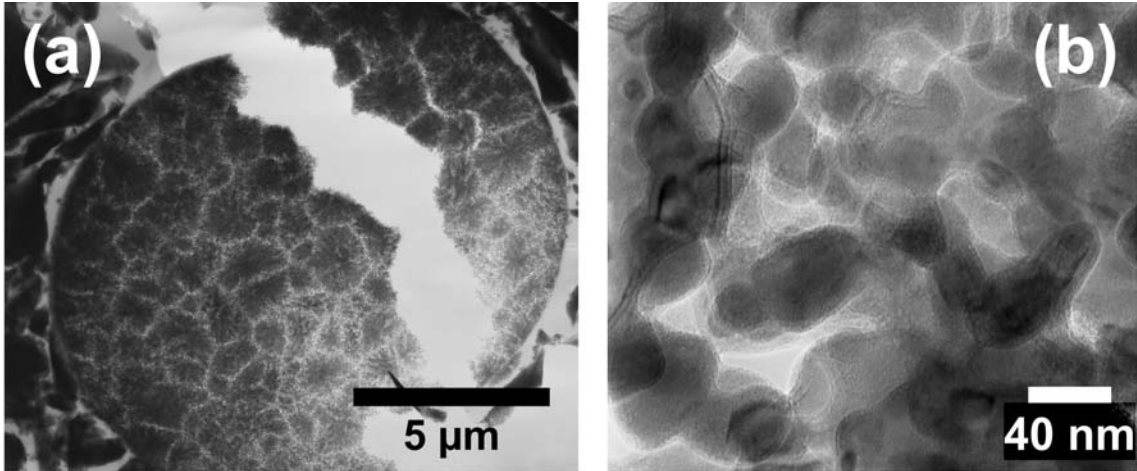


Figure 4.18: *BF*-images of a helium-atomized  $Al_{87}Ni_8La_5$  powder particle (batch II,  $8\ \mu m$ ) obtained after continuous heating at  $20^\circ C/min$  up to  $358^\circ C$ . Image (a) and (b) show different magnifications of the same powder particle.

Figure 4.18 shows a helium-atomized  $Al_{87}Ni_8La_5$  powder particle (batch II,  $8\ \mu m$ ) obtained after continuous heating at  $20^\circ C/min$  up to  $358^\circ C$ . Figure 4.18(a) exhibits the cross section at lower magnifications revealing “coarse” grains with a diameter of approximately  $1\ \mu m$ . At higher magnifications in figure 4.18(b), the previously described grains show subgrains.

## 4.6 Ar-atomized $Al_{87}Ni_8La_5$ Powder

### 4.6.1 Microstructure of As-atomized Powder

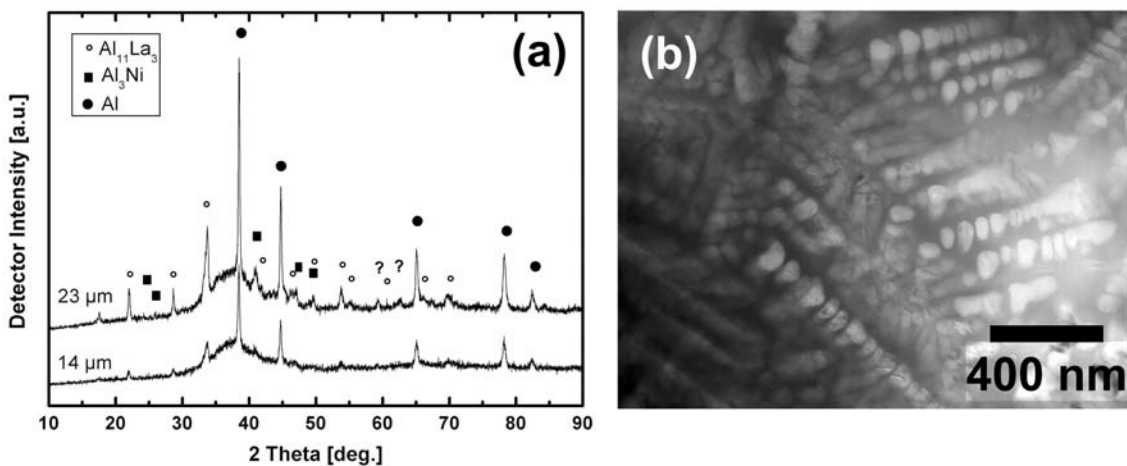


Figure 4.19: (a) XRD patterns of two fractions with different median particle diameters  $d_{50}$  of argon-atomized  $Al_{87}Ni_8La_5$  powder. (b) *BF*-image a powder particle of the  $d_{50} = 14\ \mu m$  fraction.

Recipient and cyclone fractions of argon-atomized  $\text{Al}_{87}\text{Ni}_8\text{La}_5$  powder have median particle diameters  $d_{50}$  of  $23\ \mu\text{m}$  and  $14\ \mu\text{m}$ , respectively. Figure 4.19(a) shows XRD patterns of both fractions, which reveal fcc-Al,  $\text{Al}_3\text{Ni}$  and  $\text{Al}_{11}\text{La}_3$  Bragg reflections, and a broad diffuse scattering maximum. The intensities of Bragg reflections are smaller compared to coarser powder particles.

Figure 4.19(b) illustrates the dendritic crystallite morphology in an argon-atomized  $\text{Al}_{87}\text{Ni}_8\text{La}_5$  powder particle (cyclone fraction,  $d_{50} = 14\ \mu\text{m}$ ).

## 4.6.2 Crystallization during Continuous Heating

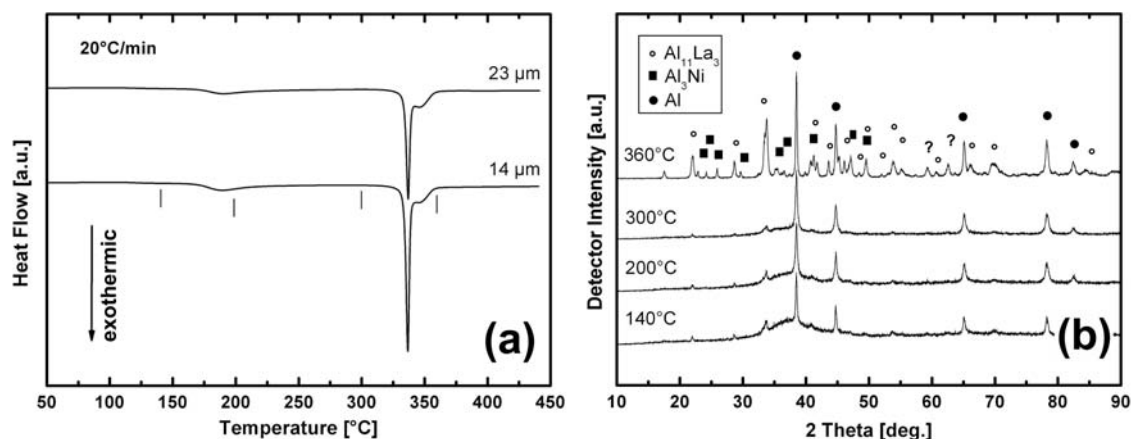


Figure 4.20: (a) DSC curves of two fractions with different median particle diameters of argon-atomized  $\text{Al}_{87}\text{Ni}_8\text{La}_5$  powder obtained during continuous heating at  $20^\circ\text{C}/\text{min}$ . Vertical lines in (a) indicate final temperatures of annealed specimen, at which XRD experiments were performed. Corresponding XRD patterns are presented in (b).

Figure 4.20(a) shows DSC curves of argon-atomized  $\text{Al}_{87}\text{Ni}_8\text{La}_5$  powder obtained during continuous heating at  $20^\circ\text{C}/\text{min}$ . Regardless of the powder particle size of each fraction, both DSC curves exhibit a first small and a second large exothermic heat release at onset temperatures of  $170^\circ\text{C}$  and  $333^\circ\text{C}$ , respectively.

Figure 4.20(b) show XRD patterns of argon-atomized  $\text{Al}_{87}\text{Ni}_8\text{La}_5$  powder obtained after continuous heating at  $20^\circ\text{C}/\text{min}$  up to different temperatures. Annealing temperatures are indicated by small vertical lines in figure 4.20(a). XRD patterns of the specimen annealed up to  $140^\circ\text{C}$  shows a broad diffuse scattering maximum and Bragg reflections of fcc-Al,  $\text{Al}_3\text{Ni}$  and  $\text{Al}_{11}\text{La}_3$ . After further continuous heating up to  $360^\circ\text{C}$ , intermetallic phases  $\text{Al}_3\text{Ni}$  and  $\text{Al}_{11}\text{La}_3$  develop and the broad diffuse scattering disappears.

## 4.7 Comparison of Powders

### 4.7.1 Influence of Alloy Composition, Atomization Gas, and Powder Particle Size on Microstructure and Oxygen Content

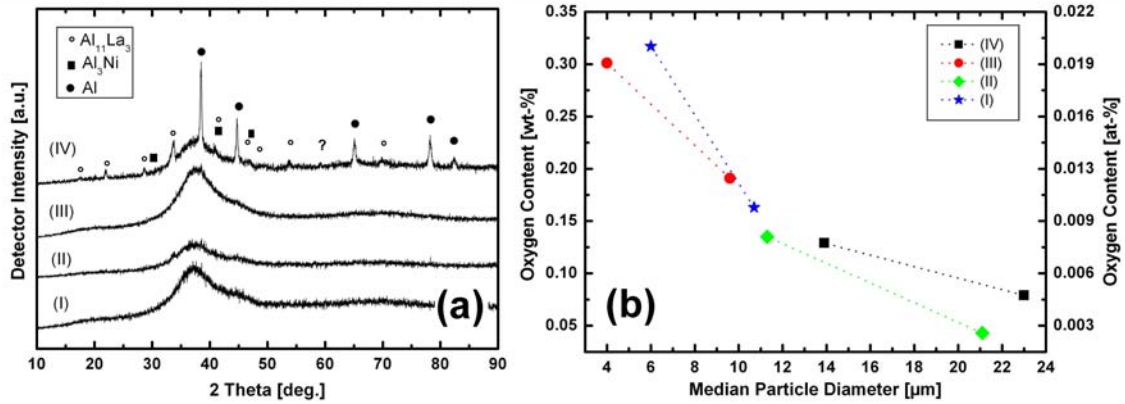


Figure 4.21: (a) XRD patterns and (b) oxygen content of (I) helium- and (II) argon-atomized  $\text{Al}_{85}\text{Ni}_{10}\text{La}_5$  powder with a median powder diameter of 11  $\mu\text{m}$ , and of (III) helium-, and (IV) argon-atomized  $\text{Al}_{87}\text{Ni}_8\text{La}_5$  powder with a median powder diameter of 14  $\mu\text{m}$ .

Figure 4.21(a) shows XRD patterns of helium- and argon-atomized  $\text{Al}_{85}\text{Ni}_{10}\text{La}_5$  and  $\text{Al}_{87}\text{Ni}_8\text{La}_5$  powders. The median particle diameter  $d_{50}$  is 11 and 14  $\mu\text{m}$  for  $\text{Al}_{85}\text{Ni}_{10}\text{La}_5$  and  $\text{Al}_{87}\text{Ni}_8\text{La}_5$  powders, respectively. XRD patterns of (I) helium- and (II) argon-atomized  $\text{Al}_{85}\text{Ni}_{10}\text{La}_5$  powders show a broad scattering maximum accompanied by a shoulder near the (200) fcc-Al Bragg reflection. XRD patterns of argon-atomized powders show additionally low intensity Bragg reflections of fcc-Al,  $\text{Al}_3\text{Ni}$  and  $\text{Al}_{11}\text{La}_3$ , as highlighted in figure 4.12. XRD patterns of (III) helium-atomized  $\text{Al}_{87}\text{Ni}_8\text{La}_5$  powder (batch II) reveal a broad scattering maximum. XRD patterns of (IV) argon-atomized  $\text{Al}_{87}\text{Ni}_8\text{La}_5$  powder show fcc-Al,  $\text{Al}_{11}\text{La}_3$  Bragg reflections, and a broad diffuse scattering maximum.

Figure 4.21(b) presents oxygen contents of argon- and helium-atomized  $\text{Al}_{87}\text{Ni}_8\text{La}_5$  alloy and  $\text{Al}_{85}\text{Ni}_{10}\text{La}_5$  powders obtained by hot gas extraction. The oxygen content decreases with increasing powder particle diameter.

### 4.7.2 Summary of Powder Properties

Tables 4.1 and 4.2 list the results of granulometry, ICP-MS, XRD and DSC experiments on argon- and helium-atomized  $\text{Al}_{87}\text{Ni}_8\text{La}_5$  and  $\text{Al}_{85}\text{Ni}_{10}\text{La}_5$  powders. They yield information about initial powder particle size, chemical composition, initial microstructure as well as temperatures, enthalpies and activation energies of crystallization reactions. Plus and minus symbols indicate whether the item listed in the row exists or not. The abbreviation “n” denotes not determined or not measured. The activation energies were obtained using Kissinger analysis.

atomization gas	Argon		Helium			
batch	I		I		II	
fraction	recipient	cyclone	recipient	cyclone	recipient	cyclone
<b>d<sub>50</sub> [μm]</b>	23	14	10	4	14	8
<b>Al [at-%]</b>	88.8	n	90.7	n	n	88.1
<b>Ni [at-%]</b>	6.7	n	5.5	n	n	7.8
<b>La [at-%]</b>	4.5	n	3.8	n	n	4.1
<b>amorphous</b>	+	+	+	+	+	+
<b>fcc-Al</b>	+	+	+	+	-	-
<b>Al<sub>3</sub>Ni</b>	+	-	-	-	-	-
<b>Al<sub>11</sub>La<sub>3</sub></b>	+	+	-	-	-	-
<b>T<sub>g</sub> (onset) [°C]</b>	-	-	-	-	-	-
<b>T<sub>X1</sub> (onset) [°C]</b>	170	169	-	-	176	176
<b>T<sub>X1</sub> (peak) [°C]</b>	190	190	-	-	194	194
<b>ΔH<sub>1</sub> [kJ/mol]</b>	-0.7	-1.1	-	-	-1.6	-1.5
<b>Q<sub>1</sub> [kJ/mol]</b>	-	164	-	-	-	182
<b>T<sub>X2</sub> (onset) [°C]</b>	333	333	330	333	337	337
<b>T<sub>X2</sub> (peak) [°C]</b>	337	337	345	345	341	341
<b>ΔH<sub>2</sub> [kJ/mol]</b>	-2.1	-2.6	-2.5	-2.6	-3.1	-3.1
<b>Q<sub>2</sub> [kJ/mol]</b>	n	196	216	n	n	196

Table 4.1: Summary of properties of Al<sub>87</sub>Ni<sub>8</sub>La<sub>5</sub> alloy powders.

atomization gas	Argon		Helium				
batch	I		I		II		blend
fraction	rec.	cyc.	rec.	cyc.	rec.	cyc.	cyc.
<b>d<sub>50</sub> [μm]</b>	21	11	11	6	12	6	n
<b>Al [at-%]</b>	n	85.3	85.2	n	85.3	n	n
<b>Ni [at-%]</b>	n	9.5	9.7	n	9.7	n	n
<b>La [at-%]</b>	n	5.1	5.1	n	5.0	n	n
<b>amorphous</b>	+	+	+	+	+	+	+
<b>fcc-Al</b>	+	-	-	-	-	-	-
<b>Al<sub>3</sub>Ni</b>	+	-	-	-	-	-	-
<b>Al<sub>11</sub>La<sub>3</sub></b>	+	+	-	-	-	-	-
<b>T<sub>g</sub> (onset) [°C]</b>	242	242	254	253	243	246	247
<b>T<sub>X</sub> (onset) [°C]</b>	256	256	271	270	264	264	264
<b>T<sub>X</sub> (peak) [°C]</b>	268	268	273	272	266	266	267/272
<b>ΔH [kJ/mol]</b>	-3.7	-4.5	-3.6	-4.4	-5.1	-5.3	-4.4
<b>Q [kJ/mol]</b>	n	339	292	n	267	n	n

Table 4.2: Summary of properties of Al<sub>85</sub>Ni<sub>10</sub>La<sub>5</sub> alloy powders.

## 4.8 Simultaneous In-situ X-ray Attenuation and Diffraction

### 4.8.1 Composition of Al-Ni-La Splats

Assuming that  $\text{Al}_{85}\text{Ni}_{10}\text{La}_5$  splats contain only Al, Ni, and La, ICP-MS analysis provided the following composition:  $\text{Al}_{85.1}\text{Ni}_{9.7}\text{La}_{5.2}$ . An error was calculated being about 0.1 at-%. The composition of the master alloy ingot was  $\text{Al}_{85.2}\text{Ni}_{9.6}\text{La}_{5.1}$ .

### 4.8.2 Continuous Heating

#### One-step Continuous Heating

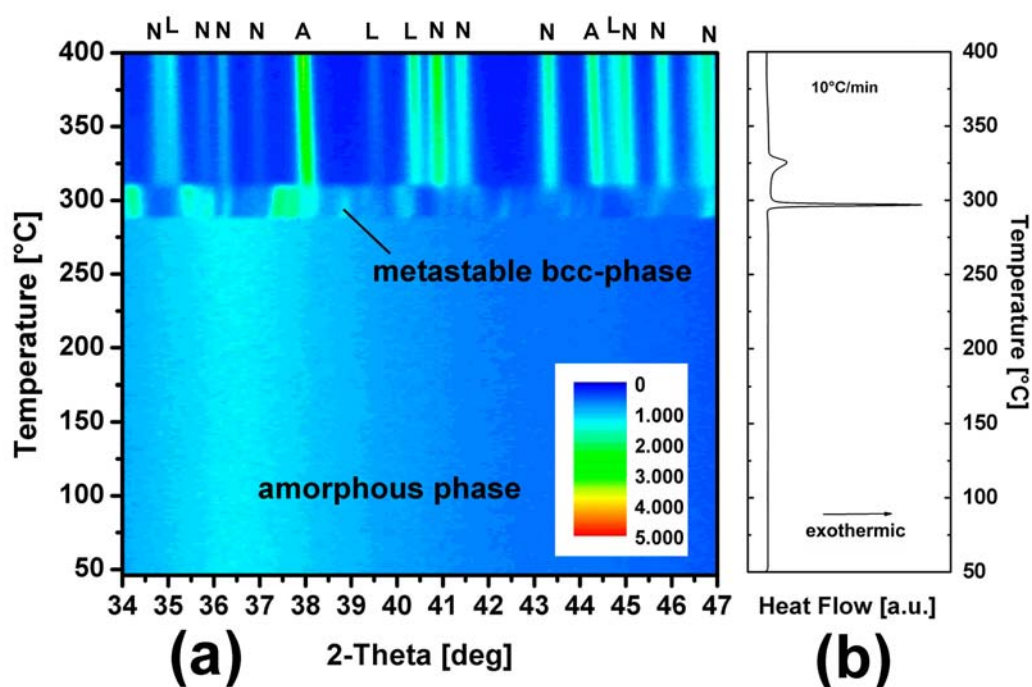


Figure 4.22: (a) In-situ XRD intensity plot of a  $\text{Al}_{85}\text{Ni}_{10}\text{La}_5$  splat obtained during continuous heating at  $10^\circ\text{C}/\text{min}$ . The intensity level corresponds to different colors. Letter A, N, and L denote Bragg reflections of fcc-Al,  $\text{Al}_3\text{Ni}$ ,  $\text{Al}_{11}\text{La}_3$  phase, respectively. (b) DSC curve of a  $\text{Al}_{85}\text{Ni}_{10}\text{La}_5$  splat obtained during continuous heating at  $10^\circ\text{C}/\text{min}$ .

Figure 4.22(a) shows the in-situ XRD plot of a  $\text{Al}_{85}\text{Ni}_{10}\text{La}_5$  splat obtained during continuous heating at  $10^\circ\text{C}/\text{min}$ . Initial XRD patterns exhibit a broad diffuse scattering maximum. The broad diffuse scattering maximum remains essentially unchanged during continuous heating. At  $282^\circ\text{C}$ , fcc-Al and an unknown phase develop in a small temperature range of  $3^\circ\text{C}$ . The unknown phase can be identified as a metastable bcc-phase [68], [69]. This phase was not observed during crystallization of  $\text{Al}_{85}\text{Ni}_{10}\text{La}_5$  powder. At

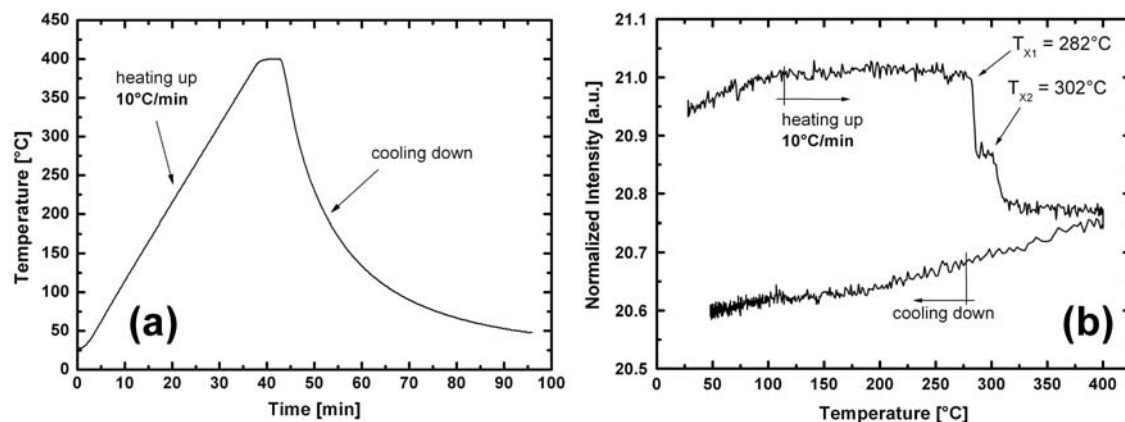


Figure 4.23: (a) *Temperature vs. time curve*, and (b) *in-situ X-ray attenuation of a  $\text{Al}_{85}\text{Ni}_{10}\text{La}_5$  splat obtained during continuous heating at  $10^\circ\text{C}/\text{min}$ .*

$314^\circ\text{C}$ , the Bragg reflections of metastable bcc-phase disappear within a small temperature range and Bragg reflections of  $\text{Al}_3\text{Ni}$  and  $\text{Al}_{11}\text{La}_3$  develop. All Bragg peaks increase in intensity and shift towards smaller  $2\Theta$ -values during further heating between  $314^\circ\text{C}$  and  $400^\circ\text{C}$ .

Figure 4.22(b) represents a DSC curve of a specimen from the same splat, which was used for an in-situ XRD experiment in figure 4.22(a). A small endothermic heat release indicating the glass transition occurs at an onset temperature of  $279^\circ\text{C}$ . Two exothermic peaks develop at  $295^\circ\text{C}$  and  $325^\circ\text{C}$ , respectively.

Figure 4.23(a) shows a heating profile of the simultaneous X-ray attenuation and diffraction experiment. The splat cooled down with monotonically decreasing cooling rate.

Figure 4.23(b) illustrates the in-situ X-ray attenuation plot of a  $\text{Al}_{85}\text{Ni}_{10}\text{La}_5$  splat, which was simultaneously recorded to XRD patterns shown in figure 4.22(a). At  $282^\circ\text{C}$  a two step intensity decrease develops within a small temperature range of 5 and  $12^\circ\text{C}$ , at  $282^\circ\text{C}$  and at  $302^\circ\text{C}$ , respectively. The mass density increases in two steps by about 0.9% and 0.6%, respectively.

### Multi-step Continuous Heating

Figure 4.24(a) shows the heating procedure applied to a  $\text{Al}_{85}\text{Ni}_{10}\text{La}_5$  splat. It demonstrates that the splat was heated up three times.

Figure 4.24(b) shows the in-situ X-ray attenuation of the  $\text{Al}_{85}\text{Ni}_{10}\text{La}_5$  splat during cyclic heating as described in (a). During continuous heating up to  $250^\circ\text{C}$ , the intensity increases with a different slope in step 1 compared to step 3 (not presented in the diagram), which yields thermal expansion coefficients of  $1.2 \times 10^{-5} \text{ 1/K}$  and  $2.3 \times 10^{-5} \text{ 1/K}$ , respectively. Continuous heating in step 5 from  $50^\circ\text{C}$  to  $268^\circ\text{C}$  shows a comparable slope to that of step 3. The thermal expansion coefficient in that temperature range of step 5 is  $2.2 \times 10^{-5} \text{ 1/K}$ .

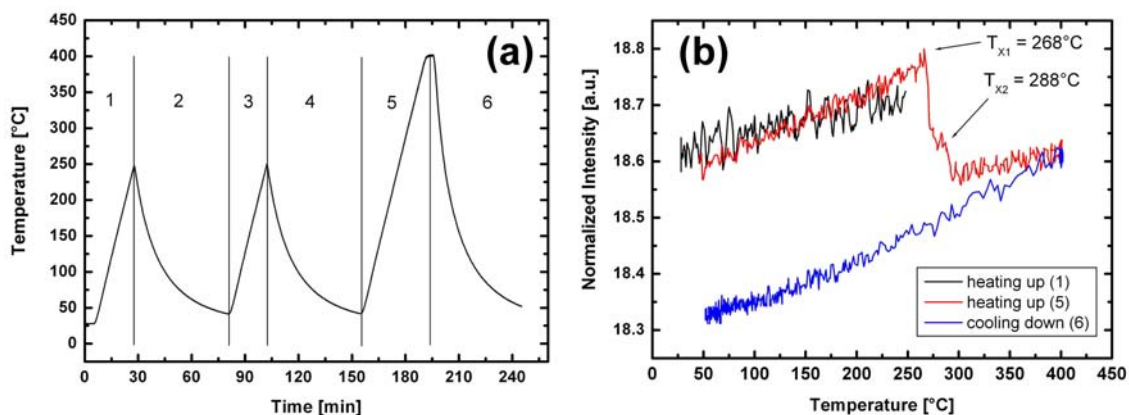


Figure 4.24: (a) Temperature vs. time curve, and (b) in-situ X-ray attenuation of a  $\text{Al}_{85}\text{Ni}_{10}\text{La}_5$  splat obtained during cyclic heating. Step 1 and 3 indicate heating at  $10^\circ\text{C}/\text{min}$  up to  $250^\circ\text{C}$ . Step 5 indicates heating at an identical rate up to  $400^\circ\text{C}$ . Steps 2, 4, and 6 indicate subsequent cooling after heating.

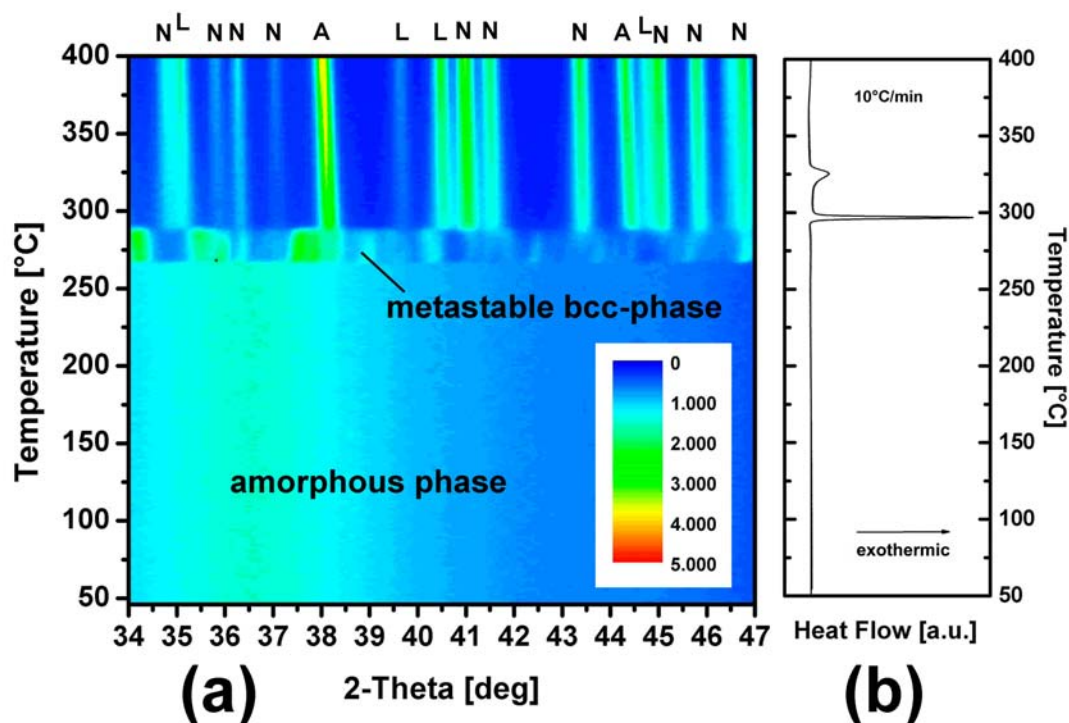


Figure 4.25: Same as figure 4.22 for a  $\text{Al}_{85}\text{Ni}_{10}\text{La}_5$  splat obtained during cyclic heating (step 5).

At 268°C and at 288°C, the intensity decreases within a small temperature range of 2-5°C yielding a mass density change of 1.1% and 0.5%, respectively. During further heating up to 400°C, a thermal expansion coefficient of  $1.1 \times 10^{-5}$  1/K can be determined. Cooling down from 400°C to 300°C and from 150°C to 50°C yields thermal expansion coefficients of  $1.3 \times 10^{-5}$  1/K and  $2.7 \times 10^{-5}$  1/K, respectively.

Figure 4.25(a) shows in-situ XRD patterns of step 5. Initial XRD patterns exhibit a broad diffuse scattering maximum. It remains essentially unchanged during continuous heating. At 262°C, Bragg reflections of fcc-Al and metastable bcc-phase develop within a small temperature range of 2°C. At 286°C, Bragg reflections of the metastable bcc-phase disappear and Bragg reflections of  $\text{Al}_3\text{Ni}$  and  $\text{Al}_{11}\text{La}_3$  develop. The Bragg peaks increase in intensities and shift to smaller  $2\Theta$ -values during further heating up to 400°C.

Figure 4.25(b) represents a DSC curve of the same splat, which was used for the in-situ XRD experiment in figure 4.22(a). Two exothermic heat releases appear at 297°C and 325°C, respectively.

### 4.8.3 Crystallization during isothermal heating

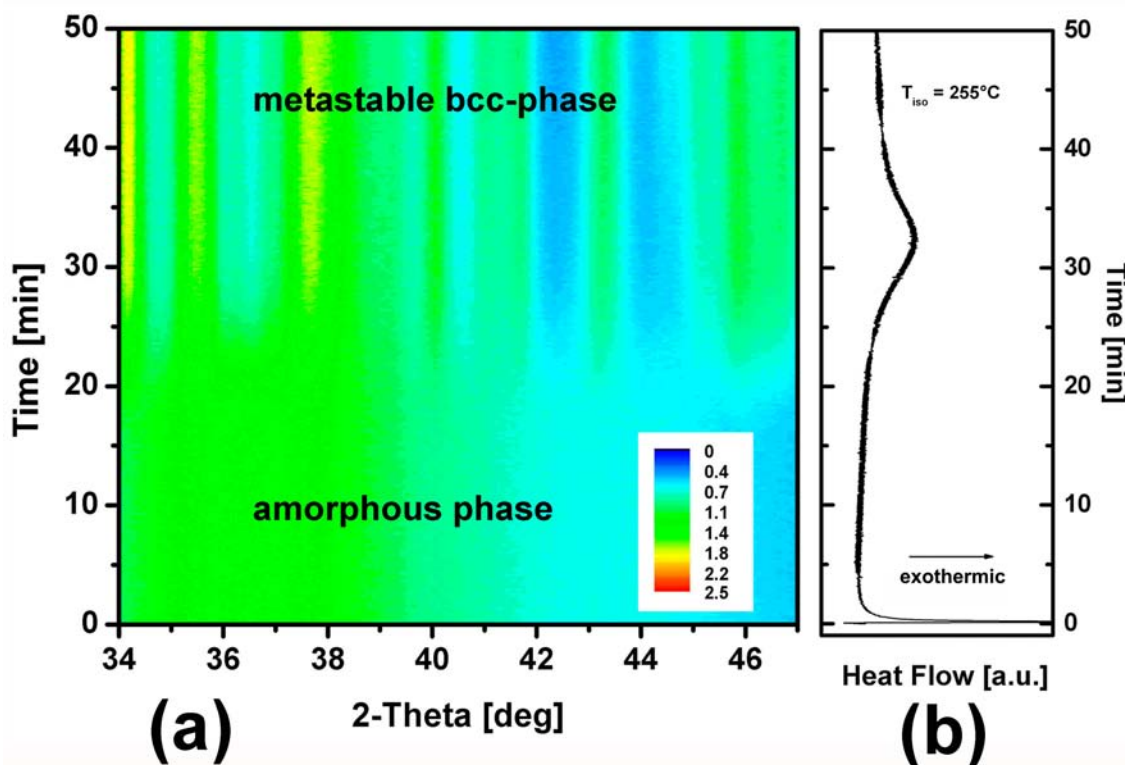


Figure 4.26: (a) In-situ XRD plot of a  $\text{Al}_{85}\text{Ni}_{10}\text{La}_5$  splat obtained during isothermal annealing at 255°C. The intensity is color coded. (b) DSC isothermal heat response of the same splat as described in (a).

Figure 4.26(a) shows in-situ XRD patterns of a  $\text{Al}_{85}\text{Ni}_{10}\text{La}_5$  splat obtained during isothermal heating at 255°C. Initial XRD patterns show a broad diffuse scattering max-

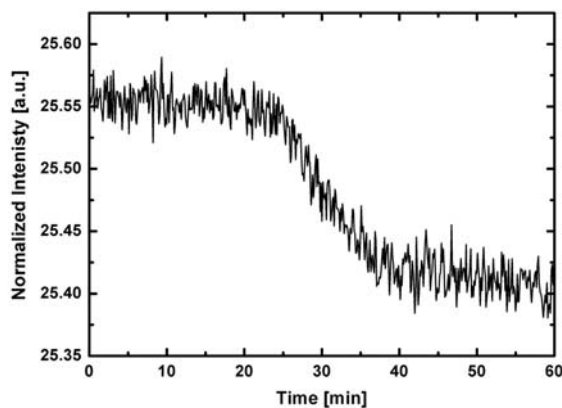


Figure 4.27: *In-situ X-ray attenuation of a  $Al_{85}Ni_{10}La_5$  splat obtained during isothermal annealing at  $255^{\circ}C$ .*

imum. Small and broad Bragg reflections of fcc-Al and metastable bcc-phase develop after approximately 20 min and increase in intensity with respect to the diffuse scattering level.

Figure 4.26(b) depicts the DSC curve of the same splat used in (a) during isothermal annealing at  $255^{\circ}C$ . After approximately 20 min a broad exothermic heat flow appears.

Figure 4.27(a) illustrates the in-situ X-ray attenuation plot of an  $Al_{85}Ni_{10}La_5$  splat during isothermal heating at  $255^{\circ}C$ . The intensity decreases between 24 min and 38 min dwelling time which corresponds to a mass density increase of 0.8%.



## **Chapter 5**

### **Experimental Results: Consolidation**

## 5.1 Hot Pressing of Al-Ni-La Metallic Glass Powders

This chapter deals with the characterization of amorphous and partially crystalline Al-Ni-La powder after consolidation by uni-axial hot pressing. Morphology, microstructure, and thermodynamical behavior are presented. Detailed investigations were made on pressing of helium-atomized  $\text{Al}_{85}\text{Ni}_{10}\text{La}_5$  powders. Due to the limited amount of helium-atomized  $\text{Al}_{85}\text{Ni}_{10}\text{La}_5$  powders, the powder used for hot pressing were made by mixing the two cyclone fractions of batch I ( $d_{50} = 6 \mu\text{m}$ ) and batch II ( $d_{50} = 6 \mu\text{m}$ ). In the following, this powder is named  $\text{Al}_{85}\text{Ni}_{10}\text{La}_5$  powder blend.

### 5.1.1 In-situ Monitoring of Hot Pressing

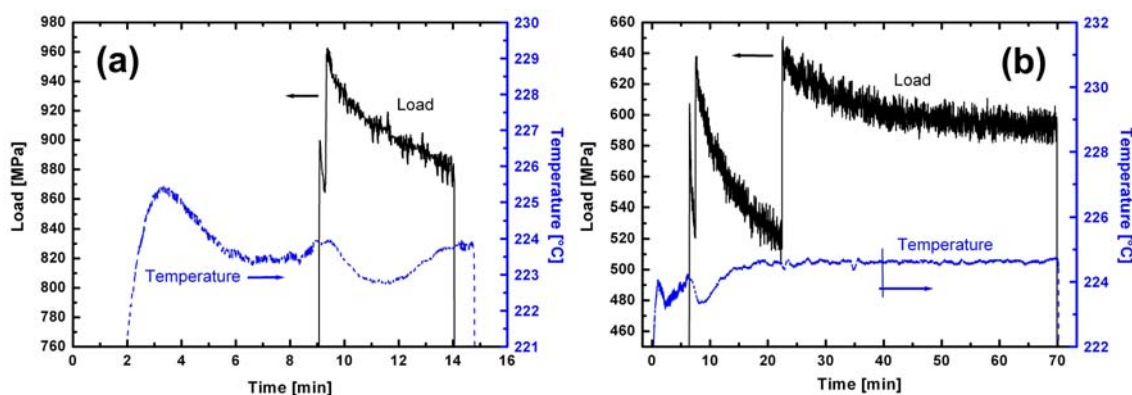


Figure 5.1: (a) In-situ load and temperature evolution during pressing at  $225^\circ\text{C}$  for 5 min applying at an initial load of 955 MPa, and (b) for 60 min applying an initial load of 637 MPa.

Figure 5.1 shows the in-situ load and temperature evolution during hot pressing at  $225^\circ\text{C}$ . Figure 5.1(a) shows a temperature variation of about  $2^\circ\text{C}$  can occur during hot pressing. Further experiments revealed that this overshoot can reach temperatures up to  $6^\circ\text{C}$  above temperature set (not presented here). Figure 5.1(a) shows that the initial load of approximately 955 MPa decreased within 5 min by about 8%. Figure 5.1(b) shows that during 60 min of hot pressing the initial load of 637 MPa drops by about 20% within 15 min. After 15 min the load increases rapidly in a small time range of a few seconds to the initial level. Afterwards, the load decreases at a slower rate compared to the first 15 min of the pressing experiment.

### 5.1.2 Morphology of Hot Pressed Samples

Figure 5.2(a) shows a hot pressed sample. Figure 5.2(b) illustrates a longitudinal cross-section of  $\text{Al}_{87}\text{Ni}_8\text{La}_5$  powder (batch II) consolidated by hot pressing at  $300^\circ\text{C}$ . Pores (black contrast) occur throughout the sample.

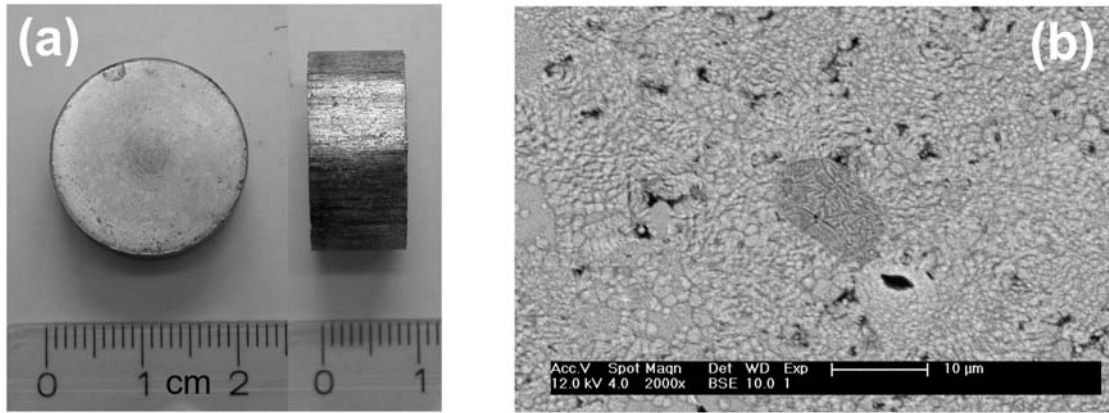


Figure 5.2: (a) Photograph of a hot pressed sample. (b) SEM-image of the longitudinal cross-section of  $\text{Al}_{87}\text{Ni}_8\text{La}_5$  powder (batch II) pressed at  $300^\circ\text{C}$ .

### 5.1.3 Density and Hardness of Hot Pressed Samples

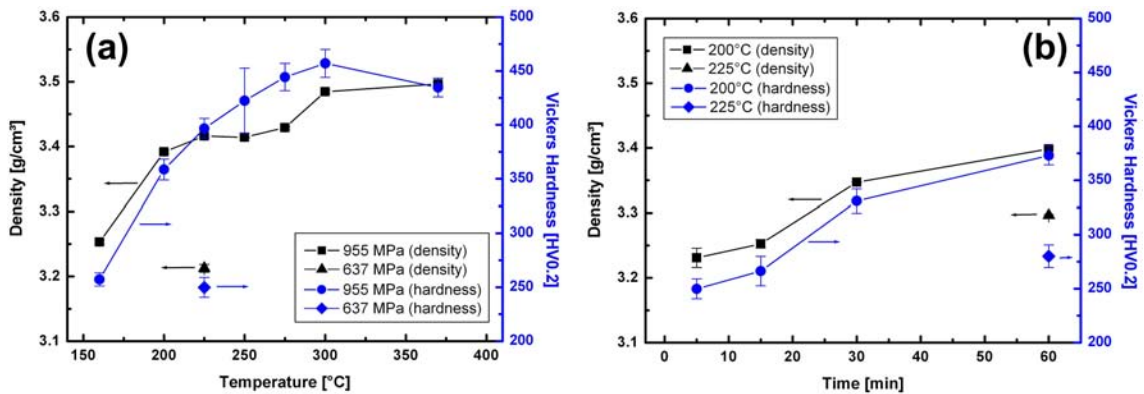


Figure 5.3: (a) Density and Vickers hardness of  $\text{Al}_{85}\text{Ni}_{10}\text{La}_5$  powder blend after hot pressing at different temperatures. An initial load of either 637 or 955 MPa was applied for 5 min. (b) Density and hardness of the same powder blend after hot pressing for different holding times using an initial load of 637 MPa. The temperature was held constant.

Figure 5.3(a) shows density and hardness curves of the  $\text{Al}_{85}\text{Ni}_{10}\text{La}_5$  powder blend after hot pressing at different temperatures. Density (squares) and hardness (circles) of samples pressed at an initial load of 955 MPa increase with pressing temperature. Maximum density of approximately  $3.5 \text{ g/cm}^3$  and maximum Vickers hardness of 457 HV0.2 can be observed at  $360^\circ\text{C}$  and  $300^\circ\text{C}$ , respectively. Density and hardness increase by about 7% and 44% between  $160^\circ\text{C}$  and  $360^\circ\text{C}$ , respectively. Density (triangles) and Vickers hardness (diamonds) of samples pressed at 637 MPa ( $225^\circ\text{C}$ ) drop approximately 6% and 37%, respectively, compared to samples pressed at 955 MPa.

Figure 5.3(b) represents density and hardness evolution of  $\text{Al}_{85}\text{Ni}_{10}\text{La}_5$  powder blend after hot pressing at different holding times. Specimens processed at  $225^\circ\text{C}$  show that density (squares) and hardness (circles) increase by about 5% and 43%, respectively, from 5 to 60 min dwelling time. Density and hardness of samples processed at  $200^\circ\text{C}$  (60 min)

decrease approximately 3% and 25%, respectively, compared to samples processed at 225°C (60 min).

### 5.1.4 XRD of Hot Pressed Samples

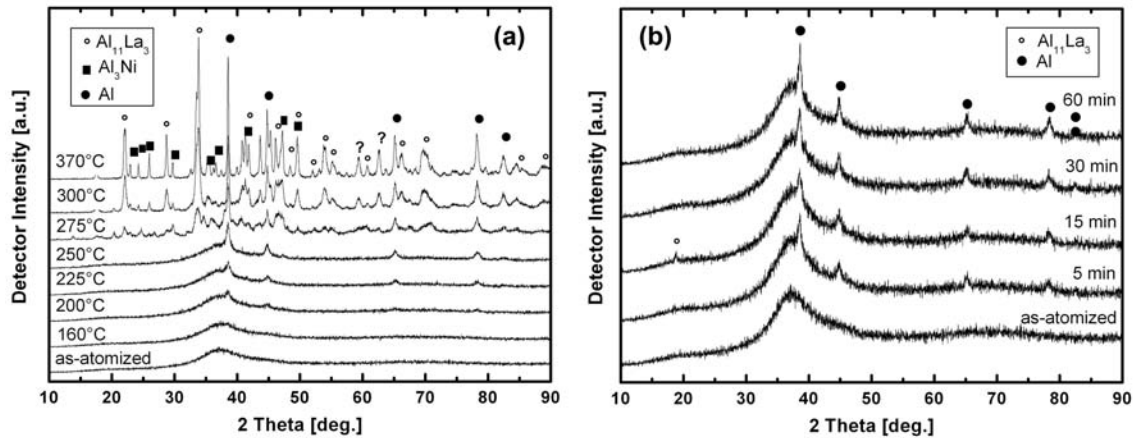


Figure 5.4: (a) XRD patterns of  $Al_{85}Ni_{10}La_5$  powder blend after hot pressing different pressing temperatures using an initial load of 955 MPa for 5 min. (b) XRD patterns of  $Al_{85}Ni_{10}La_5$  powder blend after hot pressing at 225°C for different dwelling times using an initial load of 637 MPa.

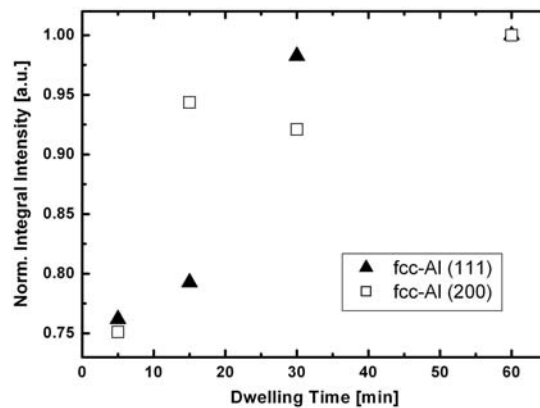


Figure 5.5: Normalized peak intensities of fcc-Al peaks of XRD patterns in figure 5.4(b).

Figure 5.4(a) shows XRD patterns of  $Al_{85}Ni_{10}La_5$  powder blend after hot pressing at different pressing temperatures. XRD patterns of powders, which were pressed between 160°C and 250°C, exhibit fcc-Al Bragg reflections and a broad diffuse scattering maximum. Low intensity Bragg reflections of the sample pressed at 160°C can be observed at higher magnification of the XRD intensity profile (not presented here). The intensities of the fcc-Al Bragg reflections increase with increasing pressing temperature. XRD patterns of powders, which were pressed between 275°C and 370°C, show Bragg reflections of

fcc-Al, Al<sub>3</sub>Ni and Al<sub>11</sub>La<sub>3</sub>. Their intensities increase and their peak widths decrease with increasing pressing temperature.

Figure 5.4(b) shows XRD patterns of Al<sub>85</sub>Ni<sub>10</sub>La<sub>5</sub> powder blend after hot pressing at 225°C for different dwelling times. XRD patterns of hot pressed samples exhibit fcc-Al Bragg reflections and a broad diffuse scattering maximum. The fcc-Al Bragg peak integral intensities increase with increasing dwelling time, as highlighted in figure 5.5.

### 5.1.5 Calorimetric Characterization after Hot Pressing

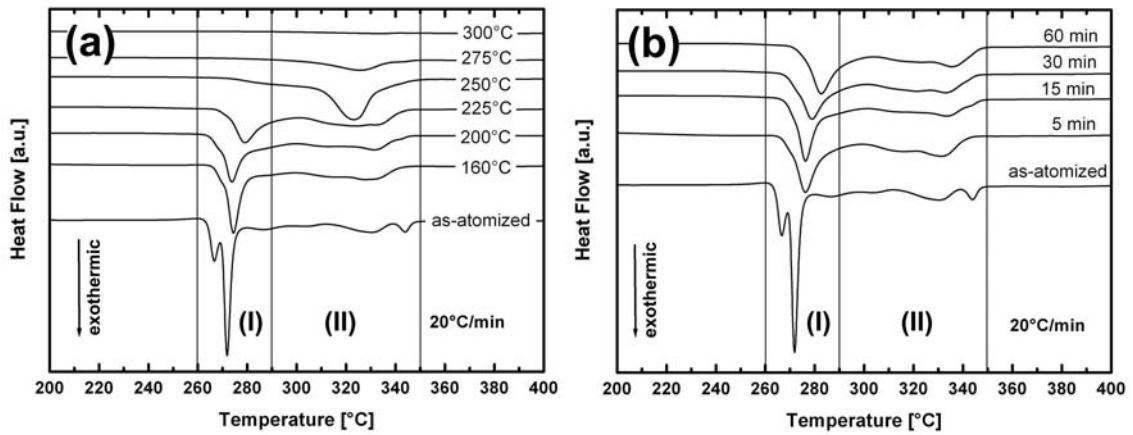


Figure 5.6: (a) DSC curves of Al<sub>85</sub>Ni<sub>10</sub>La<sub>5</sub> powder blend after hot pressing at different pressing temperatures, and (b) at different dwelling times obtained during continuous heating at 20°C/min.

Figure 5.6(a) illustrates DSC curves of Al<sub>85</sub>Ni<sub>10</sub>La<sub>5</sub> powder blend after hot pressing at different pressing temperatures obtained during continuous heating at 20°C/min. Two temperature ranges can be distinguished, at which several peaks develop. The DSC curve of as-atomized powder shows two large exothermic heat releases within temperature range (I) from 260 to 290°C. DSC curves of samples, which were pressed at higher temperatures, reveal that their minimum peaks shift towards higher temperatures with increasing pressing temperature. Their peak areas diminish at the same time. DSC curves of samples which were hot pressed at temperatures  $\geq 250^\circ\text{C}$  do not show peaks within temperature range (I). In temperature range (II), from 290 to 350°C, many small exothermic heat releases occur in the DSC curve of as-atomized powder. DSC heat responses of hot pressed samples show that total peak areas in temperature range (II) increase with pressing temperature. The sample pressed at 300°C shows no heat response.

Figure 5.6(b) shows DSC curves of Al<sub>85</sub>Ni<sub>10</sub>La<sub>5</sub> powder blend after hot pressing at different dwelling times. These DSC curves show that minimum peaks within the temperature range (I) shift towards higher temperatures with increasing dwelling time.

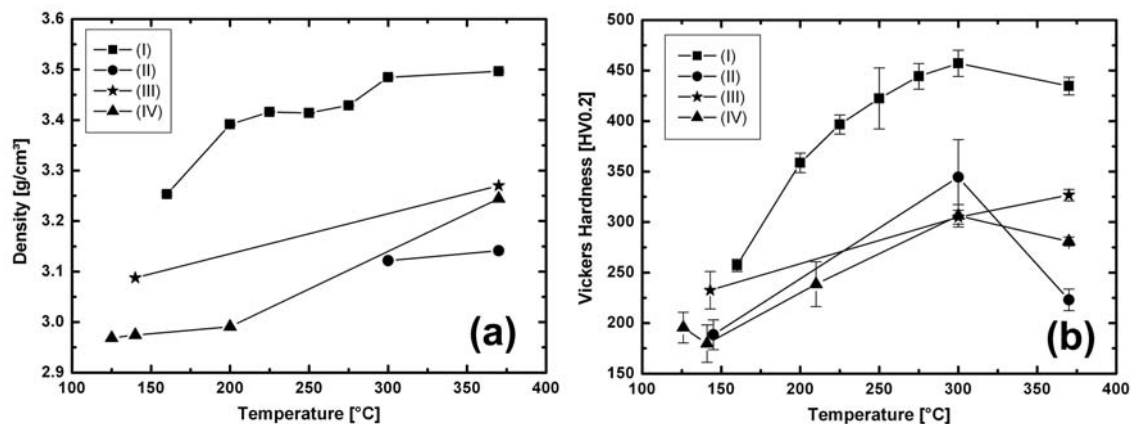


Figure 5.7: Density (a) and Vickers hardness (b) of helium-atomized  $Al_{85}Ni_{10}La_5$  powder blend (I, squares), helium-atomized  $Al_{87}Ni_8La_5$  powders batch I (II, circles), helium-atomized  $Al_{87}Ni_8La_5$  powders batch II (III, stars), and argon-atomized  $Al_{87}Ni_8La_5$  powders (IV, triangles) after hot pressing at different temperatures. All pressing experiments were performed using an initial load of 955 MPa for 5 min.

### 5.1.6 Hot Pressing of Different Alloy Powders

Figure 5.7 shows (a) density, and (b) hardness evolution of hot pressed helium-atomized  $Al_{85}Ni_{10}La_5$  powder blend (squares), helium-atomized  $Al_{87}Ni_8La_5$  powders batch I (circles), helium-atomized  $Al_{87}Ni_8La_5$  powders batch II (stars), and argon-atomized  $Al_{87}Ni_8La_5$  powders (triangles). The density and hardness of hot pressed samples increase with increasing pressing temperature. Maximum hardness values were measured at samples, which were pressed at 300°C (except hot pressed helium-atomized  $Al_{87}Ni_8La_5$  powder, batch II). The maximum hardness of hot pressed  $Al_{87}Ni_8La_5$  powders ranges from 305 to 345 HV0.2. The maximum density value of hot pressed  $Al_{87}Ni_8La_5$  powders is approximately  $3.2 \pm 1$  g/cm<sup>3</sup>. The maximum density and Vickers hardness values of hot pressed  $Al_{87}Ni_8La_5$  powders are smaller by about 8% and 35%, respectively, compared to hot pressed  $Al_{85}Ni_{10}La_5$  powders.

## 5.2 ECAP of Al-Ni-La Metallic Glass Powder

This chapter deals with the characterization of helium-atomized  $Al_{85}Ni_{10}La_5$  powders after its consolidation by Equal Channel Angular Pressing (ECAP) at different processing temperatures using a conventional ECAP and a zic-zac ECAP die. Powders of batch I ( $d_{50} = 11$  μm) and of batch II ( $d_{50} = 12$  μm) were consolidated separately (without mixing). Morphology, microstructure and thermodynamical behavior of ECAP-consolidated samples are presented.

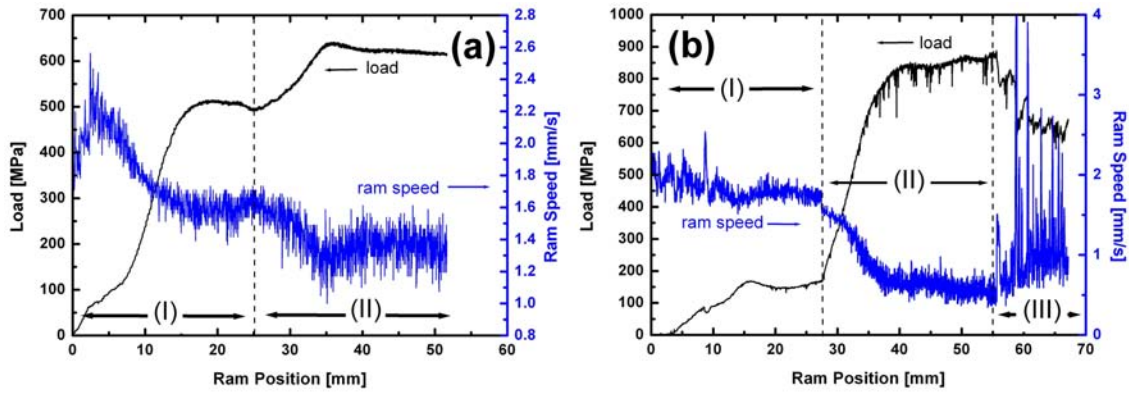


Figure 5.8: Load (black curve) and ram speed (blue curve) evolution vs. ram propagation during ECAP at (a) 225°C using a conventional ECAP die, and (b) at 175°C using a zic-zac ECAP die.

### 5.2.1 Load and Ram Speed Evolution during ECAP

The black curve in figure 5.8(a) represents the load evolution during ECAP at 225°C using a conventional ECAP die. The load increases in two steps during ram propagation. At first, load increases up to about 500 MPa within a ram propagation from 0 to approximately 25 mm (I). During further ram propagation (II), the pressing load increases up to approximately 640 MPa. Load increases in (I) and (II) are accompanied by reduction of ram speed (blue curve) from initial 2.2 mm/s to final 1.4 mm/s.

Figure 5.8(b) presents load and ram speed evolution during ECAP at 175°C using a zic-zac ECAP die. The pressing load (black curve) increases with ram propagation in two steps (I) from zero to approximately 160 MPa, and (II) from 163 MPa to approximately 850 MPa. During further load propagation indicated by ram position range (III), the load drops by about 100 MPa. At the same time, ram speed increases. Alterations of load and ram speed in (III) indicate a non steady pressing process.

### 5.2.2 Morphology of ECAP Processed Samples

Figure 5.9 shows photographs of the longitudinal cross section of ECAP samples (a) processed at 225°C using a conventional ECAP die, and (b) processed at 175°C using a zic-zac ECAP die. Both samples show big voids in front of the Cu-container. Cracks appear mostly along the upper side of the can. Cracks after conventional ECAP consolidation in figure 5.9(a) are almost parallel to the front of the can. The Cu-container front is further propagated at the bottom side, as compared to the upper side. Contrary to the Cu-can front, the front of the consolidated powders is almost parallel to the theoretical 45° shear plane. In contrast to conventional ECAP, cracks of a zic-zac ECAP consolidated sample in figure 5.9(b) are parallel to the shear plane. Generally, conventional ECAP consolidated samples show a macroscopically more homogeneous cross sectional surface with less cracks and voids, as compared to zic-zac ECAP consolidated samples.

Figure 5.10 represents a SEM-image of the longitudinal cross section of a ECAP sample processed at 200°C using the zic-zac ECAP die. It shows a consolidated and

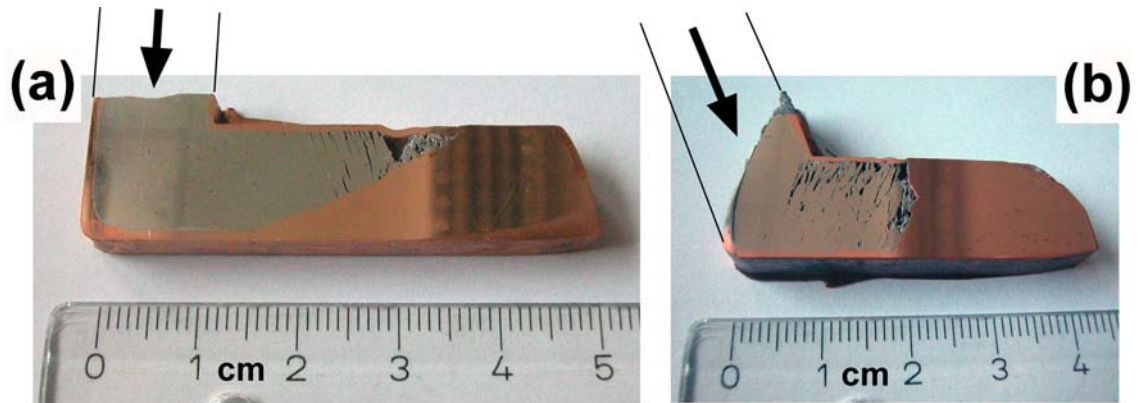


Figure 5.9: Photographs of the longitudinal cross section of ECAP samples (a) processed at 225°C using a conventional ECAP die, and (b) processed at 175°C using a zic-zac ECAP die.

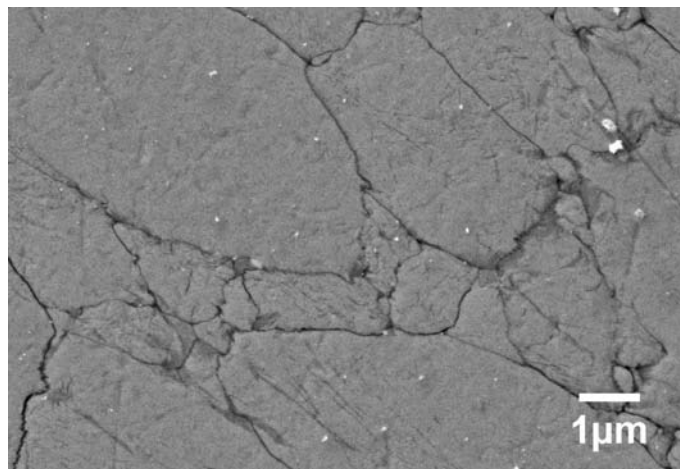


Figure 5.10: SEM-image of the longitudinal cross section of a ECAP sample processed at 200°C using a zic-zac ECAP die.

crack free region, at which plastically deformed and well integrated powder particles can be observed.

### 5.2.3 Density and Hardness of ECAP Processed Samples

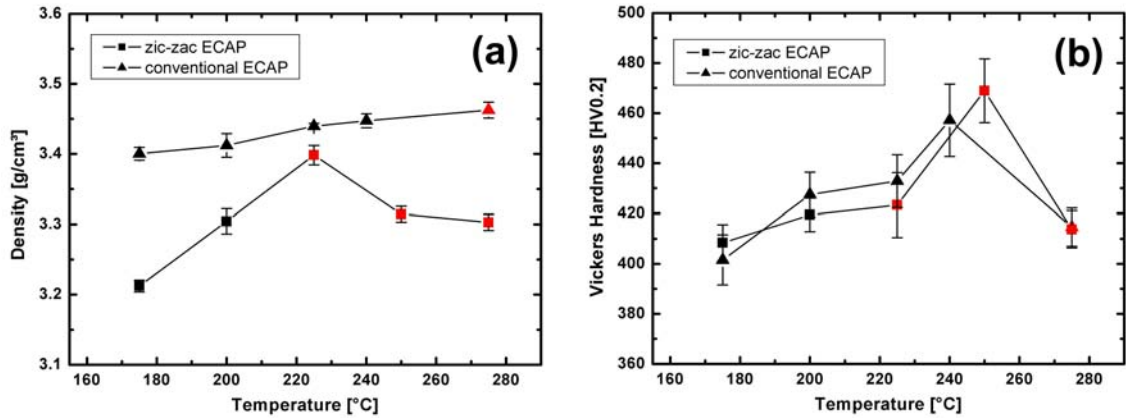


Figure 5.11: (a) Density, and (b) hardness evolution of ECAP samples obtained at different processing temperatures using a conventional, and a zic-zac ECAP die. Black symbols indicate that helium-atomized  $Al_{85}Ni_{10}La_5$  powder batch I was used, whereas red symbols indicate the use of batch II of the same alloy.

Figure 5.11(a) presents the density of ECAP-consolidated  $Al_{85}Ni_{10}La_5$  powder obtained at different temperatures using a conventional and a zic-zac ECAP die. Compared to zic-zac ECAP-consolidated samples, conventional ECAP-consolidated samples show higher densities at equal processing temperatures. The density increases with temperature by about 1.8% up to  $3.5 \text{ g/cm}^3$  in case of conventional ECAP. The density of zic-zac ECAP consolidated samples exhibits a maximum of  $3.4 \text{ g/cm}^3$  at the sample processed at  $250^\circ\text{C}$ .

Figure 5.11(b) shows the Vickers hardness evolution of ECAP samples as described in (a). Regardless of the die used, both show the same tendency. In a processing temperature range from  $175^\circ\text{C}$  to  $225^\circ\text{C}$ , Vickers hardness increases by about 3-5%. ECAP samples processed at  $240^\circ\text{C}$  (conventional ECAP die) and  $250^\circ\text{C}$  (zic-zac ECAP die) exhibit maximum hardness values of 460 HV0.2 and 470 HV0.2, respectively.

### 5.2.4 XRD of ECAP Processed Samples

Figure 5.12(a) presents XRD patterns of conventional ECAP consolidated samples obtained at different processing temperatures. XRD patterns of samples consolidated at temperatures ranging from  $175^\circ\text{C}$  to  $240^\circ\text{C}$  show fcc-Al Bragg reflections and a broad diffuse scattering maximum. Fcc-Al Bragg peak intensities increase with increasing processing temperature. Copper Bragg reflections originate from a copper-can. Similar XRD patterns can be observed for zic-zac consolidated samples processed at temperatures ranging from  $175^\circ\text{C}$  to  $250^\circ\text{C}$ , as illustrated in figure 5.12(b). Regardless of the die used, XRD

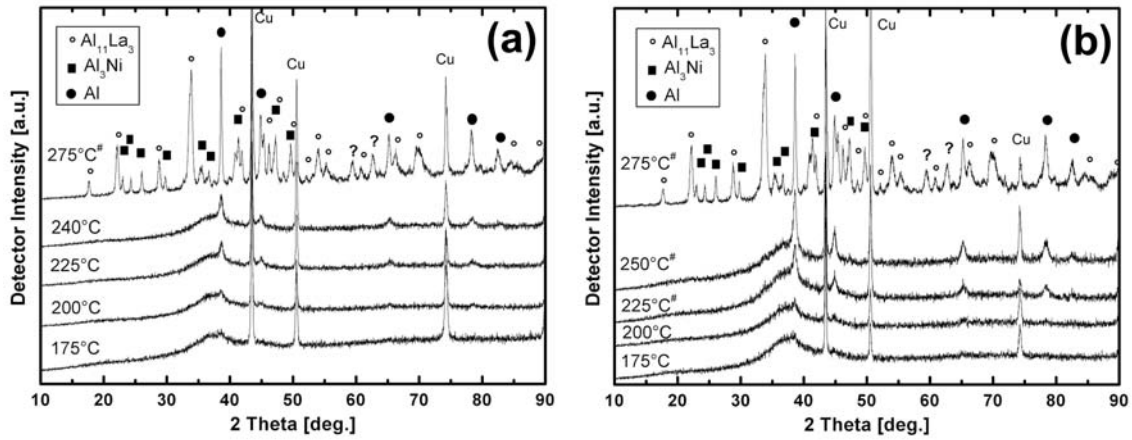


Figure 5.12: XRD patterns of helium-atomized  $Al_{85}Ni_{10}La_5$  powder, which were consolidated at different processing temperatures using (a) a conventional ECAP die, and (b) a zic-zac ECAP die.

patterns of samples consolidated at  $275^\circ C$  exhibit Bragg reflections of fcc-Al,  $Al_3Ni$  and  $Al_{11}La_3$ .

### 5.2.5 Calorimetric Characterization after ECAP

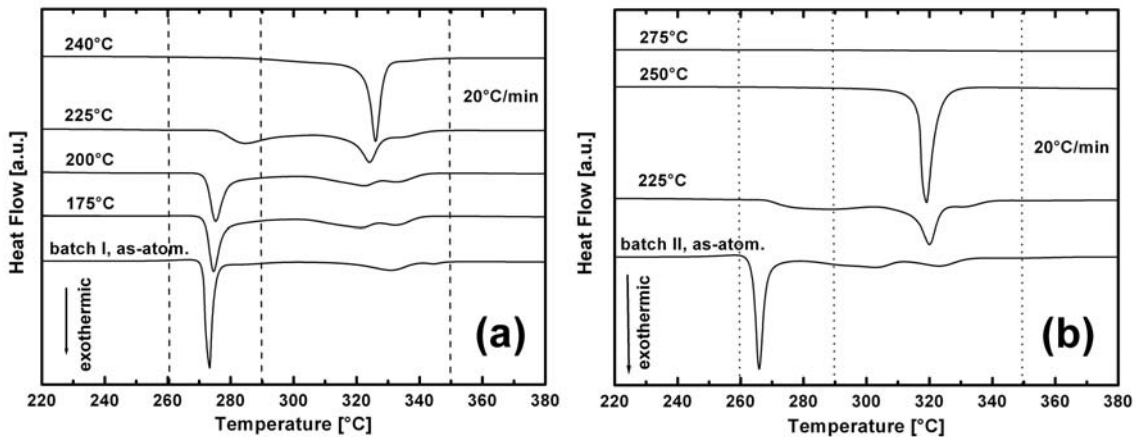


Figure 5.13: DSC continuous heating traces at  $20^\circ C/min$  of helium-atomized  $Al_{85}Ni_{10}La_5$  powder (batch I), which was consolidated at different processing temperatures using (a) a conventional ECAP die, and (b) a zic-zac ECAP die.

Figure 5.13(a) illustrates DSC curves ( $20^\circ C/min$ ) of helium-atomized  $Al_{85}Ni_{10}La_5$  powder (batch I) consolidated at different processing temperatures using a conventional ECAP die. In comparison to as-atomized powder, no glass transition can be observed in the DSC curves of ECAP samples. A large exothermic heat release in DSC curves, which develop during heating from  $260$  to  $290^\circ C$ , diminish with increasing processing temperature. Their minimum peaks shift towards higher temperatures. At the same time, a group of small exothermic events, which develop during heating from  $290$  to  $350^\circ C$ ,

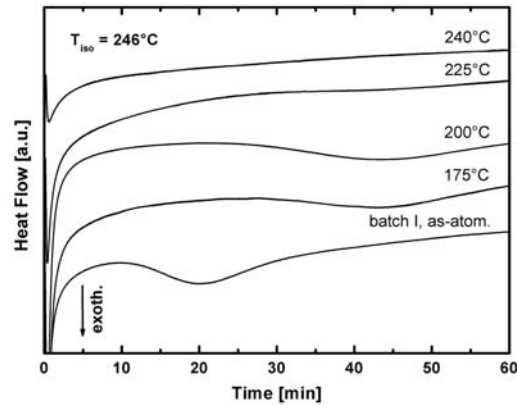


Figure 5.14: DSC curves obtained during isothermal heating at 246°C of samples consolidated at different temperatures using the conventional ECAP die.

increase in peak area. The DSC curve of a ECAP sample processed at 240°C shows a curve minimum at 326°C. A similar tendency can be observed in the DSC heat response of zic-zac ECAP consolidated samples, as presented in figure 5.13(b).

Figure 5.14 shows DSC isothermal heating traces at 246°C of ECAP-consolidated helium-atomized  $\text{Al}_{85}\text{Ni}_{10}\text{La}_5$  powder (batch I) obtained at different process temperatures using a conventional ECAP die. The curve minimum at approximately 20 min in the DSC curve of as-atomized powder has shifted towards longer dwelling times, as compared to DSC curves of ECAP samples, which were processed at 175°C and 200°C. At 225°C and 240°C, these minimum peaks cannot be detected any more.

### 5.2.6 Influence of Plastic Deformation on Morphology

Figure 5.15 shows a longitudinal cross section of a ECAP-consolidated  $\text{Al}_{85}\text{Ni}_{10}\text{La}_5$  powder (batch II) processed at 250°C using a conventional ECAP die. The sample was stopped halfway to study the influence of plastic shear deformation on powder particle morphology. SEM-images at right and bottom side of the macroscopic photograph show enlarged sample areas along the longitudinal cross section, namely in regions of the entrance channel (A-B), the corner (channel intersection), and the exit channel (C-D).

SEM-images reveal that powder particles elongate and rotate (indicated by red arrows) from A to D. The powder particles are well integrated into a dense assembly. Figure 5.16(a) shows powder particle dimension and rotation angle  $\alpha$  along the entrance channel from A to B. After 4 mm from point A, the strain  $\epsilon$  along the major axis  $a$  increases from 0.2 to 1.5. The strain along minor axis  $b$  decreases from 0.2 to 0.6, respectively.

Figure 5.16(b) shows powder particle dimensions and rotation angle along the exit channel from C to D. The strain  $\epsilon$  along major axis  $a$  increases along the exit channel from 1 to maximum strain 1.6 at 8 mm distance from point C. The minor axis  $b$  increases slightly from 0.45 to 0.6, respectively. After 8 mm from point C,  $a$  and  $b$  approach a strain

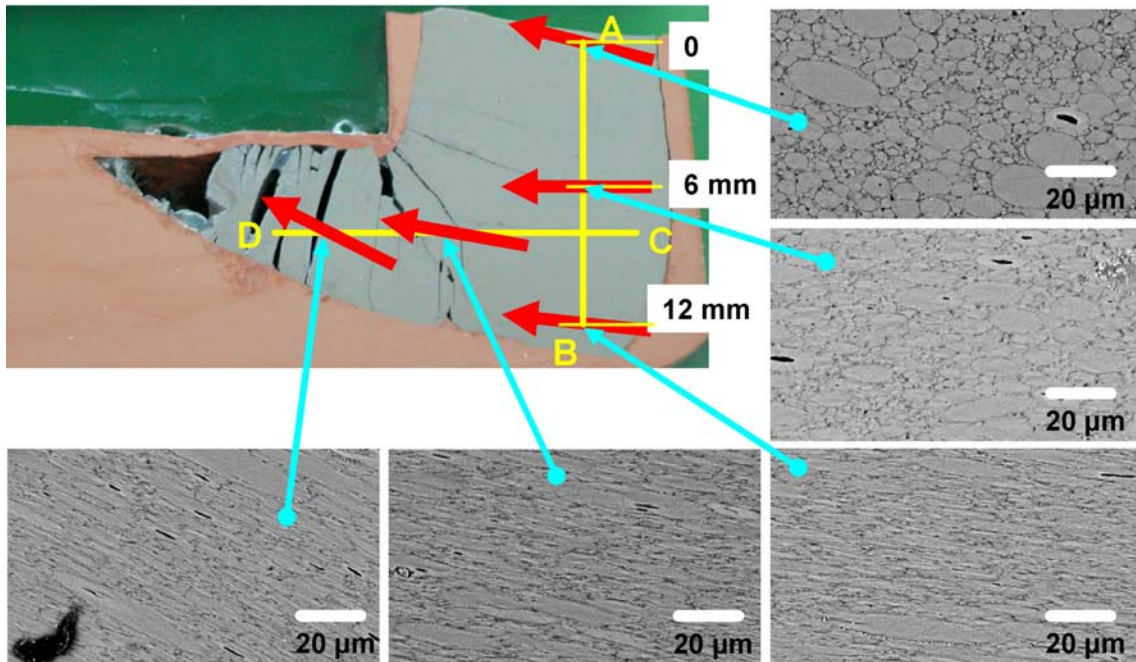


Figure 5.15: Photograph of a longitudinal cross section of  $Al_{85}Ni_{10}La_5$  powder (batch II), which was consolidated at  $250^\circ C$  using a conventional ECAP die. The sample was stopped halfway. SEM-images at the right and bottom side of the photograph show enlarged sample areas.

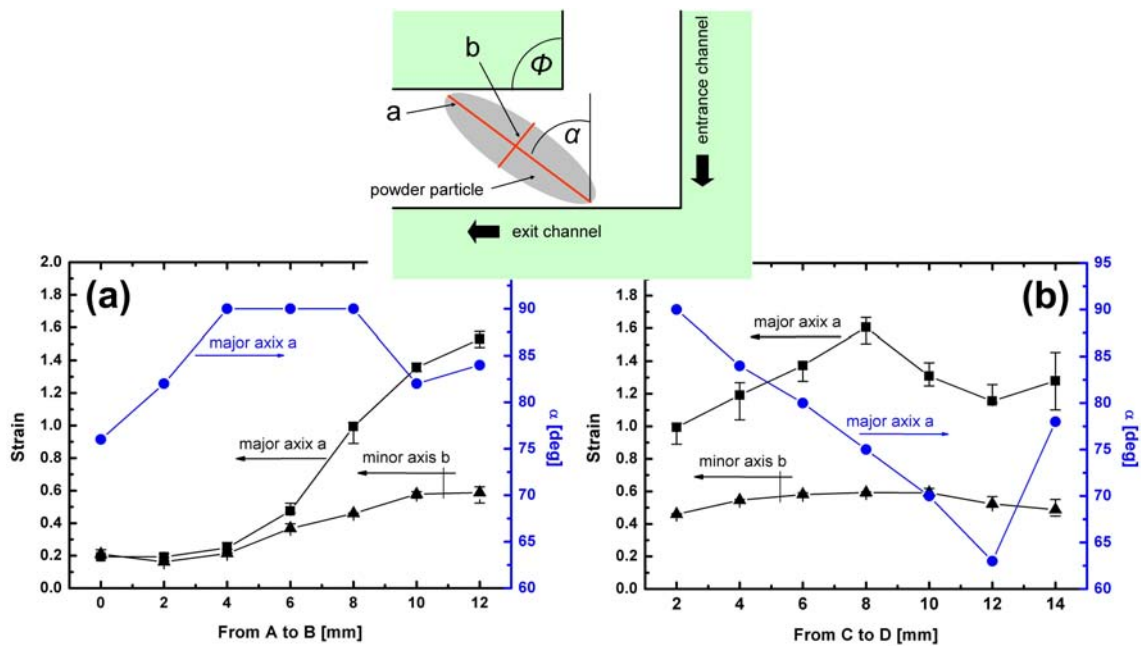


Figure 5.16: The evolution of powder particle strain and its rotation from A-B (a) and from C-D (b), as indicated in figure 5.15.

level of approximately 1.25 and 0.5, respectively. Elongated powder particles rotate along the exit channel from  $\alpha = 90^\circ$  to  $\alpha = 63^\circ$ .

### 5.2.7 Influence of Plastic Deformation on Density, Hardness, Structure

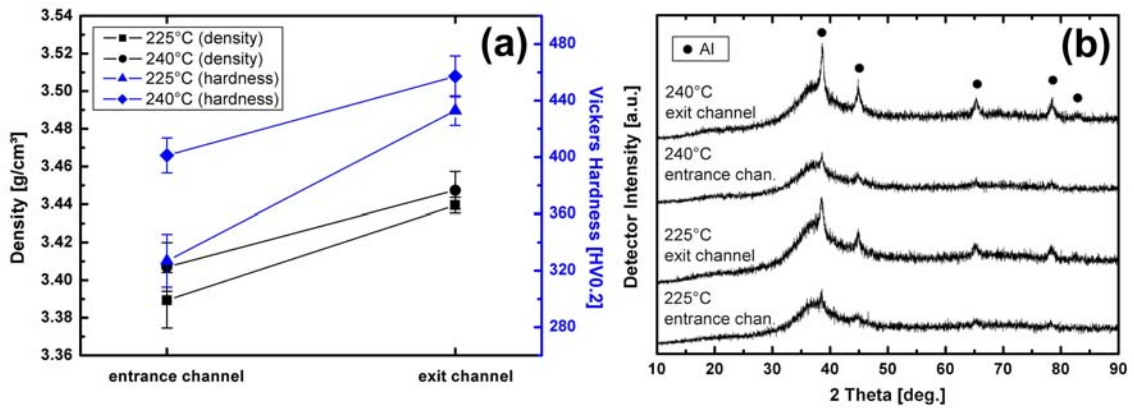


Figure 5.17: (a) Density, Vickers hardness, and (b) XRD patterns of conventional ECAP-consolidated  $\text{Al}_{85}\text{Ni}_{10}\text{La}_5$  powder (batch I) processed at 225°C and 240°C. The samples were stopped halfway.

Figure 5.17(a) shows density and Vickers hardness of conventional ECAP-consolidated  $\text{Al}_{85}\text{Ni}_{10}\text{La}_5$  powder (batch I) processed at 225°C and 240°C. The samples were stopped halfway. Density and Vickers hardness between entrance and exit channel at 240°C increase slightly by about 1.2% from 3.40 to 3.44 g/cm<sup>3</sup>, and by about 13% from 400 to 460 HV0.2, respectively. The density and the hardness between entrance and exit channel after ECAP process at 225°C increase by about 1.5% from 3.39 to 3.44 g/cm<sup>3</sup>, and by about 30% from 330 to 430 HV0.2, respectively.

Figure 5.17(b) shows XRD patterns of samples described in figure 5.17(a). All XRD patterns show fcc-Al Bragg reflections and a broad diffuse scattering maximum. Intensities of fcc-Al Bragg reflections increase in the exit channel region compared to the entrance channel region.

### 5.2.8 Influence of Plastic Deformation on Calorimetric Behavior

Figure 5.18(a) illustrates DSC continuous heating traces at 20°C/min of ECAP samples, as described in figure 5.17. The exothermic heat release, which develops during heating from 260 to 290°C, decreases for samples extracted in the exit channel region compared to those extracted in the entrance channel region. At the same time, the total peak area of a group of peaks (exothermic heat releases), which develop during heating from 290 to 350°C, increases.

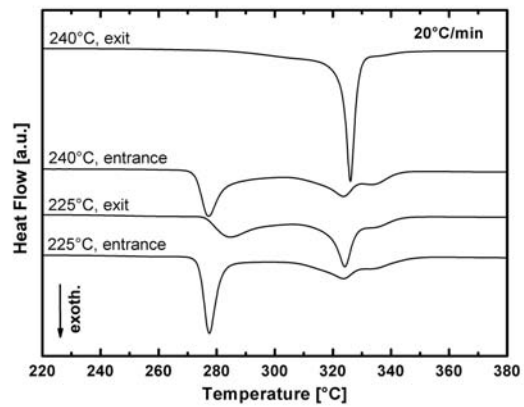


Figure 5.18: DSC continuous heating traces at 20°C/min of ECAP samples, as described in figure 5.17.

### 5.3 HPT of Al-Ni-La Metallic Glass Powder

This chapter deals with the characterization of helium-atomized  $\text{Al}_{85}\text{Ni}_{10}\text{La}_5$  powder (batch I,  $d_{50} = 11 \mu\text{m}$ ) after its consolidation by High Pressure Torsion (HPT) applying different levels of torsion. Morphology, structure and thermodynamical behavior are herein presented.

#### 5.3.1 Morphology and Density as a Function of Torsion

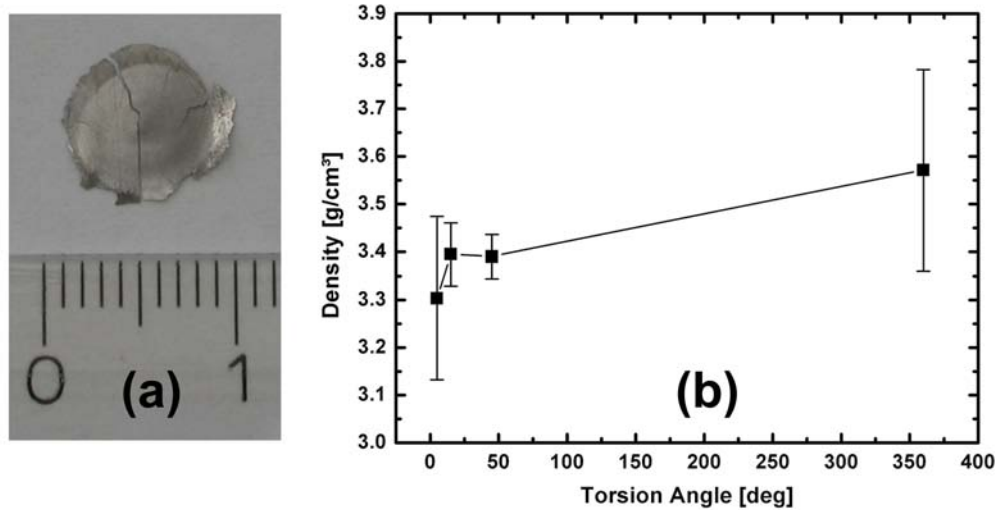


Figure 5.19: (a) Photograph of disc D360. (b) Density of disc samples obtained by applying different angles of torsion.

Figure 5.19(a) shows a photograph of disc D360. The disc is broken into 2 pieces. It further exhibits macroscopic cracks. The 4 HPT disc samples used (D5, D15, D45 and D360) have a diameter of 8 mm and a thickness between 92 and 179  $\mu\text{m}$ . All of them broke into 2 or more pieces. Figure 5.19(b) shows the density of discs subjected to different angles of torsion. The density ranges from 3.3 to 3.6  $\text{g/cm}^3$ .

Figure 5.20(a) shows SEM-images of disc surfaces of disc D5, D15, D45 and D360. They reveal flake-like features. Figures 5.20(b) and (c) present SEM-images of radial, cross-sectional fracture surfaces of disc D5, D15, D45 and D360. Discs D5, D15, and D45 show powder particle features over the whole cross sectional area. The fracture surface of disc D360 exhibits a sandwich structure. The middle layer of the sandwich structure shows powder particle features.

#### 5.3.2 Morphology in Radial Direction

Figure 5.21(a) presents SEM-images of the radial, cross-sectional fracture surface of disc D360. It reveals a sandwich structure. The width of top and bottom layers increase in radial direction. Top and bottom layer width is approximately 20  $\mu\text{m}$  at the disc center, and

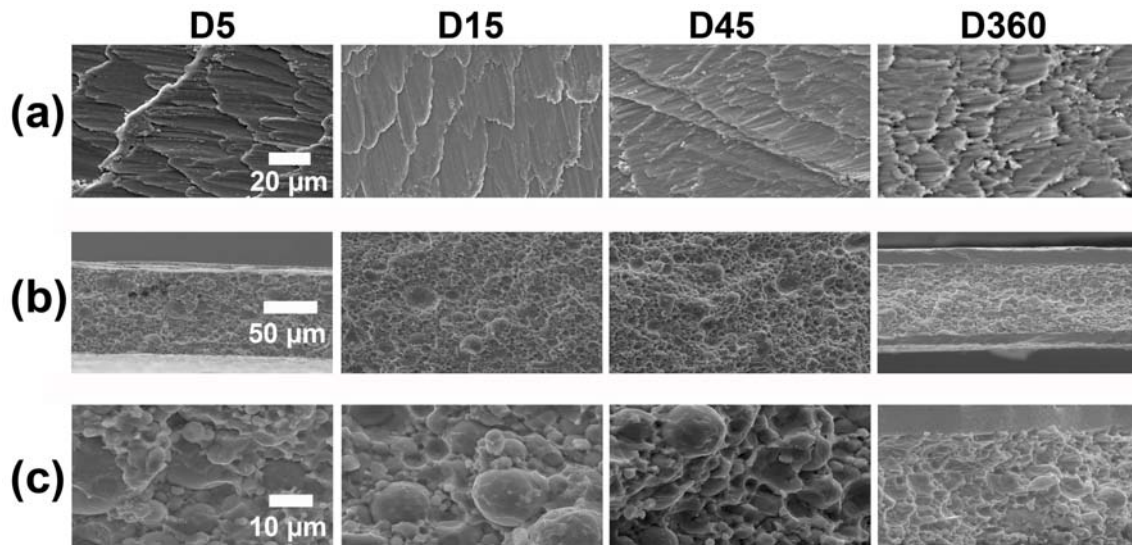


Figure 5.20: Row (a): SEM-images of disc surfaces of disc D5, D15, D45 and D360. Row (b) and (c): SEM-images of the radial, cross-sectional fracture surface of disc D5, D15, D45 and D360 at different magnifications.

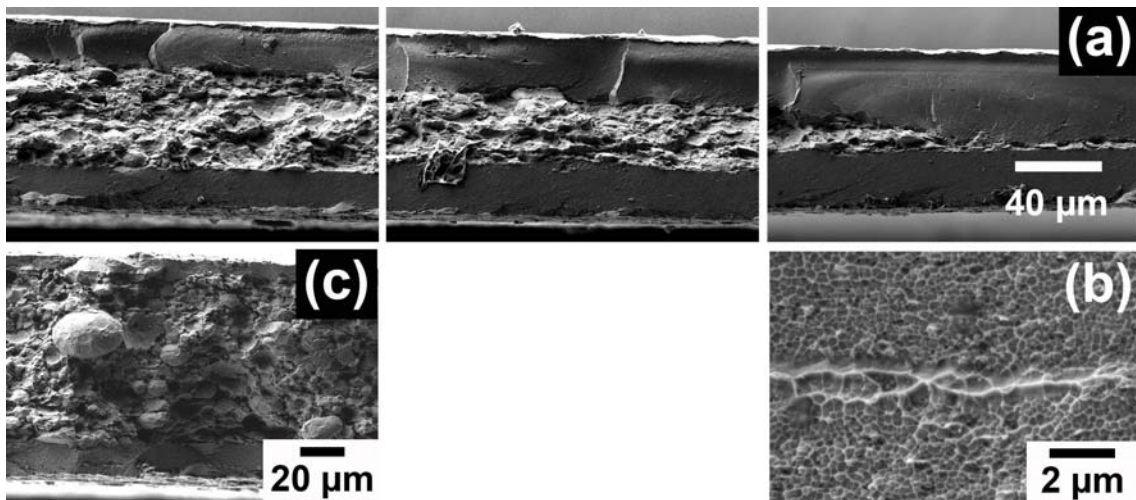


Figure 5.21: (a) SEM-images of the radial, cross-sectional fracture surface of disc D360 showing a sandwich structure with a top, middle and bottom layer. (b) SEM-image of an enlarged area of the top layer region. (c) SEM-image of an enlarged area of the middle layer region.

30  $\mu\text{m}$  near the disc edge. Furthermore, the disc thickness decreases in radial direction. Figure 5.21(b) shows a SEM-image of an enlarged area of the top layer of D360. It shows vein patterns. Figure 5.21(c) shows a SEM-image of an enlarged area of the middle layer, which exhibits powder particle features. The powder particles in the middle layer are well integrated and elongated in radial direction.

### 5.3.3 XRD and Calorimetric Characterization as a Function of Torsion

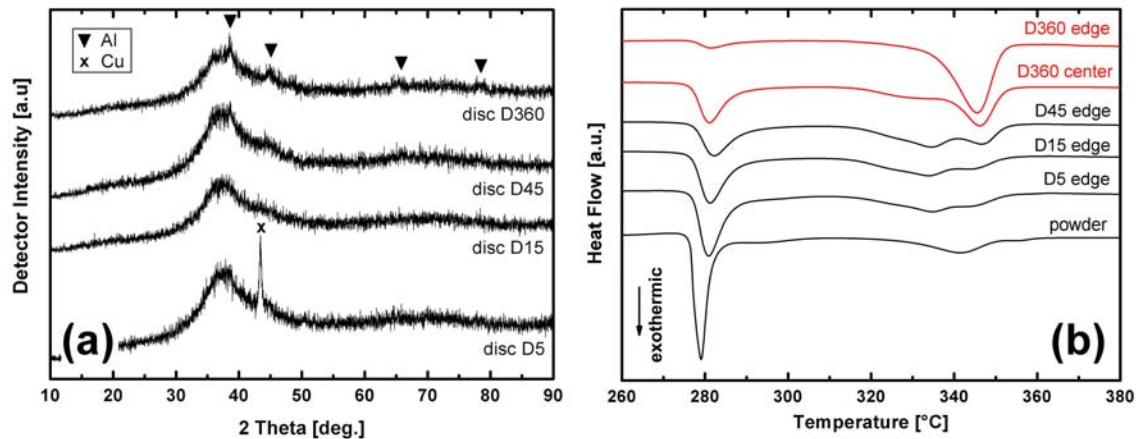


Figure 5.22: (a) XRD patterns of discs D5, D15, D45 and D360. (b) DSC curves of samples extracted from edge and center regions of HPT discs obtained during continuous heating at 40°C/min.

Figure 5.22(a) shows XRD patterns of discs D5, D15, D45 and D360. XRD patterns of disc D5 show a broad diffuse scattering maximum and a Cu Bragg reflection. Cu Bragg reflection stem from Cu powder residues of a precedent HPT experiment. XRD patterns of D15 show a broad diffuse scattering maximum. Discs D45 and D360 show a broad diffuse scattering maximum and fcc-Al Bragg reflections. The intensities of fcc-Al Bragg reflections are higher in XRD patterns of disc D360, as compared to those of disc D45. Top and bottom side of each disc reveal similar XRD patterns (not presented here).

Figure 5.22(b) depicts DSC continuous heating traces at 40°C/min of HPT discs D5, D15, D45, and D360. Looking at the DSC curves of samples taken from the edge region of the discs: compared to as-atomized powder, peak areas of the first exothermic heat release decreases with increasing torsion levels from D5 edge to D360 edge. At the same time, a group of peaks (exothermic heat releases), which develop between 290 and 350°C, increase in peak area. No glass transition can be observed in DSC curves of disc samples. The total heat release decreases with increasing angle of torsion, from 120 J/g of D5, 116 J/g of D15, 98 J/g of D45, to 93 J/g of D360.

Red DSC curves in figure 5.22(b) show a difference in heat flow between edge and center of disc D360. The DSC curve of the disc edge shows a smaller first exothermic peak area and a bigger second exothermic peak area, as compared to the disc center.

## 5.3.4 XRD and Calorimetric Characterization in Radial Direction

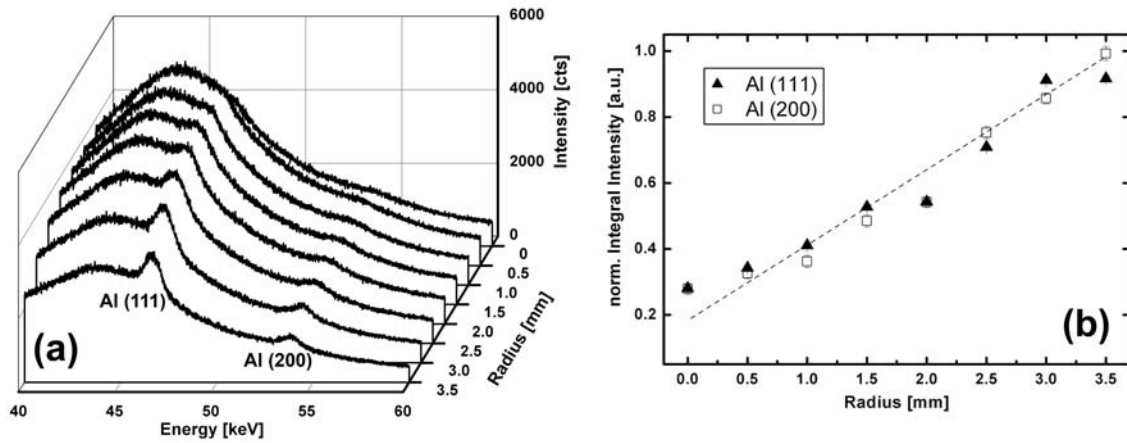


Figure 5.23: (a) Energy-dispersive XRD patterns along the disc radius of disc D360, and (b) the normalized integral intensities of (111) and (200) fcc-Al Bragg reflections.

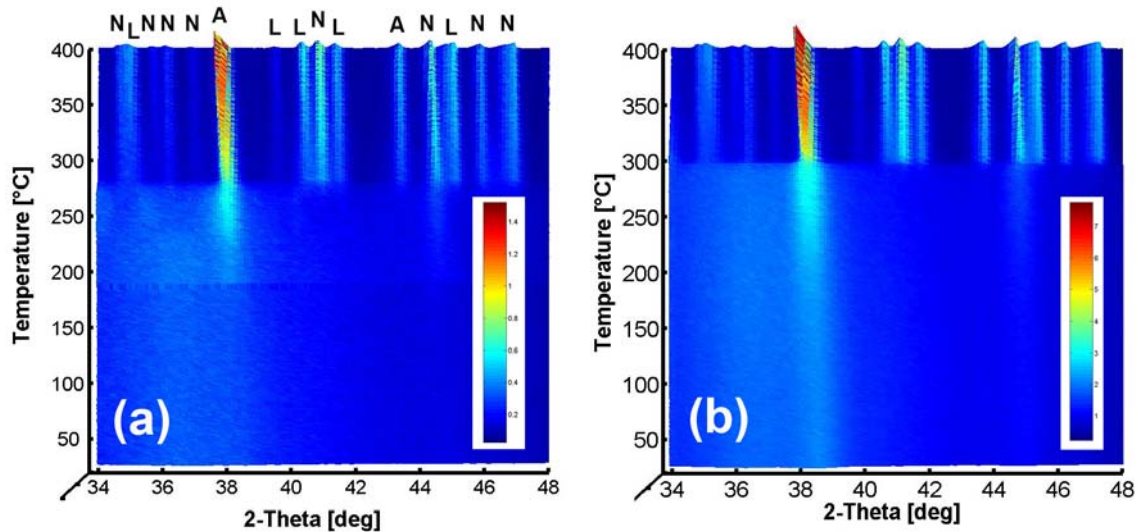


Figure 5.24: In-situ XRD plot of (a) center, and of (b) edge region of disc D360 obtained during continuous heating at  $10^\circ\text{C}/\text{min}$ . Different X-ray intensities are indicated by different colors. Letters A, N, and L denote Bragg reflections of fcc-Al,  $\text{Al}_3\text{Ni}$ , and  $\text{Al}_{11}\text{La}_3$  phase, respectively.

Figure 5.23(a) shows energy-dispersive XRD patterns of disc D360, which were measured in steps of  $500\ \mu\text{m}$  along the disc radius. XRD patterns at the disc center (radius = 0) show a broad diffuse scattering maximum similar to XRD patterns of as-atomized powder. XRD patterns at the disc edge (radius 3.5 mm) exhibit a broad diffuse scattering maximum superimposed by (111) and (200) fcc-Al Bragg reflections. The intensities of (111) and (200) fcc-Al Bragg reflections increase with distance from the disc center to the edge. This tendency is highlighted by a figure 5.23(b), where integral intensities of (111) and (200) fcc-Al Bragg reflections increase along the disc radius.

Figure 5.24 shows in-situ XRD plots of center and of edge region of disc D360 obtained during continuous heating at 10°C/min. XRD patterns at room temperature of the center region in figure (a) shows a broad diffuse scattering maximum and small (111) and (200) fcc-Al Bragg reflections. Intensities of fcc-Al Bragg reflections increase during continuous heating from room temperature to 274°C. At 274°C, additional Bragg reflections of Al<sub>3</sub>Ni and Al<sub>11</sub>La<sub>3</sub> occur within a narrow temperature range. All Bragg peaks shift to smaller 2 $\Theta$ -values between 271°C and 400°C. At the same time, their peak intensities increase significantly.

XRD patterns at room temperature of the edge region of disc D360 (figure 5.24(b)) show fcc-Al Bragg reflections, which are higher than those of the center region (figure 5.23(a)). The intensities of fcc-Al Bragg reflections increase during continuous heating from room temperature to 291°C. At 291°C, Bragg reflections of Al<sub>3</sub>Ni and Al<sub>11</sub>La<sub>3</sub> develop within a narrow temperature range.

## 5.4 Extrusion and HSS of Al-Ni-La Metallic Glass Powder

This chapter provides a brief summary of additional experiments, which were performed in the frame of this work. Powder consolidation by means of extrusion was the first technique used at the beginning of this project. Extrusion trials using partially crystalline Al-Ni-La powders did not yield satisfactory consolidation. The results of these trials are presented here. Moreover the result of one preliminary consolidation experiment using high speed sintering technique is given.

### 5.4.1 Extrusion of Al-Ni-La Metallic Glass Powder

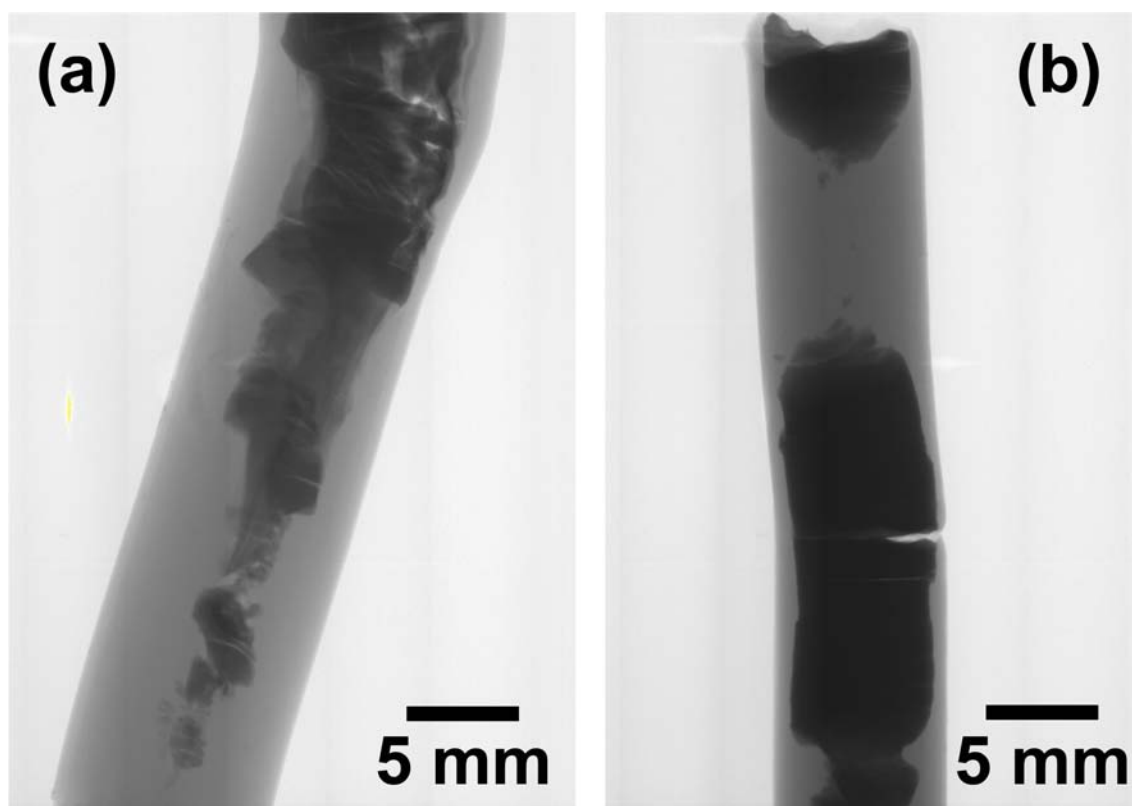


Figure 5.25: X-ray radiography images of helium-atomized  $Al_{87}Ni_8La_5$  alloy powder (batch I,  $d_{50} = 10 \mu m$ ) (a) after extrusion at  $300^\circ C$  applying a extrusion ratio of 1:4, and (b) after extrusion at  $270^\circ C$  applying a extrusion ratio of 1:11.

Figure 5.25(a) and (b) show X-ray radiography images of helium-atomized  $Al_{87}Ni_8La_5$  alloy powder (batch I) after extrusion at  $300^\circ C$  and  $270^\circ C$  applying an extrusion ratio of 1:4 and 1:11, respectively. Both X-ray radiography images illustrate heterogeneously distributed powders (darker contrast) inside the Al-can used (light gray contrast). Different gray scale colors and some white spots in the upper region in figure 5.25(a) indicate different attenuation of the X-rays.

XRD patterns (not shown here) of both samples exhibit Bragg reflections of fcc-Al,  $\text{Al}_3\text{Ni}$  and  $\text{Al}_{11}\text{La}_3$  phase.

#### 5.4.2 High Speed Sintering (HSS) of Al-Ni-La Metallic Glass Powder

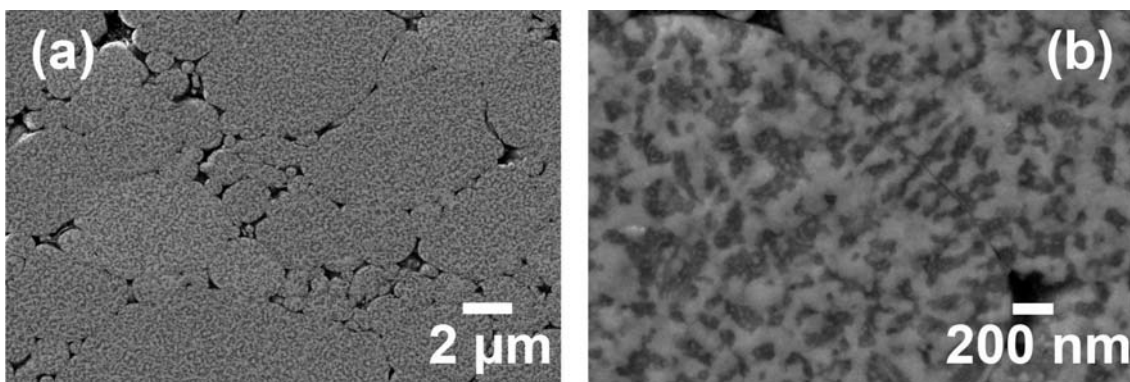


Figure 5.26: SEM-images at different magnifications of the longitudinal, cross-sectional area of helium-atomized  $\text{Al}_{85}\text{Ni}_{10}\text{La}_5$  alloy powder (batch I) after consolidation by high speed sintering at  $400^\circ\text{C}$ .

Figure 5.26 shows SEM-images at different magnifications of the longitudinal, cross-sectional area of helium-atomized  $\text{Al}_{85}\text{Ni}_{10}\text{La}_5$  alloy powder (batch I) after consolidation by high speed sintering at  $400^\circ\text{C}$ . The powder particles are not well integrated into a dense packed particle assembly. Big voids and pores occur among powder particles.

XRD patterns (not shown here) of the HSS sample show Bragg reflections of fcc-Al,  $\text{Al}_3\text{Ni}$  and  $\text{Al}_{11}\text{La}_3$  phase. Density and Vickers hardness are  $3.4\text{ g/cm}^3$  and  $165\pm 18\text{ HV}0.2$ , respectively.



# **Chapter 6**

## **Discussion**

## 6.1 Processing of Al-Ni-La Metallic Glass

The experimental results in chapter 4 show that amorphous Al-Ni-La powders can be successfully produced by means of gas-atomization. The NANOVAL process allows to produce batches of fully amorphous powders, which do not require further sieving to separate coarser crystalline powder particles from smaller amorphous particles. A successful synthesis of amorphous powders depends mainly on powder particle size, atomization gas, and GFA of the alloy. Following results are discussed assuming identical process conditions namely overheat and homogeneity of the melt, and gas pressure during atomization.

Higher cooling rates are expected in smaller powder particles, as described in chapter 2.3. Thus, smaller powder particles are either amorphous or contain a smaller volume-fraction of crystalline phases than bigger particles (Figures 4.12(b), 4.19(a)). The influence of the cooling rate on microstructure is illustrated in a continuous cooling transformation (CCT) diagram in figure 6.1. A higher cooling rate, as indicated by cooling curve (I), yields a smaller volume-fraction of crystalline phases than a lower cooling rate (II).

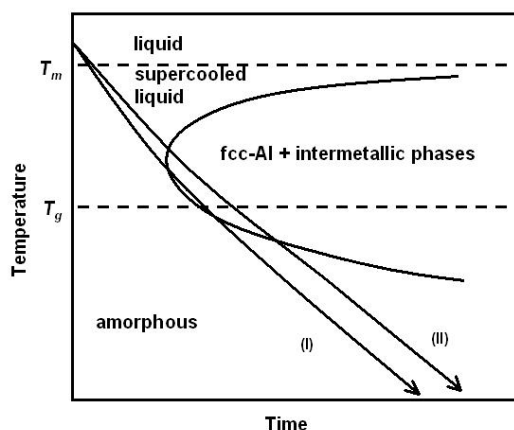


Figure 6.1: Schematic continuous cooling transformation (CCT) diagram of  $Al_{35}Ni_{10}La_5$  powder. The cooling curves (I) and (II) denote different cooling rates.

The influence of atomization gas on particle size is presented in tables 4.1 and 4.2. Comparing median diameters  $d_{50}$ , one reveals that helium-atomization yields smaller median particle diameters than argon-atomization. This is mainly due to the density of the atomization gas. According to [40] and [97], gases with lower densities ( $\rho_{helium} = 0.179 \text{ kg/m}^3$ ,  $\rho_{argon} = 1.784 \text{ kg/m}^3$  [120]) cause higher velocity differences between gas and melt jet, which leads to stronger shearing, thus finer powders.

Moreover, the atomization gas influences the heat transfer between melt droplet and gas stream, thus the cooling rate (see figure 4.21(a)). According to [40], [97], [98], a good heat transfer depends on heat conductivity of the atomization gas. Helium gas has a higher thermal conductivity ( $0.15 \text{ W/(mK)}$ ) compared to argon gas ( $0.018 \text{ W/(mK)}$ ), which permits a faster heat transfer from the surface of the melt droplet into the gas.

However, the influence of heat transfer on cooling rate is less dominant than the powder particle diameter [40]. Besides, the velocity difference between melt jet and gas stream affects the heat conductivity. Helium gas yields a higher velocity difference compared to argon gas, thus a higher heat transfer [42].

A formation of different crystalline phases in  $\text{Al}_{87}\text{Ni}_8\text{La}_5$  alloy and  $\text{Al}_{85}\text{Ni}_{10}\text{La}_5$  alloy during gas-atomization by different gases is illustrated figure 6.2. Both alloys show different phase boundaries in the CCT diagram. Helium gas achieves higher cooling rates at constant powder particle diameter compared to argon gas, which points to a better heat transfer. Helium-atomization (I) in figure 6.2(a) yields fully amorphous phase, whereas argon-atomization (II) yields coexisting amorphous, fcc-Al and intermetallic phases. Helium-atomization (I) in (b) leads to fcc-Al and amorphous phase, whereas argon-atomization leads to amorphous phase, fcc-Al and intermetallic phases.

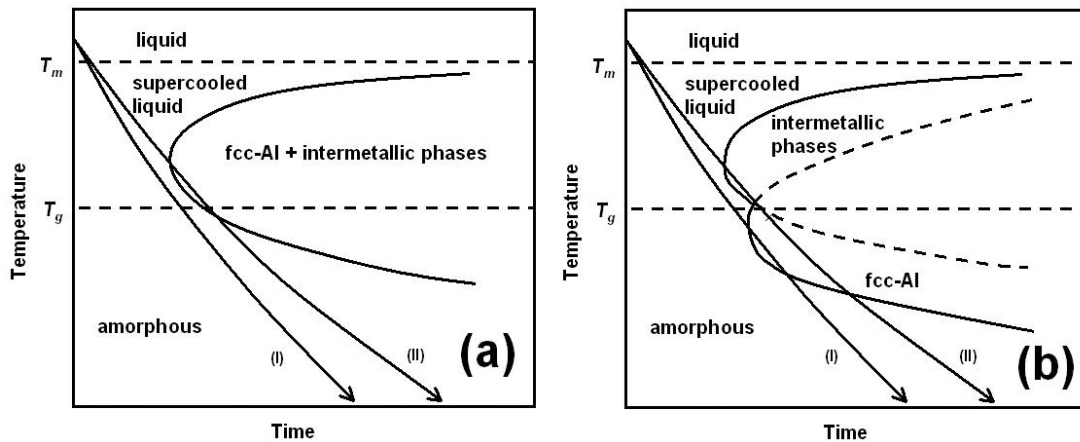


Figure 6.2: Schematic continuous cooling transformation (CCT) diagrams of (a) a one step crystallization and (b) a two step crystallization sequence in Al-Ni-La alloys. Cooling curves (I) and (II) denote helium- and argon-atomization, respectively.

The experimental results indicate that Al-Ni-La alloys with an alloying content  $\leq 13$  at-% cannot be produced fully amorphous by means of helium atomization (tables 4.1 and 4.2). One main reason is the GFA, which decreases with decreasing alloying content [61], [99]. The other reason is a limited cooling rate of the gas-atomization process. Cooling rates achieved by helium-atomization are sufficient for relative good Al-based glass formers such as  $\text{Al}_{85}\text{Ni}_{10}\text{La}_5$  and  $\text{Al}_{87}\text{Ni}_8\text{La}_5$  alloy. Melt spinning and splat quenching of the same alloys yielded also amorphous material, as shown in chapter 4.8.3 and [37]. These techniques can achieve higher cooling rates [16] as compared to gas atomization. They can be alternatively used for glass formation of Al-alloys with lower GFA.

However, highest quantities of fully amorphous powder were only obtained by helium-atomization of  $\text{Al}_{85}\text{Ni}_{10}\text{La}_5$ . Therefore, consolidation experiments were mainly performed using  $\text{Al}_{85}\text{Ni}_{10}\text{La}_5$  powder.

## 6.2 Crystallization of As-atomized Al-Ni-La Metallic Glass

### 6.2.1 As-quenched State of Al-Ni-La Metallic Glass

Helium-atomized  $\text{Al}_{85}\text{Ni}_{10}\text{La}_5$  powders, splats, and helium-atomized  $\text{Al}_{87}\text{Ni}_8\text{La}_5$  powders are amorphous for XRD and TEM. A certain volume of the amorphous phase reveals indications of a higher order, which is probably similar to fcc-Al crystalline structure. Moreover, amorphous  $\text{Al}_{85}\text{Ni}_{10}\text{La}_5$  powders contain quenched-in nuclei/ clusters. Single crystallites can develop in larger powder particles. However, the volume fraction of these crystallites is too low to be detectable for XRD.

Diffraction patterns of amorphous alloys show a broad diffuse scattering maximum and a shoulder. Their  $2\text{-}\Theta$  positions are in the vicinity to fcc-Al Bragg reflections, indicating that a certain volume of the amorphous structure has a higher order. Moreover, a prepeak points to a medium range order, which can correspond to a cluster structure constituted of unlike atoms [59], [62], [100]. Quenched-in clusters in Al-Ni-La alloys were also observed in [65]. Indications of the existence of quenched-in clusters/ nuclei are also given in DSC signals of as-quenched amorphous  $\text{Al}_{85}\text{Ni}_{10}\text{La}_5$  powders during isothermal heating (figure 4.5(a)). A monotonically decreasing exothermic heat, which occurs in the beginning of the annealing experiment can be interpreted as growth of quenched-in nuclei [89], [101], and as structural relaxation, as observed in  $\text{Al}_{85}\text{Ni}_5\text{Y}_6\text{Co}_2\text{Fe}_2$  [102]. This signal is not by machine transient as demonstrated by the uncorrected DSC-signal in figure 6.3. DSC investigations by [101] revealed also quenched-in nuclei in as-atomized  $\text{Al}_{85}\text{Ni}_{10}\text{La}_5$  powders. Many marginal glass formers such as Al-Sm, Al-Y-Fe and Al-Ni-Y-Co alloys show quenched-in nuclei [103], [104].

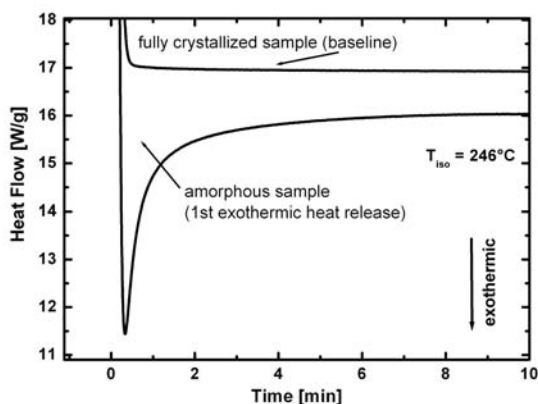


Figure 6.3: The non-corrected DSC curve of helium-atomized  $\text{Al}_{85}\text{Ni}_{10}\text{La}_5$  powder (batch I) obtained during isothermal at  $246^\circ\text{C}$  and the baseline.

Single dendrites were observed on single powder particles of  $\geq 20\ \mu\text{m}$ , which indicates a lower cooling rate due to a larger powder diameter. Since XRD of as-quenched

$\text{Al}_{85}\text{Ni}_{10}\text{La}_5$  powder does not show any indication of Bragg reflections, it can be assumed that the quantity of as-quenched crystalline phase is rather low compared to the amorphous phase.

## 6.2.2 Temperature-induced Crystallization

### $\text{Al}_{85}\text{Ni}_{10}\text{La}_5$ Alloy

Continuous and isothermal heating experiments of amorphous  $\text{Al}_{85}\text{Ni}_{10}\text{La}_5$  powder batch I and batch II yield comparable results (see chapters 4.1 and 4.2). Annealing can yield nanocrystalline structures of fcc-Al,  $\text{Al}_3\text{Ni}$  and  $\text{Al}_{11}\text{La}_3$  phase. Prior to crystallization, amorphous  $\text{Al}_{85}\text{Ni}_{10}\text{La}_5$  powders show a glass transition at about  $258^\circ\text{C}$  upon continuous heating at  $10^\circ\text{C}/\text{min}$ . At  $264^\circ\text{C}$ , a “simultaneous” crystallization of fcc-Al,  $\text{Al}_3\text{Ni}$  and  $\text{Al}_{11}\text{La}_3$  phases occurs within a narrow temperature range of approximately  $3^\circ\text{C}$ . This simultaneous crystallization can be observed for different cooling rates. During isothermal annealing, a primary crystallization of fcc-Al is indicated by XRD patterns of annealed powder samples but not by a DSC signal. DSC signals during further continuous heating between  $290$  and  $360^\circ\text{C}$  do not originate from the formation of new crystalline phases. They seem to be assigned to a growth process.

A similar crystallization sequence in  $\text{Al}_{85}\text{Ni}_{10}\text{La}_5$  powder was reported by [3], [61], and [101]. The differences of crystallization onset temperatures and peak shapes between literature data and data presented here is the result of slight differences in the composition. As observed by [101], a metastable crystalline phase occurs during isothermal annealing of helium-atomized  $\text{Al}_{85}\text{Ni}_{10}\text{La}_5$  powder. This was not observed in helium-atomized  $\text{Al}_{85}\text{Ni}_{10}\text{La}_5$  alloy powder presented in this work. But in-situ XRD studies during continuous and isothermal annealing of  $\text{Al}_{85}\text{Ni}_{10}\text{La}_5$  splats reveal that a metastable phase develops (chapter 4.8). Slight compositional changes in the vicinity of 5 at-% La in  $\text{Al}_{85}\text{Ni}_{10}\text{La}_5$  alloy cause the formation of a metastable phase. Quantitative analysis by ICP-MS shows a slightly higher La content (0.1 at-%) in  $\text{Al}_{85}\text{Ni}_{10}\text{La}_5$  splats compared to powders (table 4.2). The existence of the metastable phase depends strongly on composition. Various experimentalists in [68], [69], [105] have recently pointed out, that a metastable primitive cubic phase occurs, when the La content exceeds 5 at-%. A metastable phase does not exist for  $\text{Al}_{94-x}\text{Ni}_6\text{La}_x$  ( $x = 4-5$ ) alloys and  $\text{Al}_{92-x}\text{Ni}_8\text{La}_x$  ( $x = 4-5$ ) alloys. But it occurs in  $\text{Al}_{94-x}\text{Ni}_6\text{La}_x$  ( $x = 6-7$ ) alloys,  $\text{Al}_{92-x}\text{Ni}_8\text{La}_x$  ( $x = 6-7$ ) alloys, and  $\text{Al}_{87}\text{Ni}_7\text{La}_6$  alloy. These results suggest, that 5 at-% La is the critical value, at which metastable phase occurs.

Annealed powders can yield nanocrystalline structures. For example, continuous heating at  $20^\circ\text{C}/\text{min}$  of amorphous powder leads to spherical, homogeneously distributed nanocrystals of fcc-Al,  $\text{Al}_3\text{Ni}$  and  $\text{Al}_{11}\text{La}_3$  with a mean crystallite size of  $20 \pm 8$  nm. The nanocrystalline structure points to a nucleation-controlled crystallization process. This requires a high number density of nuclei [18], which can originate from as-quenched nuclei and thermally activated nucleation.

### **Al<sub>87</sub>Ni<sub>8</sub>La<sub>5</sub> alloy**

Amorphous Al<sub>87</sub>Ni<sub>8</sub>La<sub>5</sub> powder does not show a glass transition prior to crystallization (chapter 4.5). It reveals a two step crystallization sequence upon continuous heating. At 176°C, a primary crystallization of fcc-Al phase within the amorphous matrix occurs upon continuous heating at 20°C/min. At 337°C, the residual amorphous matrix decomposes and crystallizes into intermetallic phases Al<sub>3</sub>Ni and Al<sub>11</sub>La<sub>3</sub>. Fcc-Al crystallites grow only slightly during continuous heating up to 312°C. This observation coincides with an asymmetric DSC signal of the primary crystallization indicating an impeded growth of fcc-Al crystals after their formation. This can be explained by diffusion field impingement [106]: Solute Ni and La atoms are rejected from newly precipitated Al crystals forming Ni- and La-enriched regions around them. In order to continue growth, Al atoms have to migrate from the residual amorphous matrix to the Al crystals, since no further growth can occur via rejection of Ni and La atoms during crystallization. A long range diffusion of Al atoms is necessary, which requires time. Solute enriched regions around primary crystallized fcc-Al were observed in [67], [68], and recently verified by TAP [65]. During further heating, the residual amorphous matrix around Al crystals is continuously enriched by Ni and La atoms. When a concentration of intermetallic phases is achieved and the activation barrier for crystallization is exceeded, the residual amorphous matrix decomposes into Al<sub>3</sub>Ni and Al<sub>11</sub>La<sub>3</sub>.

### **Influence of the Ni-concentration on GFA**

Crystallization of Al<sub>87</sub>Ni<sub>8</sub>La<sub>5</sub> starts at lower temperatures and shows no glass transition compared to Al<sub>85</sub>Ni<sub>10</sub>La<sub>5</sub>. Thus, amorphous Al<sub>85</sub>Ni<sub>10</sub>La<sub>5</sub> is stable over a longer temperature range and has better GFA. Consequently, a higher Ni concentration stabilizes the amorphous phase upon heating because higher activation energies are required to induce crystallization, see tables 4.1 and 4.2. This can be explained in terms of glass topology. According to [59] and [62], Al-Ni-La metallic glasses consist of randomly distributed Al-Ni and Al-La solute-centred clusters (chapter 2.5). A higher Ni concentration leads to a higher amount of Al-Ni clusters compared to the amount of Al-La clusters. According to the dense cluster-packing model for metallic glasses [107], a higher amount of Al-Ni clusters in Al-(Ce,Y,La)-(Fe,Co,Cu,Ni) glasses can yield an enhanced packing efficiency of the glass. Denser packed clusters reflect a reduction of free energy, which is associated with a higher stability of the glass.

### **Crystallization upon Heating after Plastic Deformation**

Materials after plastic deformation by means of hot pressing, ECAP and HPT give similar DSC curves. No glass transition can be detected after HPT. Considering the free-volume theory, a plastically deformed metallic glass contains many shear bands. Within these bands, the free-volume has increased indicating a different glass structure as compared to the residual amorphous matrix. Each shear band represents a glass with different glass transition temperatures. Thus, a deformed metallic glass has many  $T_g$ , which in total lead to a smearing out of  $T_g$  of the as-quenched glass.

A decreasing first crystallization peak area upon continuous heating of samples consolidated below 250°C coincides with an increasing volume fraction of strain-induced fcc-Al. At the same time, the peak area of exothermic events, which develop during further continuous heating, increases. This coincides with the crystallization of intermetallic phases at higher temperatures, as shown by in-situ XRD plots. These results suggest that the first crystallization peak is mainly attributed to the crystallization of fcc-Al.

### 6.2.3 Strain-induced Crystallization of Al<sub>85</sub>Ni<sub>10</sub>La<sub>5</sub> Powders

Similar crystallization behaviors were observed after consolidation of amorphous Al<sub>85</sub>Ni<sub>10</sub>La<sub>5</sub> powders by means of hot pressing, ECAP and HPT (chapters 5.1, 5.2, and 5.3). All techniques involve plastic deformation at temperatures ranging from room temperature to 240°C leads to primary precipitation of fcc-Al within the amorphous matrix. This was observed neither during isothermal heating at temperatures below 240°C within 10 min nor during continuous heating. Therefore, this crystallization is strain-induced. The volume-fraction of strain-induced fcc-Al phase increases:

- with plastic deformation, as shown by HPT and ECAP (figures 5.22(a), 5.23, and 5.17)
- with temperature, as shown by ECAP and hot pressing (figures 5.4, 5.12).

#### Strain-induced Crystallization in the Light of a Free Energy Landscape

Plastic deformation, temperature and diffusivity are the main parameters which influence the strain-induced crystallization. According to the classical crystallization theory, the nucleation rate depends mainly on critical free energy  $\Delta G_c$  to start crystallization, activation energy  $Q$  for the transfer of a matrix-atom to an embryo (diffusion), and temperature. Formula 2.2 expresses that a decreasing  $\Delta G_c$  and  $Q$ , and an increasing temperature lead to higher nucleation rates, thus nanocrystalline structures. A model recently given in [108] has shown that uni-axial compression lowers  $\Delta G_c$  by several magnitudes, and  $Q$  only slightly. Severe plastic shear deformation as employed by means of ECAP and HPT seems to lower  $\Delta G_c$  even more. The increasing diffusion can be explained by increasing free volume during the formation of shear bands. Besides the influence of plastic deformation on activation energy, the system is permanently driven away from local equilibrium during deformation processing whilst the driving force for crystallization increases at the same time.

The change in crystallization behavior can be explained by means of a free energy landscape, where temperature and strain belong to different pathways towards different equilibrium states (“hierarchy of equilibrium states”). The different pathways of, (a) temperature induced crystallization and, (b) strain-induced crystallization and subsequently annealing are schematically illustrated in figure 6.4.

Starting from the local minimum of the as-quenched amorphous state: when only temperature increases (a), the amorphous system will first minimize the free energy towards

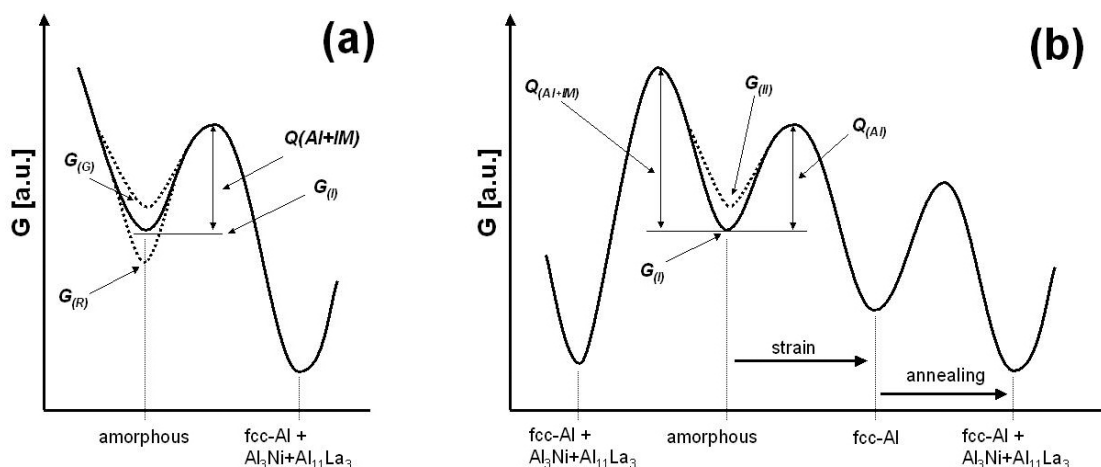


Figure 6.4: Schematic illustration of two crystallization pathways of  $Al_{85}Ni_{10}La_5$  powder in an energy landscape: a) denotes thermal treatment, and b) denotes straining and thermal treatment.

$G_{(R)}$  due to structural relaxation (exothermal). The driving force for this process is due to minimizing the entropy by slight reordering of the atoms, which is associated with minimizing free volume [109]. Consequently, the local minimum of the amorphous state will decrease with increasing temperature. However, the driving force for crystallization will increase at the same time. At the glass transition temperature, the energy minimum will largely increase when the heating rate is sufficiently high. In experiments presented here, the glass transition is assigned by an endothermic heat release during continuous heating of a not fully relaxed glass. The glass transition depends strongly on kinetics, thus the time-scale used to measure properties. It describes the acceleration of the relaxation process upon heating or deceleration upon cooling [110]. During glass transition, only small energies are required to pass the energy barrier  $Q_{Al+IM}$  for crystallization of fcc-Al and intermetallic phases.

In case the amount of plastic strain increases (b), the system is conveyed from the minimum of the as-quenched amorphous state  $G_{(I)}$  towards higher free energies  $G_{(II)}$  by permanent input of plastic strain energy into the system. During processing, some relaxation is possible and the energy can be stored by means of defects, e.g. by increasing the amount of free volume. This process depends strongly on the kinetics of the dynamic input [18], thus on the strain rate used.

If the static displacement of atoms during straining becomes large enough, the amorphous structure will be locally softened [111], [112]. Local softening can be due to rearrangements among nearest neighbor atoms by atomic motion via free volume sites [111], [112], or due to migration of atoms into nearest neighbor spaces [110]. In fact, local softening is associated with an increasing free volume, a decreasing viscosity, and an increasing diffusivity. Under these conditions, only small activation energies are required to lower the free energy of the system by crystallization of fcc-Al. Due to compositional and topological constraints (85 at-% Al, as-quenched nuclei of fcc-Al), crystallization of fcc-Al is facilitated, which is expressed by a smaller crystallization barrier  $Q_{Al}$  compared

to crystallization of intermetallic phases  $Q_{Al+IM}$ . Furthermore, crystallization of fcc-Al is a required step to form intermetallics, because enriched regions of solute atoms can be formed only after Al has crystallized. A strain-induced formation of intermetallic phases might occur if the residual, Ni- and La-enriched amorphous matrix reaches a certain concentration level.

Annealing of plastically deformed material can yield formation of intermetallic phases due to thermally activated atomic displacements. A complete crystallization is associated with a new equilibrium state.

### Strain-induced Crystallization in the Light of Shear Band Formation

Various scientists argue that the underlying mechanism for strain-induced crystallization is an athermal process. This means that the crystallization is not caused by thermally activated atomic jumps. It is rather a result of static atom displacements, which can yield shear bands<sup>1</sup>. In the following, it will be argued that strain-induced crystallization is possibly an athermal process based on evidence from the literature.

Strain-induced fcc-Al precipitation after HPT in amorphous  $Al_{85}Ce_8Ni_5Co_2$  was observed by [73]. Continuous heating of melt-spun amorphous  $Al_{85}Ce_8Ni_5Co_2$  alloy exhibits a simultaneous crystallization of fcc-Al and intermetallic phases, which is similar to the crystallization sequence of  $Al_{85}Ni_{10}La_5$  powder. After subjecting amorphous  $Al_{85}Ce_8Ni_5Co_2$  melt-spun ribbons to HPT at room temperature (5 whole turns, 6 GPa uniaxial pressure), only fcc-Al phase precipitates within the amorphous matrix. Its amount increases by increasing plastic shear straining along the disc radius.

It was reported in [1] that strain-induced nanocrystallization of fcc-Al in melt-spun  $Al_{90}Fe_5Gd_5$ ,  $Al_{90}Fe_5Ce_5$  and  $Al_{87}Ni_{8.7}Y_{4.3}$  alloys occurs in shear bands after bending and after ball milling at room temperature. Contrary to these alloys, amorphous  $Al_{85}Ni_{10}Ce_5$  melt-spun ribbons remained amorphous after bending and ball milling. The authors proposed that a temperature rise in shear bands cannot be the nature of strain-induced nanocrystallization. They estimated that adiabatic heating within the shear bands leads to a temperature increase of  $> 400\text{ K} \geq 2500\text{ K}$ , what is high enough to induce crystallization. But since this heat seems to be fast conducted away, the authors considered a model, which explains strain-induced crystallization as the result of strain-assisted atomic rearrangements of Al atoms towards more stable positions forming Al nanocrystals. Once a stable nuclei is formed, further growth is thermodynamically favorable. Moreover, strain-induced crystallization strongly depends on the topological and chemical order of the amorphous phase, thus it depends on the alloy composition. This might be the reason that  $Al_{85}Ni_{10}Ce_5$  alloy remained amorphous after plastic deformation compared to the other alloys. Similar observations were reported in [4], where melt-spun  $Al_{85}Ni_{10}Ce_5$  ribbons remained amorphous after cold rolling. The author's revealed that strain-induced crystallization occurs only if the metallic glass contains pre-existing nuclei or crystals.

Experimental evidence of so-called thermal spikes in shear bands has been recently

<sup>1</sup>Also crystalline materials can form shear bands. Shear bands are in the following exclusively related to metallic glasses.

given in [113]. They observed a rapid localized temperature rise developing in shear bands during deformation, which yield estimated temperatures of more than 1000 K lasting a few nanoseconds. However, the estimated local heat generated was considered to be fast conducted away from the shear bands to its environment within a nanosecond timescale.

Bending experiments on amorphous  $\text{Al}_{90}\text{Fe}_5\text{Gd}_5$  melt-spun ribbons performed at room temperature and at  $-40^\circ\text{C}$  revealed that strain-induced fcc-Al nanocrystals develop in shear bands in the compressive but not in the tensile region of the ribbons [5], [114]. It has been expected that similar adiabatic heating occurred in both regions. Therefore, a temperature rise cannot be the reason for nanocrystallization in shear bands. Investigations in [7], [72], and [115] revealed that crystals formed in shear bands do not exceed the shear band width. Maximum crystal sizes do not exceed 18 nm after cold rolling (CR) [72] and HPT [7], although CR and HPT involve different amounts of severe plastic deformation. Furthermore, crystals formed in shear bands can be elongated along the shear band axis and they can contain dislocations. These results indicate that strain-induced crystallization is an athermal process. If a temperature rise would induce crystallization in shear bands, it should not be limited to the shear band width. It was suggested in [115] that the reason for constant crystal size is based on a dislocation mediated fragmentation during deformation.

Strain-induced crystallization can be associated with enhanced diffusion in active shear bands. Based on various experiments [116], and theoretical models given in [111], [112], it is commonly agreed that inhomogeneous plastic deformation at temperatures below  $T_g$  is localized in narrow shear bands. A drop of viscosity inside the bands is the result of flow dilatation, which yields an increase of free volume. This leads to local shear softening of the glass. Due to the increased free volume in shear bands, a higher mobility of atoms can be expected, which permits long-range diffusion without substantial increase of the global temperature. The shear bands can be produced by compression or tension. Experimental evidence for enhanced diffusion by flow dilatation was given in [117]. The scientists were able to examine separately the effect of temperature- and strain-assisted plastic flow on amorphization during cold rolling of a bulk diffusion couple using Zr and Ni. Their results reveal that strain-assisted plastic flow plays a significant role enhancing the interdiffusion coefficient by several orders of magnitude.

However, strain-induced crystallization is not limited to shear bands only. TEM-observation in [72] revealed that strain-induced fcc-Al nanocrystals were homogeneously distributed within the residual amorphous matrix after cold rolling of amorphous  $\text{Al}_{88}\text{Y}_7\text{Fe}_5$  melt-spun ribbons. The nanocrystals were found in shear bands but also within the residual amorphous matrix. This was also observed after HPT of  $\text{Al}_{88}\text{Y}_7\text{Fe}_5$  by [7]. The formation of fcc-Al nanocrystals outside shear bands can be explained by atomic bond rearrangements. Based on molecular dynamics simulations by [118], structural changes of metallic glasses upon pressure are discussed by means of Bond Orientational Order (BOO) and Bond Orientational Anisotropy (BOA). The order parameter defines the topology of atomic bonds at constant bond number. Elastic and plastic deformation changes bond rearrangements, mostly by bond exchanges. Under static stress, the bond exchange results in the bond orientational anisotropy. Nanocrystal formation might undergo a BOA towards a long range BOO, which occurs in crystalline materials.

## 6.2.4 Density Changes during Crystallization

The mass density of amorphous  $\text{Al}_{85}\text{Ni}_{10}\text{La}_5$  increases 1.4-1.7% during the phase transformation from the amorphous to the crystalline state. This result is similar to the contraction observed in other metallic glasses upon crystallization, which is by about 1-2% [119]. The volume contraction during crystallization is due to rearrangements of disordered atoms towards a higher ordered state with higher packing efficiency. A higher packing efficiency is associated with minimization of entropy and thus free energy.

Simultaneous in-situ X-ray attenuation and in-situ X-ray diffraction measurements on amorphous  $\text{Al}_{85}\text{Ni}_{10}\text{La}_5$  splats (chapter 4.8) revealed two mass density increases upon continuous heating within a narrow temperature range corresponding to two phase transformations. During the first crystallization step, amorphous  $\rightarrow$  fcc-Al + metastable bcc-phase, the mass density increases by about 0.9-1.1%. The second crystallization step, fcc-Al + metastable bcc-phase  $\rightarrow$  fcc-Al,  $\text{Al}_3\text{Ni}$  and  $\text{Al}_{11}\text{La}_3$ , is associated with a density increase by about 0.5-0.6%. During isothermal annealing, the density increases by about 0.8% corresponding to the first crystallization step. The slightly smaller mass density change compared to continuous heating can originate from structural relaxation of the glass within 20 min isothermal annealing prior to the onset of crystallization. Structural relaxation was also observed during cyclic continuous heating. According to [119], the volume contraction due to structural relaxation is  $\leq 0.5\%$ .

During continuous heating between 300 and 400°C, the Bragg reflections shift by about 0.1%. This coincides with the thermal expansion coefficient of  $1.1 \times 10^{-5}$  1/K extracted from X-ray attenuation data yielding a relative expansion of 0.1%. The thermal expansion is a consequence of thermally induced harmonic oscillations (Debye theory). In a perfect monoatomic crystal, the thermal displacement increases continuously with temperature [110]. This leads to dilatation of interatomic spacings (volume expansion) as indicated by smaller  $2\Theta$  angles according to Bragg's formula. The thermal expansion coefficients of amorphous and fully crystalline  $\text{Al}_{85}\text{Ni}_{10}\text{La}_5$  splats ranges between 1.1 and  $2.7 \times 10^{-5}$  1/K, which is in the range of pure crystalline fcc-Al ( $2.3 \times 10^{-5}$  1/K [120]).

## 6.3 Consolidation of Al-Ni-La Metallic Glass Powder

Consolidation by hot pressing, SPS<sup>2</sup>, ECAP, and HPT of Al-Ni-La powder yield similar results regarding sample density and Vickers hardness. The here presented results reveal that processing temperature, processing time, and amount of plastic deformation are the main process parameters governing the consolidation process. Hot pressing and SPS yielded full consolidated samples, whereas ECAP and HPT yielded only partially consolidated samples.

<sup>2</sup>The results of SPS consolidation are presented in [9], [10].

### Influence of the Processing Temperature and Processing Time on Consolidation

Density and Vickers hardness increase with processing temperature and processing time yielding a maximum density and hardness of approximately:

- 3.5 g/cm<sup>3</sup> and 460 HV0.2, respectively, for Al<sub>85</sub>Ni<sub>10</sub>La<sub>5</sub> alloy, and
- 3.3 g/cm<sup>3</sup> and 350 HV0.2, respectively (figure 5.7), for Al<sub>87</sub>Ni<sub>8</sub>La<sub>5</sub> alloy.

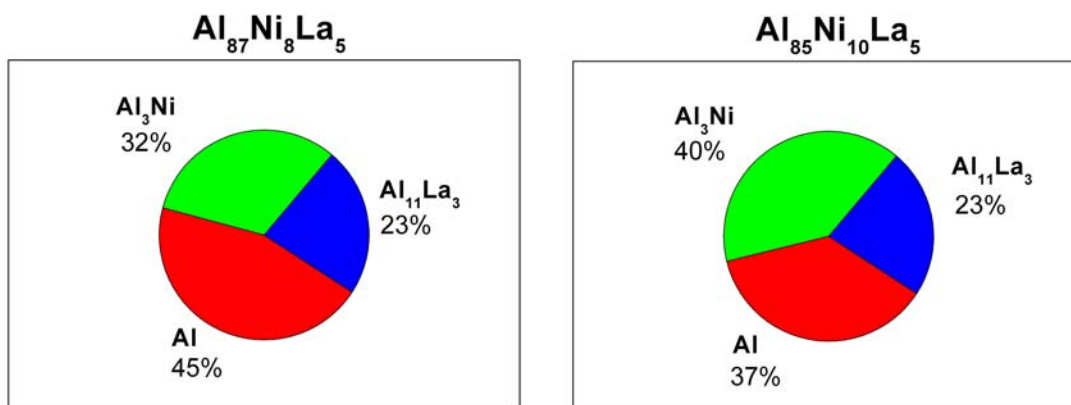


Figure 6.5: The fractions of equilibrium phases in Al<sub>87</sub>Ni<sub>8</sub>La<sub>5</sub> and Al<sub>85</sub>Ni<sub>10</sub>La<sub>5</sub> alloy calculated from the stoichiometric phase compositions.

Smaller density and hardness values of consolidated Al<sub>87</sub>Ni<sub>8</sub>La<sub>5</sub> powder compared to Al<sub>85</sub>Ni<sub>10</sub>La<sub>5</sub> coincides with a smaller volume-fraction of intermetallic phases, as illustrated in figure 6.5.

XRD patterns of consolidated Al<sub>85</sub>Ni<sub>10</sub>La<sub>5</sub> samples reveal that the maximum density and hardness is due to partially or fully crystallization. Figure 6.6 shows that hardness increases with density. Furthermore, the hardness increases significantly with increasing amount of fcc-Al phase within the amorphous matrix due to precipitation strengthening (figures 5.4 and 5.12). ECAP processing at temperatures above 250°C involves a decreasing hardness by about 15% which is associated with fully crystallization and thus formation of intermetallic phases. This is different to hot pressed and SPS processed samples, which show highest density and hardness in fully crystallized samples. Neither a significant density nor hardness drop is detected after consolidation above 250°C. This is a contradiction to observations in [68] and [69], where a drop of hardness occurred after formation of intermetallic phases. Their annealing experiments using melt-spun Al<sub>92-x</sub>Ni<sub>8</sub>La<sub>x</sub> (x = 4-7) and Al<sub>94-x</sub>Ni<sub>6</sub>La<sub>x</sub> (x = 4-7) alloys revealed that the Vickers hardness increases with increasing amount of primary crystallized fcc-Al phase within the residual amorphous matrix. After full crystallization, the hardness decreases when intermetallic phases form. In addition to the influence of processing temperature on consolidation behavior, the processing time also affects the consolidation process. Hot pressing using longer dwelling times was assisted by slow plastic flow, which rendered denser and harder samples. This indicates that a small strain-rate can help to deform hard materials.

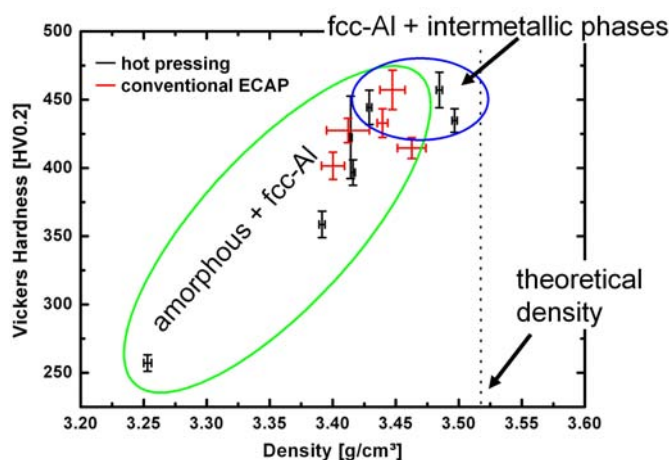


Figure 6.6: Density-hardness correlation of hot pressed and ECAP processed  $Al_{85}Ni_{10}La_5$  powders.

Consolidation at room temperature using pressing, extrusion<sup>3</sup> and ECAP was not feasible. Only HPT processing yielded consolidated samples with a maximum density (figure 5.19) similar to that of hot pressed and ECAP samples processed at elevated temperatures. This was obtained by use of large amounts of plastic shear deformation during HPT.

### Influence of Plastic Deformation on Consolidation

An increasing plastic shear deformation leads to denser samples, as shown in ECAP and HPT (figures 5.17 and 5.21). A sandwich structure occurs in the fracture surface of disc D360, which indicates differently consolidated regions. Vein patterns in the top and bottom layer. Generally, vein patterns are observed on fracture surfaces after failure of brittle metallic glasses below  $T_g$  [116]. Considering vein patterns as being significant for fracture surfaces of bulk metallic glasses, the vein patterns containing layers can be regarded as layers of fully consolidated powders. In this context, consolidation means that the powder particles are merged to pore-free bulky layers. This pore-free consolidation requires a certain degree of plastic shear deformation, as presented by HPT samples processed at different amounts of torsion. In order to achieve completely merged HPT samples, larger degrees of torsion are required. In case of HPT on amorphous Al powder reported in [7] and [14], 5 full turns of the anvils render full consolidation.

Hot pressed and ECAP samples always show powder features similar to HPT discs processed up to  $45^\circ$  torsion. The powders are well integrated into "closed packed" particle assemblies. The amount of plastic deformation was obviously not large enough to merge powder particles. A merger of powder particles can be obstructed by surface oxide layers, which cannot be avoided by conventional technical measures. Figure 4.21(b) shows that oxygen is present in gas-atomized powders used. The oxygen content decreases with powder particle diameter indicating that oxygen is associated with the particle surface.

<sup>3</sup>Consolidation by means of extrusion was not feasible even at elevated temperatures, as shown in figure 5.25. Harder partially crystallized powder used as precursor impeded the extrusion process.

In general, hot pressing and SPS yielded full consolidation through the whole sample compared to extrusion, ECAP, and HPT, which developed large macroscopic cracks. The cracks appeared in ECAP samples due to a material flow gradient in the exit channel, as indicated by the copper-container front in figure 5.9. A faster flow along the bottom side of the exit channel has mainly two reasons: the difference in ductility between soft Cu container material and hard  $\text{Al}_{85}\text{Ni}_{10}\text{La}_5$  powders, and the formation of a dead zone in the ECAP die corner yielding a wide curvature  $\psi$  [121]. The development of cracks in the exit channel coincides with irregular load and ram speed drops during processing near the end of the ECAP process. The material flow gradient and thus crack formation can be reduced or avoided using a second plunger in the exit channel. The second plunger presses with a minor load against the propagating sample inducing a so-called “back pressure”, which leads to a plane propagation front of the sample perpendicular to the pressing direction. It has been observed that back pressure ECAP of pure Al powder yields pore- and crack-free samples [122], [123].

The use of the conventional ECAP die leads to a smaller amount of macroscopic cracks compared to the zic-zac ECAP die. Shear strain applied in opposite directions by means of zic-zac ECAP does not improve macroscopic properties concerning density, hardness and crack formation. This corresponds to observations in [12] and [124].

## **Chapter 7**

### **Summary and Conclusions**

A wide range of investigations were carried out to evaluate the processing, crystallization and consolidation behavior of Al-Ni-La metallic glasses.

### Processing of Al-Ni-La Alloy

Gas atomization of  $\text{Al}_{85}\text{Ni}_{10}\text{La}_5$  and  $\text{Al}_{87}\text{Ni}_8\text{La}_5$  using the NANOVAL process can yield fully amorphous powders, which do not require further sieving. Helium gas yields smaller powders than argon gas, which is associated with a higher cooling rate. Fully amorphous powder batches have median particle size diameters of  $\leq 14 \mu\text{m}$ . Moreover, helium gas enhances rapid quenching due to its higher thermal conductivity compared to argon. Splat quenching and melt spinning of  $\text{Al}_{85}\text{Ni}_{10}\text{La}_5$  and  $\text{Al}_{87}\text{Ni}_8\text{La}_5$  alloys can also yield fully amorphous material.

### Crystallization Behavior of Al-Ni-La Metallic Glass

Gas-atomized amorphous  $\text{Al}_{85}\text{Ni}_{10}\text{La}_5$  powders contain quenched-in nuclei as indicated by XRD and DSC. The alloy shows a glass transition prior to crystallization. The crystallization sequence of  $\text{Al}_{85}\text{Ni}_{10}\text{La}_5$  alloy changes upon heating and upon straining:

- Continuous heating of amorphous  $\text{Al}_{85}\text{Ni}_{10}\text{La}_5$  powders shows a crystallization of fcc-Al,  $\text{Al}_3\text{Ni}$ , and  $\text{Al}_{11}\text{La}_3$  within a small temperature range (about  $3^\circ\text{C}$  at  $10^\circ\text{C}/\text{min}$ ): amorphous phase  $\rightarrow$  fcc-Al +  $\text{Al}_3\text{Ni}$  +  $\text{Al}_{11}\text{La}_3$ .
- Isothermal heating at  $246^\circ\text{C}$  of amorphous  $\text{Al}_{85}\text{Ni}_{10}\text{La}_5$  powders shows that fcc-Al phase occurs in a short time range prior to intermetallic phases.
- Continuous and isothermal heating of amorphous  $\text{Al}_{85}\text{Ni}_{10}\text{La}_5$  splats reveal a two step crystallization sequence: amorphous phase  $\rightarrow$  fcc-Al + metastable bcc-phase  $\rightarrow$  fcc-Al +  $\text{Al}_3\text{Ni}$  +  $\text{Al}_{11}\text{La}_3$ . The formation of the metastable phase is probably attributed to a slightly higher La-content  $> 5$  at-%.
- Plastic deformation of amorphous  $\text{Al}_{85}\text{Ni}_{10}\text{La}_5$  powders at temperatures between room temperature and  $250^\circ\text{C}/\text{min}$  leads to primary crystallization of strain-induced fcc-Al phase: amorphous phase  $\rightarrow$  fcc-Al + residual amorphous phase. The volume fraction of strain-induced fcc-Al increases with plastic deformation and temperature. The results are discussed in the light of thermodynamics and shear band formation.

The mass density of amorphous  $\text{Al}_{85}\text{Ni}_{10}\text{La}_5$  increases by about 1.4-1.7% during crystallization. The thermal expansion coefficient of  $\text{Al}_{85}\text{Ni}_{10}\text{La}_5$  alloy ranges between 1.1 and  $2.7 \times 10^{-5}$  1/K.

The crystallization sequence of  $\text{Al}_{87}\text{Ni}_8\text{La}_5$  alloy upon continuous heating shows a two-step crystallization sequence: amorphous phase  $\rightarrow$  fcc-Al  $\rightarrow$   $\text{Al}_3\text{Ni}$  +  $\text{Al}_{11}\text{La}_3$ . It shows no glass transition prior to crystallization. A higher Ni-content leads to shift of the onset for primary crystallization of fcc-Al towards higher temperatures.

---

## **Consolidation of Al-Ni-La powders**

The consolidation behavior of Al-Ni-La powders depends on process temperature, the amount of plastic deformation, processing time and alloy composition. An increasing processing temperature leads to an increasing density and Vickers hardness due to partially crystallization at temperatures below 250°C. Hot pressing, SPS and ECAP samples of Al<sub>85</sub>Ni<sub>10</sub>La<sub>5</sub> powder show similar maximum densities and Vickers hardness of approximately 3.5 g/cm<sup>3</sup> and 460 HV0.2, respectively. The hardness drops in fully crystallized ECAP samples but not in hot pressed and SPS samples. Consolidation at room temperature can be achieved by HPT only due to large amounts of plastic shear deformation. A higher shear strain leads to larger consolidated regions. However, HPT and ECAP consolidation leads to only partially consolidated sample regions, whereas hot pressing and SPS can provide full consolidated samples.



# References

- [1] H. CHEN, Y. HE, G.J. SHIFLET, S.J. POON *Deformation-induced nanocrystal formation in shear band of amorphous alloys*, Nature **367** (1994) pp.541-543.
- [2] Y. KAWAMURA, H. MANO, A. INOUE *Nanocrystalline aluminum bulk alloys with high strength of 1420 MPa produced by the consolidation of amorphous powders*, Scripta Materialia **44** (2001) pp.1599-1604.
- [3] A.P. TSAI, T. KAMIYAMA, Y. KAWAMURA, A. INOUE, T. MASUMOTO *Formation and precipitation mechanism of nanoscale Al particles in Al-Ni based amorphous alloys*, Acta Materialia **45** (1997) pp.1477-1487.
- [4] J.H. PEREPEZKO, R.J. HEBERT, R.I. WU *Nanostructure synthesis and amorphization during cold rolling*, Materials Science Forum **386-388** (2002) pp.11-20.
- [5] W.H. JIANG, F.E. PINKERTON, M. ATZMON *Deformation-induced nanocrystallization in an Al-based amorphous alloy at a subambient temperature*, Scripta Materialia **48** (2003) pp.1195-1200.
- [6] J.-J. KIM, Y. CHOI, S. SURESH, A.S. ARGON *Nanocrystallization during nanoindentation of a bulk amorphous metal alloy at room temperature*, Science **295** (2002) pp.654-657.
- [7] N. BOUCHARAT, R. HEBERT, H. RÖSNER, R. VALIEV, G. WILDE *Nanocrystallization of amorphous  $Al_{88}Y_7Fe_5$  alloy induced by plastic deformation*, Scripta Materialia **53** (2005) pp.823-827.
- [8] P.P. CHOI, J.S. KIM, O.T.H. NGUYEN, D.H. KWON, Y.S. KWON, J.C. KIM *Al-La-Ni-Fe bulk metallic glasses produced by mechanical alloying and spark-plasma sintering*, Material Science Engineering A **449-451** (2007) pp.1119-1122.
- [9] T.T. SASAKIA, J. VIERKE, M. WOLLGARTEN, J. BANHART AND K. HONO *Bulk nanocrystalline  $Al_{85}Ni_{10}La_5$  alloy fabricated by spark plasma sintering of atomized powders*, Material Science Engineering A (2008) article in press.
- [10] S. SCUDINO, K.B. SURREDDI, K. NIKOLOWSKI, M. STOICA, M. SAKALIYSKA, H.V. NGUYEN, J.S. KIM, J. VIERKE, M. WOLLGARTEN, J. ECKERT *Bulk nanocrystalline  $Al_{87}Ni_8La_5$  alloy with high strength and good ductility produced by spark plasma sintering of gas atomized powders*, manuscript submitted (2008).

## REFERENCES

---

- [11] A. INOUE, H. KIMURA *Fabrications and mechanical properties of bulk amorphous, nanocrystalline, nanoquasicrystalline alloys in aluminum-based system*, Journal of Light Metals **1** (2001) pp.31-41.
- [12] O.N. SENKOV, D.B. MIRACLE, J.M. SCOTT, S.V. SENKOVA *Equal channel angular extrusion compaction of semi-amorphous Al<sub>85</sub>Ni<sub>10</sub>Y<sub>2.5</sub>La<sub>2.5</sub> alloy powder*, Journal of Alloys and Compounds **365** (2004) pp.126-133.
- [13] R.Z. VALIEV, R.K. ISLAMGALIEV, I.V. ALEXANDROV *Bulk nanostructured materials from severe plastic deformation*, Progress in Materials Science **45** (2000) pp.103-189.
- [14] W.J. BOTTA FILHO, J.B. FOGAGNOLO, C.A.D. RODRIGUES, C.S. KIMINAMI, C. BOLFARINI, A.R. YAVARI *Consolidation of partially amorphous aluminum-alloy powders by severe plastic deformation*, Materials Science and Engineering A **375-377** (2004) pp.936-941.
- [15] Meriam-Websters Online Dictionary, <http://www.m-w.com/dictionary>
- [16] H.A. DAVIES *Metallic glass formation* from F.E. LUBORSKY (ED.) *Amorphous metallic alloys*, Butterworth & Co Ltd London (1983) pp.8-25.
- [17] G. WILDE, N. BOUCHARAT, R.J. HEBERT, H. RÖSNER, W.S. TONG, J.H. PEREPEZKO *Nanocrystallization in Al-rich metallic glasses*, Advanced Engineering Materials **5** (2003) pp.125-130.
- [18] J.H. PEREPEZKO *Nucleation-controlled reactions and metastable structures*, Progress in Materials Science **49** (2004) pp.263-284.
- [19] J.W. CAHN *Obtaining inferences about relative stability and metastable phase sequences from phase diagrams*, Bulletin of Alloy Phase Diagrams **1** (1980) pp.27-32.
- [20] R. BUSCH, J. SCHROERS, W.H. WANG *Thermodynamics and kinetics of bulk metallic glasses*, MRS Bulletin **32** (2007) pp.620-623.
- [21] W. KLEMENT, R.H. WILLENS, P. DUWEZ *Non-crystalline structure in solidified gold-silicon alloys*, Nature **187** (1960) pp.869-870.
- [22] A. INOUE, N. NISHIYAMA *Extremely high cooling rates of new Pd-Cu-P based amorphous alloys*, Materials Science Engineering A **226-228** (1997) pp.401-405.
- [23] T.A. WANIUK, J. SCHROERS, W.L. JOHNSON *Critical cooling rate and thermal stability of Zr-Ti-Cu-Ni-Be alloys*, Applied Physics Letters **78** (2001) pp.1213-1215.
- [24] A. INOUE *Stabilization of metallic supercooled liquid and bulk amorphous alloys*, Acta Materialia **48** (2000) pp.279-306.
- [25] H. MA, L.L. SHI, J. XU, Y. LI, E. MA *Discovering inch-diameter metallic glasses in three dimensional composition*, Applied Physics Letters **87** (2005) pp.1819-15.

- [26] Q.K. JIANG, G.Q. ZHANG, L. YANG, X.D. WANG, K. SAKSL, H. FRANZ, R. WUNDERLICH, H. FECHT, J.Z. JIANG *La-based bulk metallic glasses with critical diameter up to 30 mm*, *Acta Materialia* **55** (2007) pp.4409-4418.
- [27] M.H. COHEN, D. TURNBULL *Composition requirements for glass formation in metallic and ionic systems*, *Nature* **189** (1961) pp.131-132.
- [28] D. TURNBULL *Under what conditions can a glass be formed?*, *Contemporary Physics* **10** (1969) pp.473-488.
- [29] A. INOUE *Bulk amorphous alloys*, *Trans Tech Publications Zürich* **4** (1998).
- [30] S. MECHLER *Die Rolle der Ikosaedrischen Nahordnung bei Glassbildung und Kristallisation im System Zr-Ti-Ni-Cu-Be*, dissertation thesis, Berlin University of Technology (2007).
- [31] M.G. SCOTT *Crystallization* from F.E. LUBORSKY (ED.) *Amorphous metallic alloys*, Butterworth & Co Ltd London (1983) pp.144-168.
- [32] J.W. CHRISTIAN *The theory of transformations in metals and alloys*, Pergamon 3rd ed. (2002).
- [33] G.W. SCHERRER *Glass formation and relaxation* from J. ZARZYCKI (ED.) *Materials science and technology - glasses and amorphous materials*, VCH Weinheim **9** (1991) pp.119-174.
- [34] T.E. QUESTED, A.L. GREER *Athermal heterogeneous nucleation of solidification*, *Acta Materialia* **53** (2005) pp.2683-2692.
- [35] J.F. SHACKELFORD *Introduction to materials science for engineers*, Prentice Hall International Inc. 4ed. (1998).
- [36] U. KÖSTER, U. HEROLD *Crystallization of metallic glasses* from H.J. GÜNDTERODT, H. BECK (ED.) *Glassy Metals*, Springer Berlin (1981) pp.225-259.
- [37] S. GOERGEN *Herstellung und Charakterisierung von Gläsern auf Basis von Aluminium*, students project (Studienarbeit), Hahn-Meitner-Institute Berlin, Berlin University of Technology (2006).
- [38] J.J.DUNKLEY *Atomization*, *ASM Handbook* **7** (1998) pp.35-52.
- [39] A. ÜNAL, D.D. LEON, T.B. GURGANUS, G.J. HILDEMAN *Production of aluminum and aluminum-alloy powder*, *ASM Handbook* **7** (1998) pp.148-159.
- [40] L. GERKING *Powder from metal and ceramic melts by laminar gas streams at supersonic speeds*, *Powder Metallurgy International* **25** (1993) pp.59-65.
- [41] H.H. LIEBERMANN *Sample preparation: methods and process characterization* from F.E. LUBORSKY (ED.) *Amorphous metallic alloys*, Butterworth & Co Ltd London (1983) pp.26-39.

## REFERENCES

---

- [42] A. NYLUND *Surface reactions during atomization, handling and consolidation of Al-powders*, Dissertation thesis, Chalmers Tekniska Högskola Göteborg (1993).
- [43] X.H. LIN, W.L. JOHNSON *Formation of Ti-Zr-Cu-Ni bulk metallic glass*, Journal of Applied Physics **11** (1995) pp.6514-6519.
- [44] H. GLEITER *Nanocrystalline materials*, Progress in Materials Science **33** (1989) pp.223-315.
- [45] R. VALIEV *Nanostructuring of metals by severe plastic deformation of advanced properties*, Nature Materials **3** (2004) pp.511-516.
- [46] G. WILDE *Nanostructures and nanocrystalline composite materials - synthesis, stability and phase transformations*, Surface and Interface Analysis **38** (2006) 1047-1062.
- [47] C.C. KOCH *Structural nanocrystalline materials: an overview*, Journal of Materials Science **42** (2007) pp.1403-1414.
- [48] Y. WANG, M. CHEN, F. ZHOU, E. MA *High tensile ductility in a nanostructured metal*, Nature **419** (2002) pp.912-914.
- [49] R.Z. VALIEV, I.V. ALEXANDROV, Y.T. ZHU, T.C. LOWE *Paradox of strength and ductility in metals processed by severe plastic deformation*, Journal of Materials Research **17** (2002) pp.5-8.
- [50] M. BALOG *Ultrafine grained Al profiles with high temperature stability*, dissertation thesis, Slovak Academy of Sciences (2007).
- [51] H.A. KUHN *Forging and hot pressing*, ASM Handbook **7** (1998) pp.632-637.
- [52] W. SCHATT *Sintervorgänge - Grundlagen*, VDI-Verlag, Düsseldorf (1992).
- [53] Z.A. MUNIR, U. ANSELMINI-TAMBURINI, M. OHYANAGI *The effect of electric field and pressure on the synthesis and consolidation of materials: A review of the spark plasma sintering method*, Journal of Materials Science **41** (2006) pp.763-777.
- [54] B.L. FERGUSON *Extrusion of metal powders*, ASM Handbook **7** (1998) pp.621-631.
- [55] R.Z. VALIEV, T.G. LANGDON *Principles of equal-channel angular pressing as a processing tool for grain refinement*, Progress in Materials Science **51** (2006) pp.881-981.
- [56] G.J. RAAB, R.Z. VALIEV, T.C. LOWE, Y.T. ZHU *Continuous processing of ultra-fine grained Al by ECAPConform*, Materials Science and Engineering A **382** (2004) pp.30-34.
- [57] Y. IWAHASHI, J. WANG, Z. HORITA, M. NEMOTO, T.G. LANGDON *Principle of equal-channel angular pressing for the processing of ultrafine grained materials*, Scripta Materialia **35** (1996) pp.143-146.

- [58] I.V. ALEXANDROV, Y.T. ZHU, T.C. LOWE, R.K. ISLAMGALIEV, R.Z. VALIEV *Consolidation of nanometer sized powders using severe plastic torsional straining*, Nanostructured materials **10** (1998) pp.45-54.
- [59] A. INOUE *Amorphous, nanoquasicrystalline and nanocrystalline alloys in Al-based systems*, Progress in Materials Science **43** (1998) pp.365-520.
- [60] A. INOUE *Bulk amorphous alloys - preparation and fundamental characteristics*, Trans Tech Publications Ltd, Switzerland (1998).
- [61] W.S. SANDERS, J.S. WARNER, D.B. MIRACLE *Stability of Al-rich glasses in the AlLaNi system*, Intermetallics **14** (2006) pp.348-351.
- [62] K. SAKSL, P. JÓVÁRI, H. FRANZ, Q.S. ZENG, J.F. LIU, J.Z. JIANG *Atomic structure of Al<sub>89</sub>La<sub>6</sub>Ni<sub>5</sub> metallic glass*, Journal of Physics: Condensed Matter **18** (2006) pp.7579-7592.
- [63] G. WILDE, H. SIEBER, J.H. PEREPEZKO *Glass formation versus nanocrystallization in an Al<sub>92</sub>Sm<sub>8</sub> alloy*, Scripta Materialia **40** (1999) pp.779-783.
- [64] W. G. STRATTON, J. HAMANN, J. H. PEREPEZKO, P M. VOYLESA, X. MAO, S. V. KHAREB *Aluminum nanoscale order in amorphous Al<sub>92</sub>Sm<sub>8</sub> measured by fluctuation electron microscopy*, Applied Physics Letters **86** (2005) pp.141910.
- [65] B. RADIGUET, N. WANDERKA, K.L. SAHOO, D. BLAVETTE, J. BANHART *Segregation controlled nanocrystallization in an Al-Ni-La metallic glass*, submitted to Applied Physic Letters (2008).
- [66] K.F. KELTON, T.K. CROAT, A.K. GANGOPADHYAY, L.-Q. XING, A.L. GREER, M. WEYLAND, X. LI, K. RAJAN *Mechanisms for nanocrystal formation in metallic glasses*, Journal of Non-Crystalline Solids **317** (2003) pp.71-77.
- [67] K. HONO, Y. ZHANG, A.P. TSAI, A. INOUE, T. SAKURAI *Solute partitioning in partially crystallized Al-Ni-Ce(-Cu) metallic glass*, Scripta Metallurgica et Materialia **32** (1995) pp.191-196.
- [68] K.L. SAHOO, M. WOLLGARTEN. K.B KIM, J. BANHART *Crystallization behavior and microhardness evolution in Al<sub>92-x</sub>Ni<sub>8</sub>La<sub>x</sub> amorphous alloys*, Journal of Materials Research **20** (2005) pp.2927-2933.
- [69] K.L. SAHOO, M. WOLLGARTEN, J. HAUG, J. BANHART *Effect of La on the crystallization behaviour of amorphous Al<sub>94-x</sub>Ni<sub>6</sub>La<sub>x</sub> (x = 4-7) alloys*, Acta Materialia **53** (2005) pp.3861-3870.
- [70] A.K. GANGOPADHYAY, K.F.KELTON *Effect of rare-earth atomic radius on the divertification of Al<sub>88</sub>Re<sub>8</sub>Ni<sub>4</sub> amorphous alloys* Philosophical Magazine A **80** (2000) pp.1193-1206.
- [71] N. BAREKAR *Effect of melt-spinning process parameters on the microstructure of Al-Ni-La alloys*, Master thesis, Indian Institute of Technology (2006).

- [72] R.J. HEBERT, J.H. PEREPEZKO *Effect of cold-rolling on the crystallization behavior of amorphous  $Al_{88}Y_7Fe_5$  alloy*, Materials Science and Engineering A **375-377** (2004) pp.728-732.
- [73] Zs. KOVÁCS, P. HENITS, A.P. ZHILYAEV, Á. RÉVÉSZ *Deformation induced primary crystallization in a thermally non-primary crystallizing amorphous  $Al_{85}Ce_8Ni_5Co_2$  alloy*, Scripta Materialia **54** (2006) pp.1733-1737.
- [74] Y. KAWAMURA, H. KATO, A. INOUE, T. MASUMOTO *Full Strength compacts by extrusion of glassy metal powder at the supercooled liquid state*, Applied Physics Letters **67** (1995) pp.2008-2010.
- [75] I. KARAMAN, J. ROBERTSON, J.T. IM, S.N. MATHADHU, Z.P. LUO, K.T. HARTWIG *The effect of temperature and extrusion speed on the consolidation of zirconium-based metallic glass powder using equal-channel angular extrusion*, Metallurgical and Materials Transactions A **34A-35A** (2003) pp.247-256.
- [76] J. SCHROERS, T. NGUYEN, S. O'KEEFFE, A. DESAI *Thermoplastic forming of bulk metallic glass - applications for MEMS and microstructure fabrication*, Materials Science Engineering A **449-451** (2007) pp.898-902.
- [77] J.C. LI, Z.K. ZHAO, Q. JIANG *Bulk high strength  $Al_{85}La_{10}Ni_5$  alloy prepared by hot pressing*, Materials Research Bulletin **37** (2002) pp.297-304.
- [78] J.C. LI, Z.K. ZHAO, Q. JIANG *Properties of high strength  $Al_{85}La_{10}Ni_5$  alloy*, Materials Science Engineering A **A339** (2003) pp.205-208.
- [79] Q. WEI *Elektronenmikroskopische Untersuchungen der Kristallisation im metallischen Massivglas  $Zr_{41}Ti_{14}Ni_{10}Cu_{12.5}Be_{22.5}$* , dissertation thesis, Universität Potsdam (1997).
- [80] D.M. HERLACH, R.F. COCHRANE, I. EGRY, H.J. FECHT, A.L. GREER *Containerless processing in the study of metallic melts and their solidification*, International Materials Reviews **38** (1993) pp.273-347.
- [81] M. BALOG, J. NAGY, F. SIMANČIK, A. CSUBA, G. REQUENA *Direct extrusion vs. ECAP - consolidation of fine Al powders into ultra-fine grained structurally stable profiles*, article in progress (2007).
- [82] P.W. BRIDGEMAN *Effect of high shearing stress combined with high hydrostatic pressure*, Physical Review **48** (1935) pp.825-847.
- [83] M. PHAN *Mahlung und Siebung*, Vorlesungsscript Gemeinschaftslabor Verfahrenstechnik WS2004/05, Ruhr-Universität Bochum (2004).
- [84] W. GRUNER *Determination of oxygen in oxides by carrier gas hot extraction analysis with simultaneous COX detection*, Journal of Analytical Chemistry **365** (1999) pp.597-603.

- [85] K. HEUMANN, S. GALLUS, G. RÄDLINGER, J. VOGL *Precision and accuracy in isotope ratio measurements by plasma source mass spectrometry*, Journal of Analytical Atomic Spectrometry **13** (1998) pp.1001-1008.
- [86] Manual DSC Pyris 1.
- [87] M.J. STARINK *Analysis of aluminum based alloys by calorimetry: quantitative analysis of reactions and reaction kinetics*, International Materials Reviews **49** pp.191-226.
- [88] H.E. KISSINGER *Reaction kinetics in differential thermal analysis*, Analytical Chemistry **29** (1957) pp.1702-1706.
- [89] L.C. CHEN, F. SPAEPEN *Analysis of calorimetric measurements of grain growth*, Journal of Applied Physics **69** (1991) pp.679-688.
- [90] H. ALEXANDER *Physikalische Grundlagen der Elektronenmikroskopie*, G.B. Teubner, Stuttgart (1997).
- [91] C. MICKEL, P. SCHUBERT- BISCHOFF, S. VENKATARAMAN, T. GEMMING, G. SCHEIDER *Preparation of TEM samples of metallic glass powder*, Proceedings of the microscopy conference (an EMS -European Microscopy Society- extension) Davos (2005).
- [92] CH. WEISSMANTEL *Grundlagen der Festkörperphysik*, Springer Press, Berlin (1979).
- [93] I. LANGFORD, D. LOUER *Powder diffraction*, Reports on Progress in Physics **59** (1996) pp.131-234.
- [94] H. KRISCHNER, B. KOPPERLUBER-BITSCHNAU *Röntgenstrukturanalyse und Rietveld Methode*, Vieweg & Sohn Verlagsgesellschaft, Braunschweig/ Wiesbaden (1994).
- [95] CH. GENZEL, I.A. DENKS, M. KLAUS *The materials science beamline EDDI for energy-dispersive analysis of subsurface residual stress gradients*, Materials Science Forum **524-525** (2006) pp.193-198.
- [96] <http://www.hmi.de/bereiche/SF/bessy/eigenspannung.html>
- [97] G. FROMMEYER *Technologien der raschen Erstarrung zur Erzeugung hochwertiger Stähle*, Stahl und Eisen **108** (1988) pp.418-426.
- [98] A. ZAMBON *Nitrogen versus helium: effects of the choice of the atomizing gas on the structures of Fe<sub>50</sub>Ni<sub>30</sub>Si<sub>10</sub>B<sub>10</sub> and Fe<sub>32</sub>Ni<sub>36</sub>Ta<sub>7</sub>Si<sub>8</sub>B<sub>17</sub> powders*, Materials Science and Engineering A **375-377** (2004) pp.630-637.
- [99] H. NITSCHKE *Kinetics of crystallization in amorphous alloys; nucleation and growth*, dissertation thesis, Max-Planck-Institut für Metallforschung Stuttgart, Bericht Nr. 168 (2005).

## REFERENCES

---

- [100] H.Y. HSIEH, B.H. TOBY, T. EGAMI, Y. HE, S. POON, G.J. SHIFLET *Atomic structure of amorphous  $Al_{90}Fe_xCe_{10-x}$* , Journal of Materials Research **5** (1990) pp.2807-2812.
- [101] Z. ZHANG, D. WITKIN, E. LAVERNIA *Crystallization behavior of a gas atomized  $Al_{85}Ni_{10}La_5$  amorphous alloy*, Journal of Non-Crystalline Solids **351** (2005) pp.1646-1652.
- [102] H.W. YANG, J.Q. WANG *Evidence of structural relaxation prior to nanocrystallization in an Al-based metallic glass*, Scripta Materialia **55** (2006) pp.359-362.
- [103] N. BOUCHARAT, H. RÖSNER, G. WILDE *Development of nanocrystals in amorphous Al-alloys*, Materials Science and Engineering C **23** (2003) pp.55-59.
- [104] J.Q. WANG, H.W. ZHANG, X.J. GU, K. LU, F. SOMMER, E.J. MITTEMEIJER *Identification of nanocrystal nucleation and growth in  $Al_{85}Ni_5Y_8Co_2$  metallic glass with quenched-in nuclei*, Applied Physics Letters **80** (2002) pp.3319-3321.
- [105] V. RONTO, L. BATTEZZATI, A.R. YAVARI, M. TONEGARU, N. LUPU, G. HEUNEN *Crystallization behavior of  $Al_{87}Ni_7La_6$  and  $Al_{87}Ni_7Sm_6$  amorphous alloys*, Scripta Materialia **50** (2004) pp.839-843.
- [106] J.C. FOLEY, D.R. ALLEN, J.H. PEREPEZKO *Analysis of nanocrystal development in Al-Y-Fe and Al-Sm glasses*, Scripta Materialia **35** (1996) pp.655-660.
- [107] D.B. MIRACLE *A structural model for metallic glasses*, Nature Materials **3** (2004) pp.697-702.
- [108] S.-W. LEE, M.-Y. HUH, S.-W. CHAE, J.-C. LEE *Mechanism of the deformation-induced nanocrystallization in a Cu-based bulk amorphous alloy under uni-axial compression*, Scripta Materialia **54** pp.1439-1444.
- [109] H.S. CHEN *Structural relaxation in metallic glasses* from F.E. LUBORSKY (ED.) *Amorphous metallic alloys*, Butterworth & Co Ltd London (1983) pp.169-186.
- [110] P.R. OKAMOTO, N.Q. LAM, L.E. REHN *Physics of crystal-to-glass transformations* from H. EHRENREICH, F. SPAEPEN (ED.) *Solid state physics*, Academic Press San Diego (1999) pp.1-135.
- [111] A.S. ARGON *Plastic deformation in metallic glass*, Acta Metallurgica **27** (1979) pp.47-58.
- [112] F. SPAEPEN *A microscopic mechanism for steady state inhomogeneous flow in metallic glass*, Acta Metallurgica **25** (1977) pp.407-415.
- [113] J.J. LEWANDOWSKI, A.L. GREER *Temperature rise at shear bands in metallic glasses*, Nature Materials **5** (2006) pp.15-18.
- [114] W.H. JIANG, M. ATZMON *The effect of compression and tension on shear-band structure and nanocrystallization in amorphous  $Al_{90}Fe_5Gd_5$ : a high-resolution transmission electron microscopy study*, Acta Materialia **51** (2003) pp.4095-4105.

- [115] R.J. HEBERT, J.H. PEREPEZKO, H. RÖSNER, G. WILDE *Dislocation formation during deformation-induced synthesis of nanocrystals in amorphous and partially crystalline amorphous Al<sub>88</sub>Y<sub>7</sub>Fe<sub>5</sub> alloy*, Scripta Materialia **54** (2006) pp.25-29.
- [116] C.A. SCHUH, T.C. HUFNAGEL, U. RAMAMURTY *Mechanical behavior of amorphous alloys*, Acta Materialia **55** (2007) pp.4067-4109.
- [117] G. MAZZONE, A. MONTONE, M. VITTORI ANTISARI *Effect of plastic flow on the kinetics of amorphous phase growth by solid-state reaction in the Ni-Zr system*, Physical Review Letters **65** (1990) pp.2019-2022.
- [118] T. TOMIDA, T. EGAMI *Molecular-dynamics study anisotropy and anelasticity in metallic glasses*, Physical Review B, **48** 5 (1993) pp.3048-3057.
- [119] H.S. CHEN *Glassy metals*, Reports on Progress in Physics **43** (1980) pp.353-432.
- [120] U. SCHWABE, K. MARTIN, E. GUTMACHER, B. GRIMM, W. WÖRSTENFELD *Tafelwerk*, Volk und Wissen, Berlin (1992).
- [121] S. LI, M.A.M. BOURKE, I.J. BEYERLEIN, D.J. ALEXANDER, B. CLAUSEN *Finite element analysis of the plastic deformation zone and working load in equal channel angular extrusion*, Materials Science and Engineering A **382** (2004) pp.217-236.
- [122] K. XIA, X. WU *Back pressure equal channel consolidation of pure Aluminum particles*, Scripta Materialia **53** (2005) pp.1225-1229.
- [123] K. XIA, X. WU, T. HOMMA, S.P. RINGER *Ultrafine pure aluminum through back pressure equal channel angular consolidation of particles*, Journal of Materials Science **42** (2007) pp.1551-1560.
- [124] O.N. SENKOV, S.V. SENKOVA, J.M. SCOTT, D.B. MIRACLE *Compaction of amorphous aluminum alloy powder by direct extrusion and equal channel angular extrusion*, Materials Science and Engineering A **393** (2005) pp. 12-21.